2013

Mechanical Properties And Thermal Residual Stresses Of Zrb2-sic Ceramic Composites For Hypersonic Vehicle Applications

Richard Stadelmann
University of Central Florida

MECHANICAL PROPERTIES AND THERMAL RESIDUAL STRESSES OF ZrB$_2$-SiC CERAMIC COMPOSITES FOR HYPERSONIC VEHICLE APPLICATIONS

by

RICHARD PHILIP STADELMANN
B.S. University of Central Florida, 2011

A thesis submitted in partial fulfillment of the requirements
for the degree of Master of Science
in the Department of Mechanical & Aerospace Engineering
in the College of Engineering & Computer Science
at the University of Central Florida
Orlando, Florida

Fall Term
2013

ABSTRACT

Ultra High Temperature Ceramic (UHTC) ZrB_2- 10, 20, 30wt%SiC composites are of high interest for use in hypersonic air-breathing vehicles. In this work, ZrB_2- 10, 20, 30wt%SiC UHTC composites were produced by the Spark Plasma Sintering (SPS) technique. After sintering, almost dense ceramics with ~ 5-8% porosity were produced. Their mechanical properties, such as Young's, shear, and bulk moduli, along with Poisson's ratio, 4-point bending strength, and single edge V-notched beam (SEVNB) fracture toughness were measured. In addition, *in-situ* bending experiments under a Raman microscope were performed to determine the piezo-spectroscopic coefficients of SiC Raman active peaks for calculation of thermal residual stresses. The results show that these materials are possible candidates for hypersonic air-breathing vehicles due to their high Young's modulus, ability to withstand high temperatures, and relatively low densities.

This thesis is dedicated to my wife, Paulette Stadelmann, for giving all her love and support throughout the preparation of my thesis and my graduate academic career. Also to my parents and sister for all of their love and support throughout my entire life.

ACKNOWLEDGMENTS

This thesis is a result of the guidance, patience, and support I have received from my advisor, Dr. Nina Orlovskaya. Dr. Nina first introduced me to the use of materials for aerospace application, which allowed me to incorporate my passion and interest for aerospace engineering. I express my deepest gratitude to Dr. Nina for all the time and efforts she has put into to guiding me through my research and encouraging me to go the extra mile.

I am very grateful for Cassandra Carpenter, who laid down the foundation of the research conducted in this thesis. Likewise, I am grateful for Dr. Sglavo, Dr. Radovic, and Dr. Reece for their contributions to this work.

I would like to thank Dr. Ranganathan Kumar and Dr. Seetha Raghavan for being on my thesis committee.

Finally, I would like to thank all of my friends and family for the added support in my life to accomplish anything I want.

TABLE OF CONTENTS

LIST OF FIGURES

xi

LIST OF TABLES

CHAPTER 1: INTRODUCTION

From the beginning of time, mankind has sought ways to fly. In 1902, the Wright brothers made the dream of powered flight possible, allowing man to fly for extended periods of time. As the years grew on, advances in airplanes came about with the improvements of the understanding of aerodynamics. The development of planes had a great impact in war, especially during World War I, where the first dog fights occurred. From this war, both sides saw how important of a contribution an airplane would be to war; this caused the airplane to grow in design and development. With World War II (WWII), airplanes had a major role in combat. Not only did WWII give rise to an advent of new airplanes, it also led to the development of the new turbojet engine used in many military aircrafts to this day. After the wars were over, airplanes started to be used as a means of travel around the world. Airplanes had much shorter travel times compared to traveling by ship. When the Cold War set in, there were many secret government projects intended to develop the fastest and most technologically advanced airplanes in the world. Chuck Yeager broke the sound barrier using the Bell X-1 rocket, thus bringing man into the age of flying faster than the speed of sound. Chuck later broke this record by flying at a speed of Mach 2.44, or 2.44 times faster than the speed of sound. The "Space Race" during the Cold War brought about even more technological advances that gave way to a new era of rockets and airplanes.

With this research and development to make airplanes more efficient and fly faster than ever, we are constantly searching for the technology of the future, especially in hypersonic missiles, and re-entry aerial vehicles. This is creating high demand for more research and better materials. We have already been able to achieve sustained supersonic flight and short flights at

hypersonic speed, speeds that are greater than 5 times the speed of sound or Mach >5. At sea level, the speed of sound is around 342 m/s. So Mach >5 at sea level would be speeds higher than 1710 m/s. However, we have not been able to sustain flight at a hypersonic range for long periods of time, such as a couple of hours. This is mainly due to the fact that materials used today are not able to withstand the extreme environment of hypersonic flight for extended periods of time. In this hypersonic flight regime, temperatures can exceed $2600°C$. At these temperatures, most materials melt or greatly lose their mechanical properties, which could cause catastrophic failure of the component and ultimately the aerial vehicle. High temperatures are not the only obstacles in hypersonic flight; there are also extreme aerodynamic loads, including separated strong shock waves, making it difficult to sustain the flight at speeds greater than 1710 m/s. With the combination of the high temperature and high aerodynamic loading, very few materials would be able to withstand these conditions. In addition, hypersonic flight is an aggressive oxidizing environment, which further increases the difficulty of finding proper materials to withstand this extreme environment. The reason for the high oxidation is due to Oxygen and Nitrogen disassociation (the splitting of a diatomic molecule to single atoms that then can readily react) [1-6].

The main components that this extreme environment affects are the leading edges and nose cones. These components have to be able withstand the highest temperature that can potentially exceed 2600 °C, at the stagnation point. Not only do they need to withstand the high temperatures, but they also need to be able to withstand very high temperature gradients. These temperature gradients can be as high as 1000 °C in a very short distance of 2mm [7, 8]. An example of the heat transfer on a leading edge is shown below in Figure 1.

2
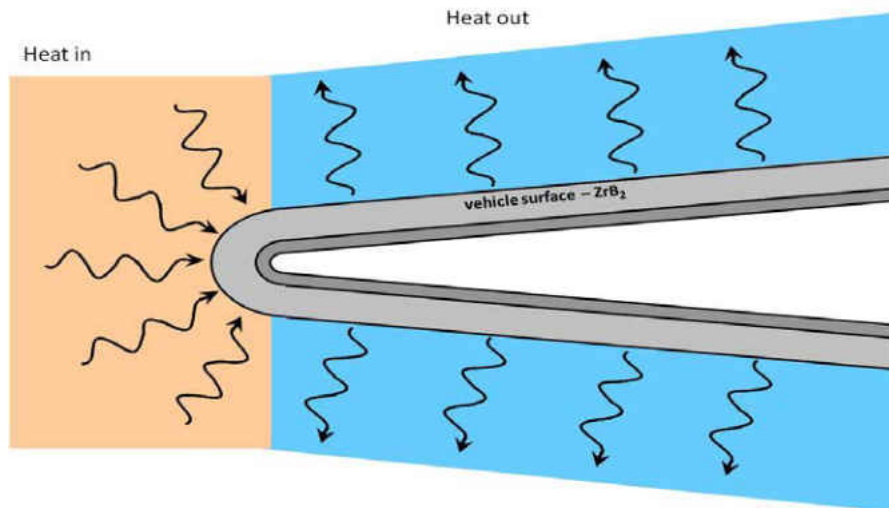
Figure 1: A schematic presentation of leading edge configuration [3]

On top of this, the material of these components must hold its shape, even with the high aerodynamic loading along with the high thermal loading. This environment also requires a material that is oxidation resistant, and withstands ablation (which is the removal of material by vaporization).

With the environment characterized, one can come up with the requirements that the material must meet in order to be used for this application. Therefore, the material must have high strength to withstand the high aerodynamic forces, have a high thermal conductivity in order to be able to handle the high heat fluxes, and since the application is an aerial vehicle, the material must be light and thus have a low density. Therefore, one comes across the refractory metals, such as ZrB_2. These materials are promising but, due to the flow, encouraging oxidation ZrB_2 by itself would decompose, and then the material would be weakened and thus catastrophic

3

failure will would occur. Therefore, SiC-phase has been added to ZrB$_2$ in order to increase the oxidation resistance, resulting in a ceramic composite [6, 9-11]. This increases the oxidation resistance, and is accomplished when SiC oxidizes to form a SiO layer, which is a stable glassy oxide that prevents oxygen from penetrating further into the material. Basically, the SiO layer is effectively a barrier between the flow environment and the component on the vehicle. Figure 2 below shows the result of oxidation at 1900 °C at three different compositions of SiC in ZrB$_2$.

Figure 2: Oxidation models at 1900 °C of ZrB2 with low SiC content(a), medium SiC content(b) and high SiC content(c), with the white color representing holes [12].

From the conditions of the environment, we can determine the properties of materials that must be met. The materials must have a high melting temperature, oxidation resistance, high thermal conductivity, high toughness, and high Young's modulus. This brings us to a group of materials that are called Ultra High Temperature Ceramic (UHTC) composites; these ceramic composites have high thermal conductivity and high melting temperatures, making them perfect candidates for hypersonic vehicles. Figure 3 below shows all of the components and effects of atmospheric re-entry from space.
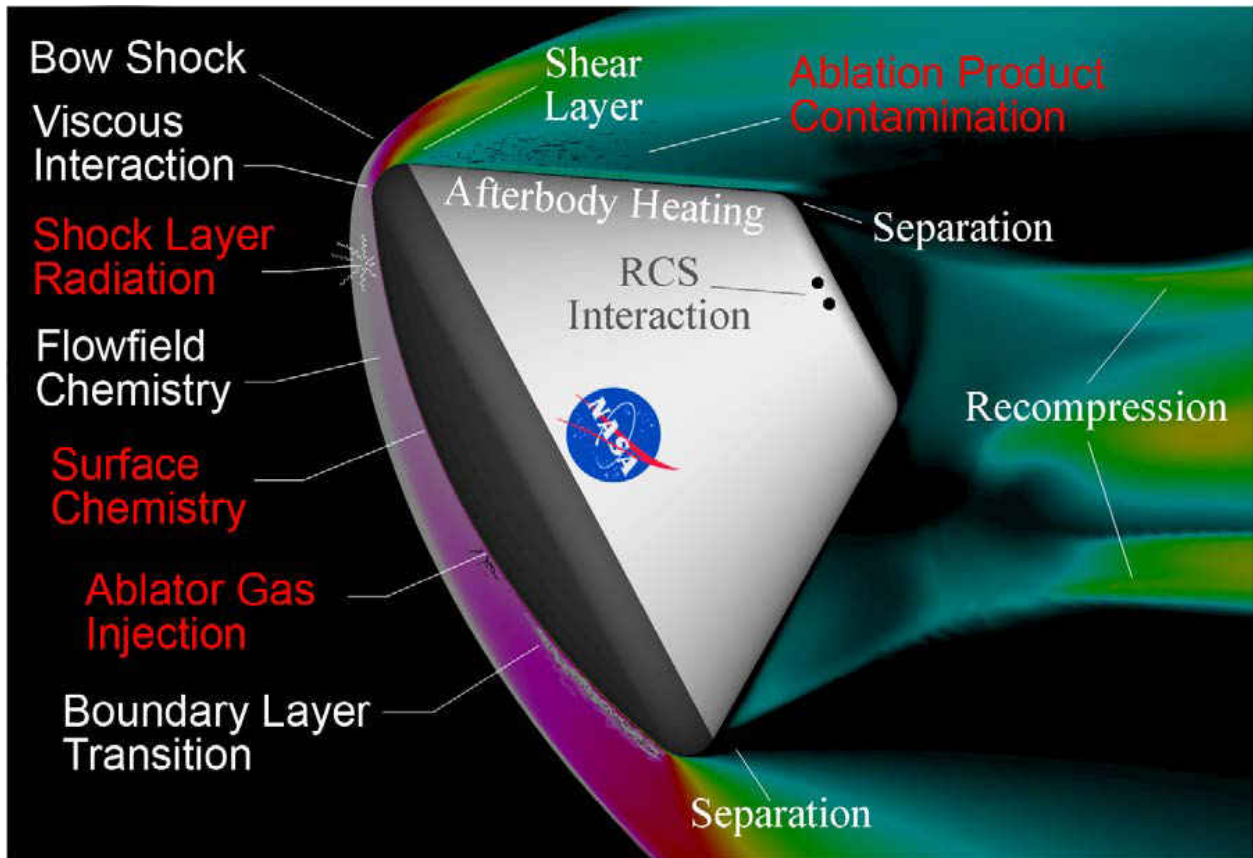
Figure 3: Re-entry to Earth's atmosphere [13]

Following this introduction section is the literature review section, which will cover everything known about ZrB_2-SiC ceramic composites found in literature. This includes everything from the crystal structure and phase diagrams to fatigue and arc jet tests. Following that section is the experimental procedure section, which will go over in detail how each experiment was conducted. Following the experimental procedure are the results, conclusion, and future plans for this research, which will be described in this thesis.

CHAPTER 2: LITERATURE REVIEW

When conducting research, it is imperative to know what others have done before so one can determine if the results are valid or not. That is why this section is included in this thesis. The first thing that one would be interested in learning about a material is the crystal structure or the smallest repeatable unit cell and the phase diagram of a material. This is important because the fact that the crystal structure determines the density of a material along with the mechanical properties. The phase diagram indicates which phase is present at what temperature and pressure. This is very helpful since this will help one know when a solid material will become a liquid.

2.1: ZrB_2 Crystal Structure

First, the crystal structure of ZrB_2 by itself will be discussed. The typical structure of ZrB_2 has only one possible crystal structure for this phase, which is the hexagonal structure. This crystal structure is shown below in Figure 4. Looking at the ZrB_2 crystal structure as shown below as Figure 4a, one can see the location of the boron and Zr atoms. The boron atoms are in a face-centered structure position, while the Zr atoms are located at the center of the unit cell and at the midpoint between each of the boron atoms. Figure 4B shows the ZrB crystal structure just for comparison to the crystal structure of ZrB_2. On the next page, Figure 5 shows a better 3-D representation of the crystal structure. This representation of the ZrB_2 crystal structure shows a layer of boron atoms and then a layer of Zr atoms, and then the layers repeat. The lattice parameters for ZrB_2 are a $\approx 3.17\mathring{A}$, and c $\approx 3.5\mathring{A}$ [14].
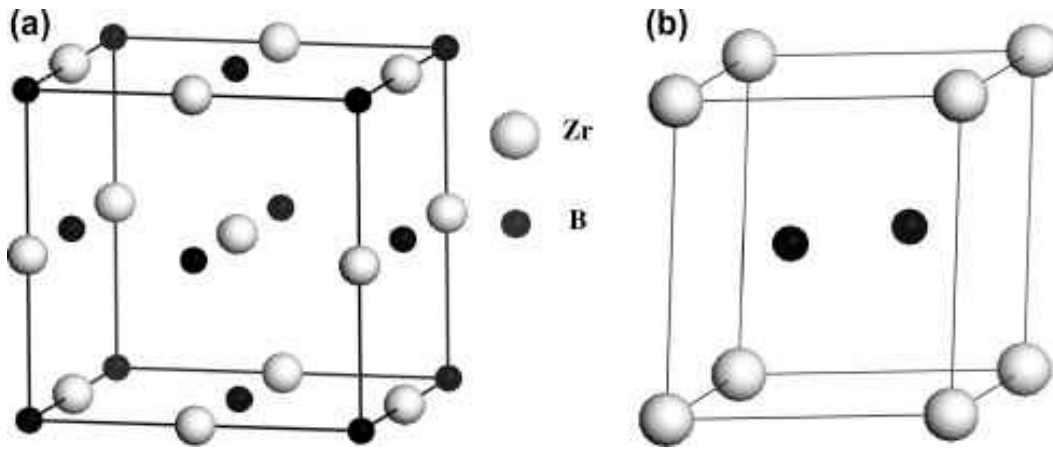
Figure 4:ZrB2 crystal structure (a) and ZrB crystal structure (b) [14]
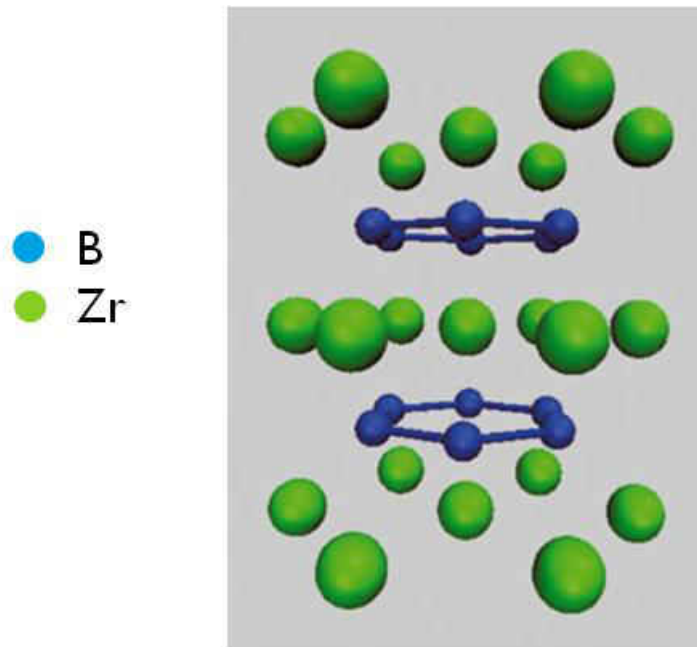
Figure 5: 3D Visualization of ZrB2 crystal structure [15]

<u>2.2: SiC Crystal Structure</u>

The crystal structure of SiC is hard since SiC has many different polytypes. The polytypes refer to the order of the repeated structure. For example, 3-cubic would be a cubic unit cell with 3 different unit cells being repeated. There are over 200 polytypes for SiC thus making it hard to pinpoint the crystal structure throughout the entire component. The most common of these polytypes are as follows: 3-cubic, 2-hexagonal, 4-hexagonal, 15-rhombohedral, 6-hexagonal, and 8-hexagonal [16]. Within the scopes of this paper and my current research, I will be using 6-hexagonal as my SiC crystal structure. Figure 6 below shows the crystal structure of 6-hexagonal SiC. Figure 6 also shows 3-cubic and 4-hexagonal SiC crystal structures. Figure 7 shows a 3-D depiction of the ideal SiC crystal structure.
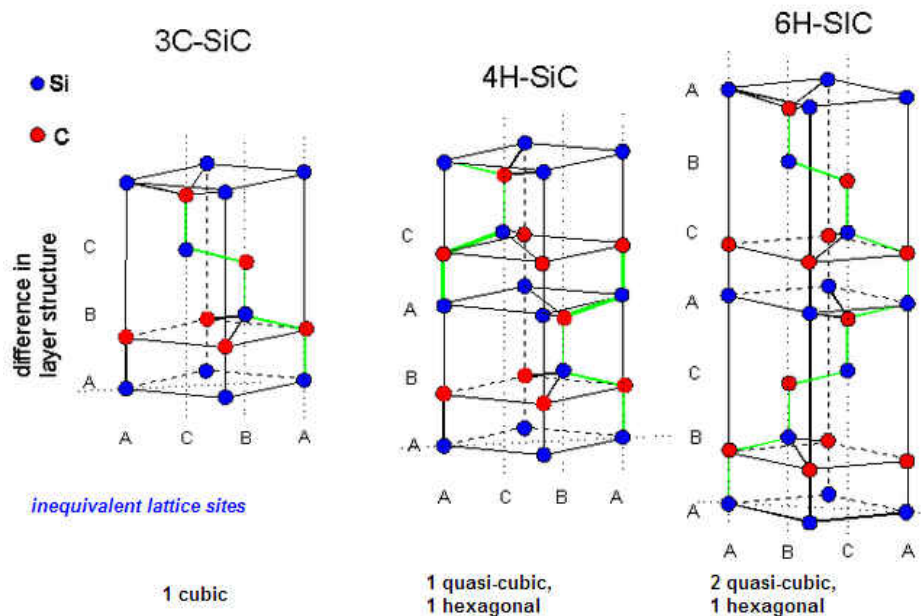
Figure 6: 6-hexagonal SiC crystal structure [17]
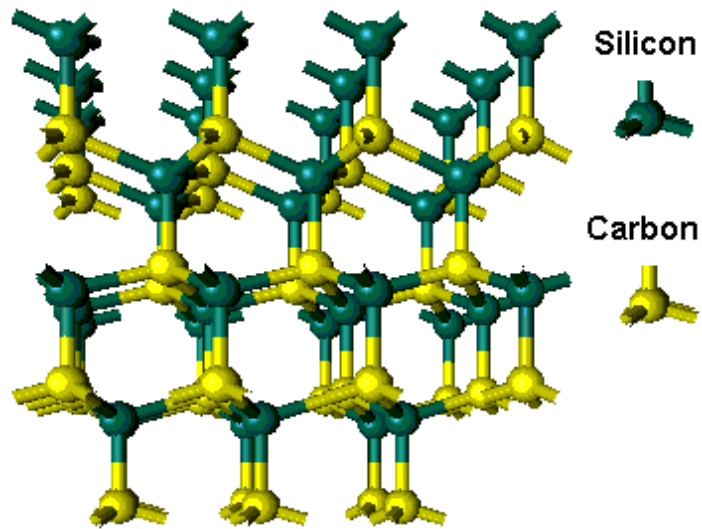
Figure 7: 6-hexagonal SiC crystal structure [18]

The lattice parameters for SiC are shown below in Table 1. Table 1 shows multiple polytypes of SiC lattice parameters. Based on Figure 6, one would expect that 3-cubic would have the smallest lattice parameter in the z-direction or vertical direction and that 6-hexagonal will have a larger lattice parameter in that direction. Looking at Table 1, one finds this to be the case.

Table 1: SiC lattice parameters with the Ceperly-Alder correlation are given in parentheses [19]

	Calculation Method	a($\overset{\circ}{\mathrm{A}}$)	c/a
Si	Theoretical	5.432[a]	
		5.433[b],5.435[c]	
	Experimental	5.429[d]	
C	Theoretical	3.56[a]	
		3.561[b], 3.607[c]	
	Experimental	3.567[d]	
3C-SiC	Theoretical	4.358 (4.354)[a]	
		4.361[b,e], 4.326[f], 4.365[g]	
	Experimental	4.36[d]	
2H-SiC	Theoretical	3.072[a]	1.641[a]
		3.12[h]	1.611[h]
	Experimental	3.076[c]	1.641[c]
4H-SiC	Theoretical	3.069[a]	3.292[a]
	Experimental	3.073[c]	3.271[c]
6H-SiC	Theoretical	3.077[a]	4.91[a]
	Experimental	3.073[c]	4.907[c]

[a][19], [b][20], [c][21], [d][22],[e][23, 24],[f][25] ,[g][26],[h][27]

2.3: ZrB_2 Phase Diagram

The phase diagrams found for these compositions were actually for the Zr-B system, since at different temperatures and compositions one will either end up with ZrB or ZrB_2. Figure 8a below shows the Zr-B phase diagram without labels for the different phases. This figure was created by Kufman[28], but an updated version that is easier to see where the specific phases and what the compositions are is shown below as Figure 8b. This phase diagram, Figure 8b, shows the same information as Figure 8a, but includes labels of where the different phases of the Zr-B system are with respect to the composition of the molecules. Multiple phase diagrams exist for the same system. Looking at Figure 8 again, one can see that it is very easy to get ZrB or ZrB_{12}

instead of ZrB_2. This is very important when producing ZrB_2 powders for commercial use or when using the powder to produce samples for testing.

The three key factors that complicated the determination of accurate phase equilibrium diagrams for ZrB_2 are it has very high melting temperatures, slow solid-state reaction rates and boron vaporization [2]. Another factor that contributes to the complexities of the phase diagram is that boron may have more than one phase present; this is most commonly found with powders produced with the powder-metallurgy techniques [2]. Figure 9 shows a Zr-B system phase diagram produced by experimental and theoretical methods and show the approximate temperatures and wt % for boron for which important phases are located. ZrB_2 phase is the dominate phase of the Zr-B system.
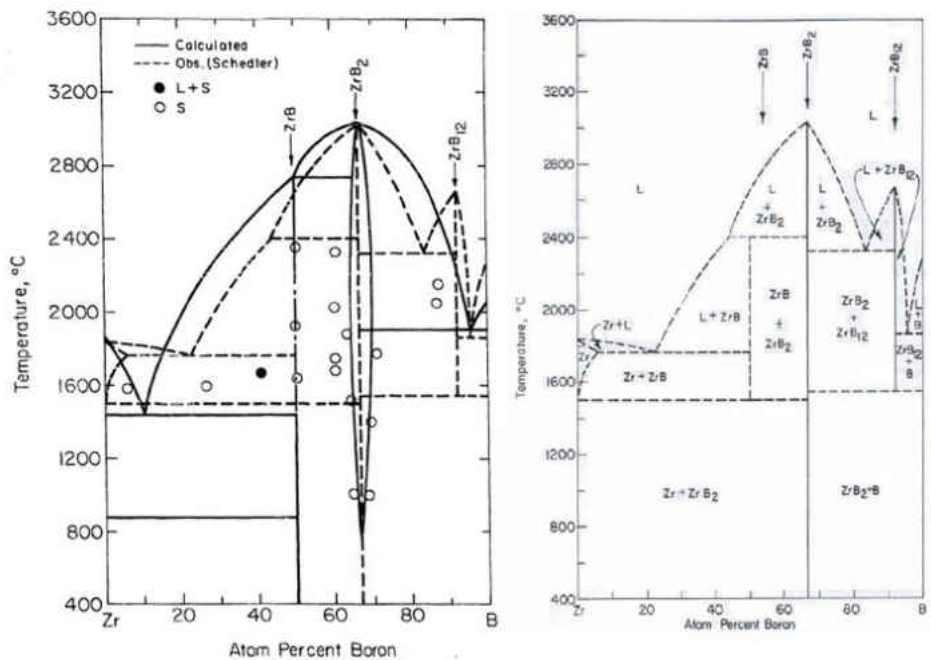
Figure 8: Phase diagram Zr-B system without labels(a), and with labels of the phases(b) [2, 28]

12
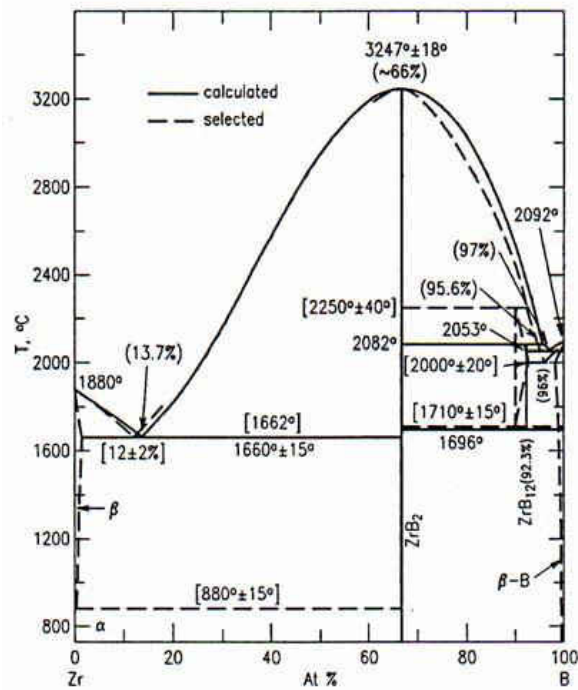
Figure 9: Phase diagram Zr-B system based on the experiments results [29]

2.4: SiC Phase Diagram

Now for the phase diagram of the Si-C system, one finds not as many phase diagrams as found for the Zr-B system phase diagrams. Two phase diagrams were found for the Si-C system, which are shown on the next page as Figure 10 & Figure 11. Figure 10 shows the Si-C system phase diagram with some labels and approximated temperature at which the phase will change. Looking at this first phase diagram in Figure 10, one finds that the melting point of the SiC increases with an increase in pressure that the material is exposed to. One also sees a dotted region; I do not know what this region is and why it is there. The region is also not labeled with a phase, so one has no idea what it is just from looking at it. Now looking at Figure 11, one finds that this phase diagram only goes to 3500 °C while the other phase diagram, Figure 11, goes up

13

to 4500 °C. Also, the graph of Figure 11 starts at 1500 °C while Figure 10 starts at 1000 °C. Comparing the two figures further, one sees the temperature at which the phase occurs is slightly different between the two figures. This goes to show that even though the two phase diagrams are of the same material, they can be reported very differently. One believes that the main cause of the difference in reporting the temperature at which the phase changes is the method at which the phase diagram was produced, and the method at which the powder was produced may be different and from a different company. Another cause could be that, since SiC has so many different polytypes, one was produced for one polytype and the other by another polytype. Upon looking at the phase diagrams further, one sees that there are only a few phases: Si(l), SiC+C, Si+SiC, and Si(l)+SiC. Comparing this to Zr-B system, one again sees that this phase diagram is a lot less complex, and it is much easier to produce these phase diagrams experimentally.
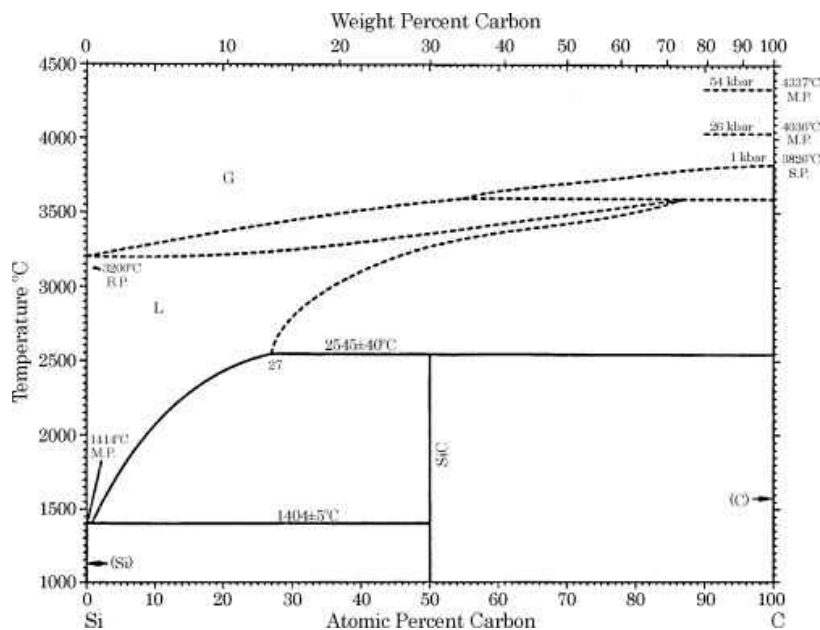
Figure 10: Si-C system Phase Diagram [30]

14
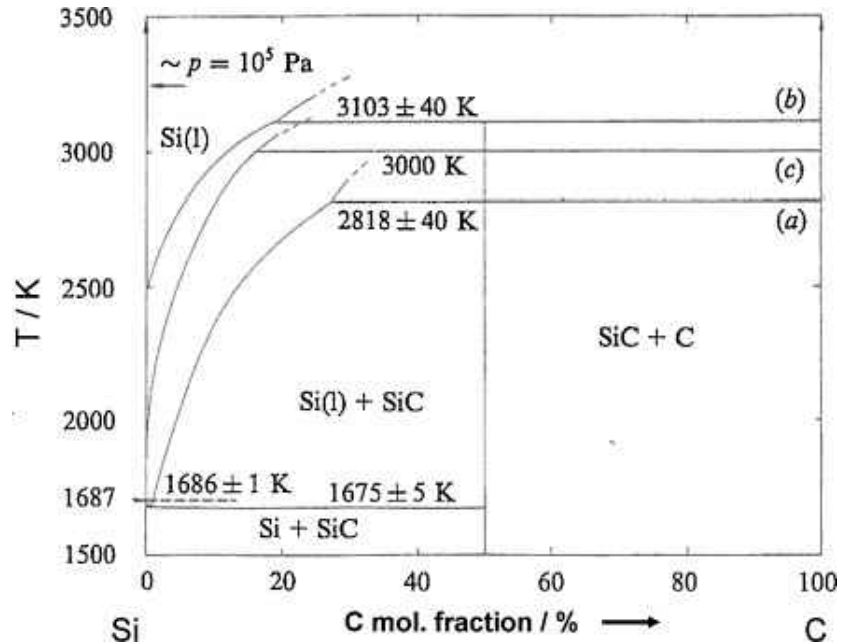
Figure 11: Si-C binary system Phase Diagram [31]

2.5: ZrB$_2$-SiC Phase Diagram

One was able to find one ZrB$_2$-SiC phase diagram. This phase diagram is shown below as Figure 12. Looking at this Figure 12, one finds that in the ZrB$_2$-SiC phase diagram, there is one eutectic point that occurs at approximately 2270 °C at a composition of 23 mol% ZrB$_2$ of the ZrB$_2$-SiC system. One also sees that there is only one phase labeled, and that is the liquid phase, the rest of the phases have been left unlabeled. This is probably due to the fact that the research was only interested in the point at which the ZrB$_2$-SiC system becomes a liquid at different compositions of ZrB$_2$.

15
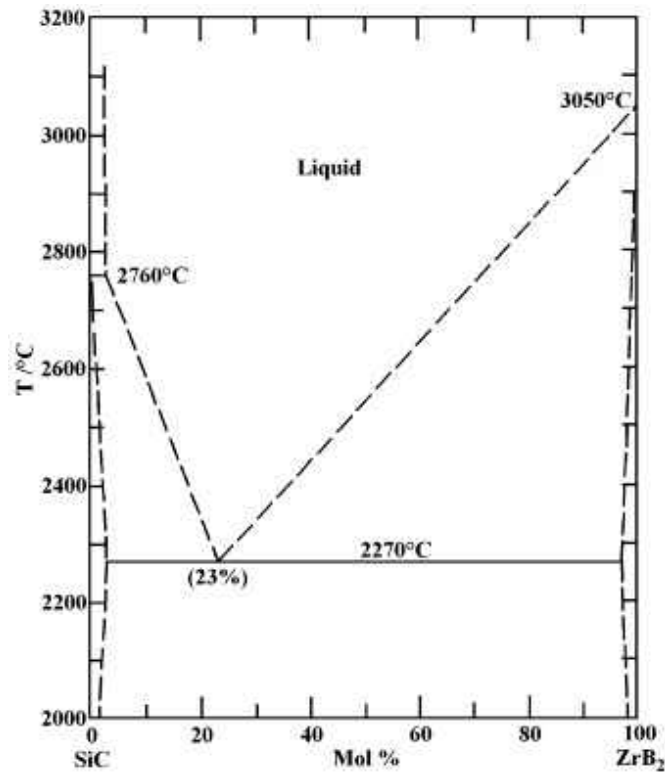
Figure 12: ZrB2-SiC Phase Diagram [32]

<u>2.6: ZrB$_2$-SiC Processing Methods</u>

Now looking in through literature to find out the mechanical properties and sintering processes used for ZrB$_2$-SiC ceramic composites. The two most common methods of sintering these ceramic composites are hot pressing (HP) and spark plasma sintering (SPS). A few other methods have been used, such as Electron Beam Sintering [33] and reactive-SPS sintering [34]. The bulk of all publications have been in hot pressing, but, in the past year, a lot of research has been conducted using the relatively new process of SPS for UHTC composites. Hot pressing uses heating elements to heat a sample to be sintered to the temperature wanted, followed by

applying pressure on the sample while in a vacuum. Figure 13 below shows a diagram of a hot pressing machine.
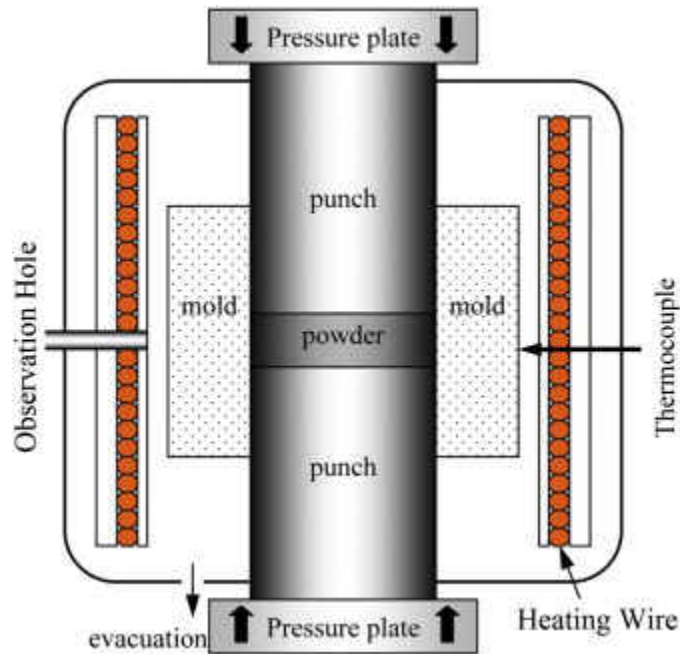
Figure 13: Schematic drawing of hot press sintering [35]

SPS uses pulsing electrical current to heat up the powder being sintered to the temperature the sample sinters at. In addition, the sample is placed under pressure, along with the sample is in a vacuum all at the same time. Figure 14 below shows a diagram of a SPS machine. The pulsing electrical current allows for high heating cooling rates, which shorten the time to produce a sample to about 1-2 hours instead of 6 hours in a hot pressing machine.
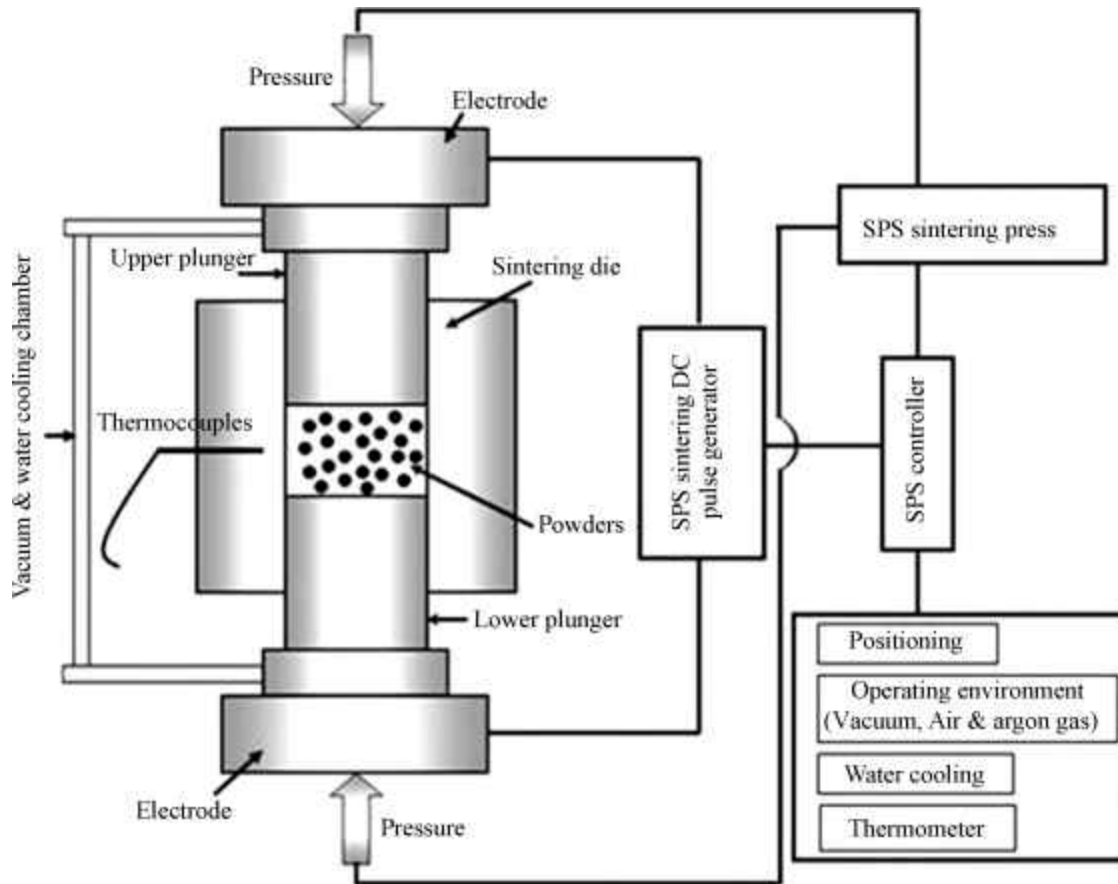
Figure 14: Schematic pattern of spark plasma sintering [36]

With this relatively new sintering process, a few papers were on the effects of heating rate and composition of ZrB_2-SiC on its mechanical properties [37, 38]. Many of these recent publications are on finding the parameters in SPS that give a full density material, with the desired mechanical properties, the shortest amount of time to sinter and the lowest temperature to decrease cost of the sample. One such experiment, conducted by Akin, found that sintering ZrB_2-SiC with 20-60mass% SiC were 99% dense at temperature between 2000-2100°C with a hold time of 180 seconds. Akin also found that the microstructures in samples above 2120°C were different then samples with microstructures below that temperature [39]. The difference in

18

microstructure is shown below as Figure 15. Looking at Figure 15, one sees that at 1900ºC and 2100ºC samples, the SiC grains are small and distributed throughout the entire sample, while the high temperature samples without hold times have large SiC grains and are not well distributed. The sample looks to be almost entirely SiC rather than a composite of ZrB_2-SiC. Now looking at Figure 16, one finds that same pattern as in Figure 15 with the increase of sintering temperature. Figure 17 below shows the microstructure of ZrB_2-SiC with a different weight percent of SiC. Figure 17 also shows the effect of adding carbon to the ZrB_2-SiC on the microstructure of the composite.
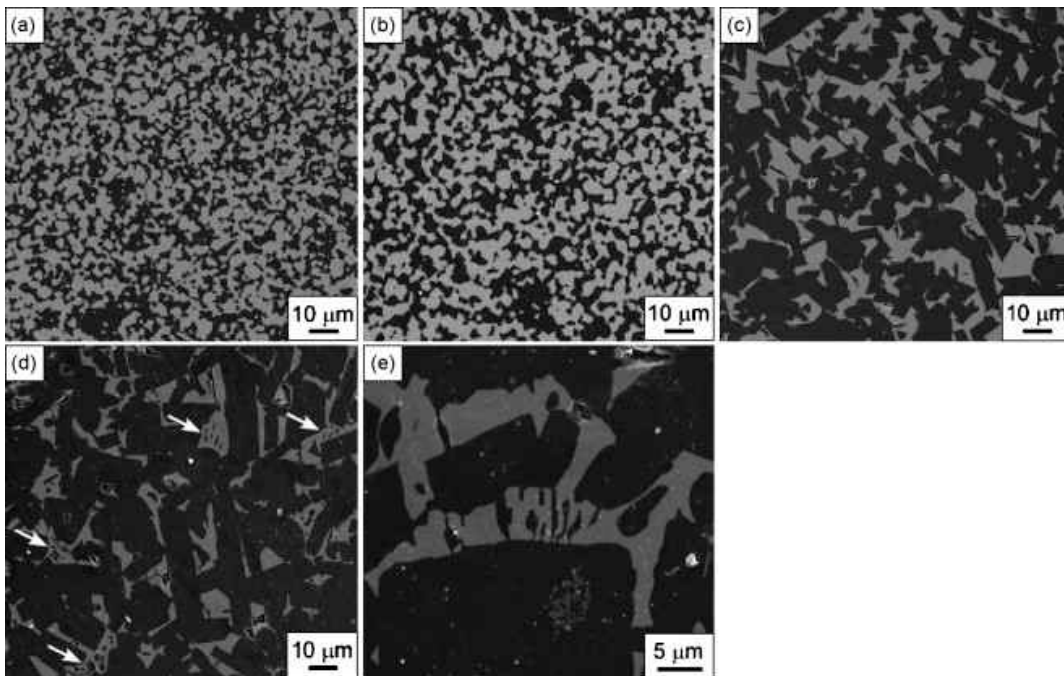
Figure 15: SEM images of polished surfaces of ZrB_2–SiC composites containing 40 mass% SiC sintered at 1900 °C for 300 s (a), 2100 °C for 180 s (b), 2120 °C (c), 2200 °C (d) without a holding time and high magnification of irregular texture at 2200 °C (e) [39].
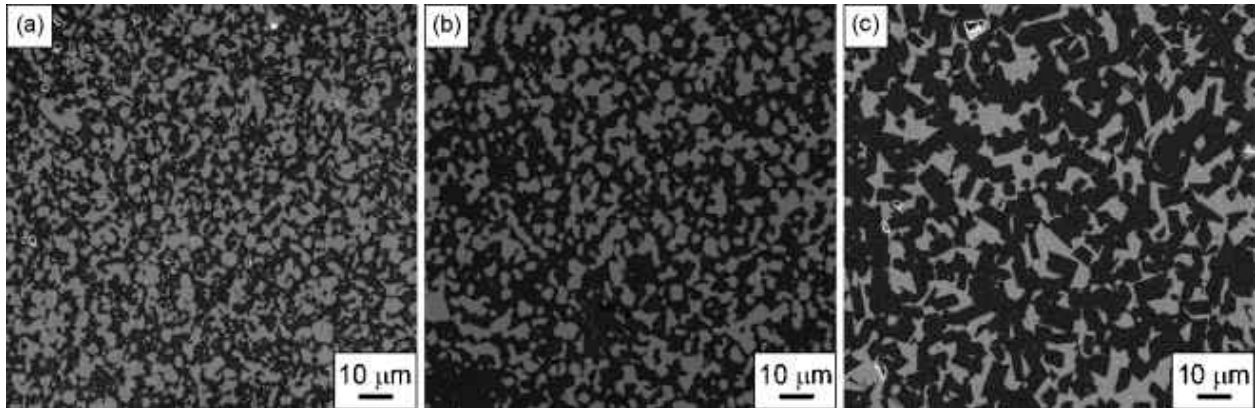
Figure 16: SEM images of polished surfaces of ZrB$_2$–SiC composites containing 50 mass% SiC sintered at 1900 °C for 300 s (a), 2100 °C for 180 s (b) and 2165 °C without a holding time (c) [39].
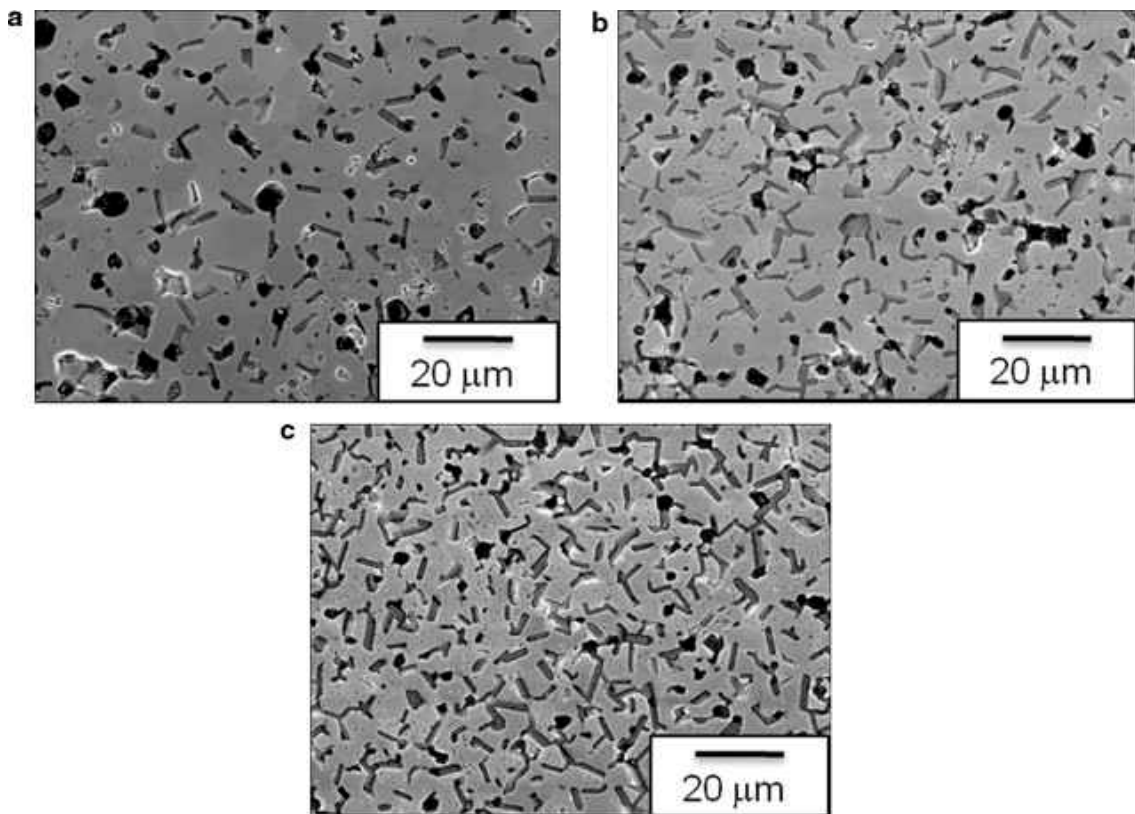
Figure 17: Microstructure of ZrB$_2$ ceramics containing (A) 10 vol%, (B) 20 vol%, and (C) 30 vol% SiC (UF-25) additions and 5 wt% carbon [40].

2.7: ZrB$_2$-SiC Mechanical Properties

Looking through many publications, one can find a range of the mechanical properties. Pure ZrB$_2$ has the following mechanical properties that were found in literature and are shown in the Table 2 below.

Table 2: ZrB$_2$ Mechanical Properties

Young's Modulus [41, 42]	489-493 GPa
Melting Temperature[43]	3100-3500 °C
Density[44]	6.09 g/cm^3
Vickers Hardness [41]	21-23 GPa
Fracture Toughness [45, 46]	5.46-6.02 MPam$^{1/2}$
Fracture Strength [45, 46]	416-708 MPa
Coefficient of Thermal Expansion[47, 48]	5.9x10^{-6} K^{-1}
Thermal Conductivity [41]	60 W/mK

Also looking at the mechanical properties of pure 6H-SiC, one finds the following mechanical properties as shown in the Table 3 below. The reason for the 6H-SiC polytype is that it is the material use to conduct the experiments for this thesis.

Table 3: SiC Mechanical Properties

Young's Modulus [49, 50]	440±20 GPa
Melting Temperature[51]	2700 °C
Density[52]	3.21 g/cm^3
Vickers Hardness [49]	32 GPa
Fracture Toughness [49]	6.8 MPam$^{1/2}$
Fracture Strength [49]	490±70 MPa
Coefficient of Thermal Expansion[53]	4.16x10^{-6} K^{-1}
Thermal Conductivity [52]	0.9-50 W/mk

Looking at this, one can infer that the ZrB_2-SiC ceramic composites will have a Young's modulus lower than pure ZrB_2, but higher than pure SiC, based on the theory of mixers. When looking through existing literature, this is found to be the case. Table 4 and Table 5 below show the mechanical properties of ZrB_2-SiC ceramic composites. Looking at these two tables, one notices that with the decrease of SiC maximum grain size, the strength, Knoop hardness and Young's modulus increase. The Vickers hardness increases until a particle size of 6.4μm, and then starts to decrease again. Table 5 does not change the SiC particle size, but it does change the amount of SiC present in the ZrB_2-SiC. From Table 5, one finds that as the SiC volume percent in the ZrB_2SiC ceramic composites is increased, the Young's Modulus, Hardness, Flexure Strength, and Toughness all increase.

Table 4: Summary of Mechanical Properties for Varying SiC Particle Size ZrB_2–SiC Composites [54]

Composition	Final maximum SiC particle size (μm)	Strength (MPa)	Elastic modulus (GPa)	Vickers hardness (GPa)	Knoop hardness (GPa)
HC Starck SiC grade UF-25	4.4	1150 ± 115	541 ± 22	21.4 ± 0.6	17.2 ± 0.2
HC Starck SiC grade UF-10	6.4	924 ± 100	532 ± 13	21.7 ± 0.6	17.1 ± 0.3
HC Starck SiC grade UF-5	8.2	892 ± 120	534 ± 20	21.2 ± 0.4	17.0 ± 0.2
ZrB_2-30vol%SiC Milled 8 hours	11.5	825 ± 118	531 ± 14	21.2 ± 0.6	17.1 ± 0.3
ZrB_2-30vol%SiC Milled 4 hours	11.8	724 ± 83	520 ± 12	19.3 ± 1.8	16.1 ± 0.3
ZrB_2-30vol%SiC Milled 2 hours	12	460 ± 47	518 ± 16	18.6 ± 0.5	15.6 ± 0.4
ZrB_2-30vol%SiC Milled 1 hour	13	280 ± 34	505 ± 7	18.4 ± 1.3	15.6 ± 0.4

Composition	Final maximum SiC particle size (μm)	Strength (MPa)	Elastic modulus (GPa)	Vickers hardness (GPa)	Knoop hardness (GPa)
HC Starck SiC grade UF-25	4.4	1150 ± 115	541 ± 22	21.4 ± 0.6	17.2 ± 0.2
HC Starck SiC grade UF-10	6.4	924 ± 100	532 ± 13	21.7 ± 0.6	17.1 ± 0.3
HC Starck SiC grade UF-5	8.2	892 ± 120	534 ± 20	21.2 ± 0.4	17.0 ± 0.2
ZrB_2-30vol%SiC Milled 8 hours	11.5	825 ± 118	531 ± 14	21.2 ± 0.6	17.1 ± 0.3
ZrB_2-30vol%SiC Milled 4 hours	11.8	724 ± 83	520 ± 12	19.3 ± 1.8	16.1 ± 0.3
ZrB_2-30vol%SiC Milled 2 hours	12	460 ± 47	518 ± 16	18.6 ± 0.5	15.6 ± 0.4
ZrB_2-30vol%SiC Milled 1 hour	13	280 ± 34	505 ± 7	18.4 ± 1.3	15.6 ± 0.4
ZrB_2-30vol%SiC Milled 0 hour	18	245 ± 23	484 ± 6	17.3 ± 1.4	15.2 ± 0.3

Table 5: Comparison of mechanical properties of ZrB_2 with 10, 20, and 30 vol% SiC [40]

SiC volume fraction (vol%)	10	20	30
Carbon addition (wt%)	5% Based on the SiC weight		
B4C addition (wt%)	4% Based on ZrB2 weight		
Sintering conditions	2000 °C/3 h	2000 °C/3 h	2000 °C/3 h
Sintered density (%)	~97	>97	>99
Elastic modulus (GPa)	446 ± 7	474 ± 7	490 ± 7
Hardness (GPa)	15.3 ± 1.2	18.8± 1.1	22.4 ± 0.7
Flexure strength (MPa)	404 ± 62	463 ± 53	492 ± 49
Toughness (MPa m^1/2)	3.1 ± 0.1	3.4 ± 0.1	3.5 ± 0.3

Continuing the search for the mechanical properties, one finds many more papers about ZrB_2-SiC ceramic composites; such papers cover more about the effects of the SiC grain size on the mechanical properties of the ceramic composites. But one can find papers about elevated

temperature mechanical properties as well as ablation and oxidation resistance tests. Starting with the other mechanical properties found, first of which is strength testing, or flexure test, one sees again that, with increase of SiC volume/mass percent in the composites, there is a decrease in the SiC grain size. There is also an increase in the fracture strength of the ceramic composites. Figure 18, Figure 19, Figure 20 and Figure 21 shown below show this trend and all agree with each other. These results were from multiple sources. Thus one can conclude that this trend should be the same for the results of this thesis.
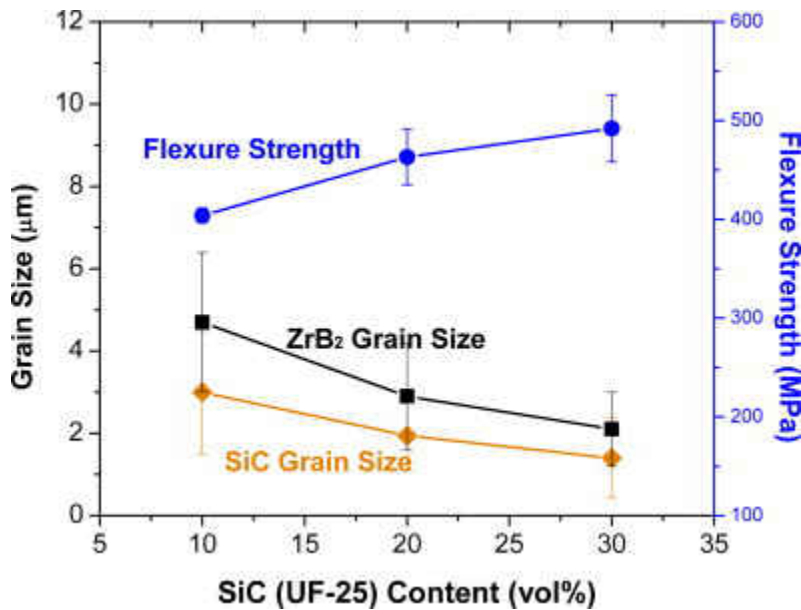
Figure 18: Room temperature flexure strength, as well as ZrB$_2$ and SiC grain sizes, for ZrB$_2$–SiC materials as a function of SiC (UF-25) volume fraction [40].
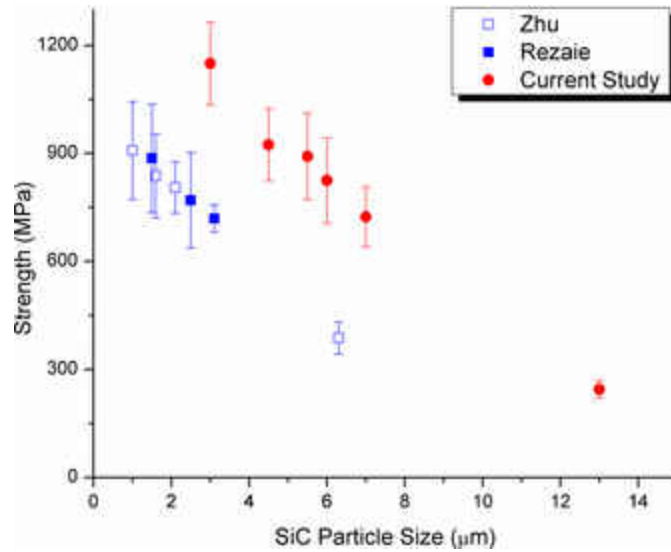
Figure 19: Strength of ZrB₂–SiC composites as a function of the average SiC particle size measured as an average circular diameter from Zhu [55], Rezaie [11, 56] and the current study as a function of the maximum SiC particle size also measured as a circular diameter [54].
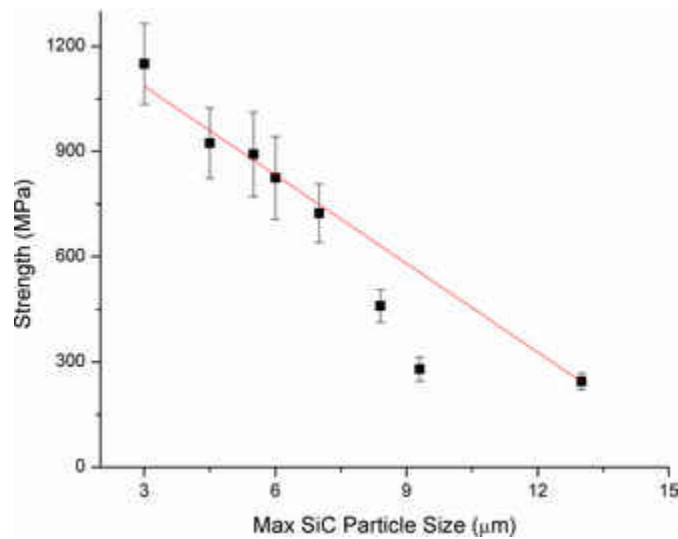
Figure 20: Strength as a function of the maximum SiC size measured as a circular diameter indicating that the ZrB₂-30vol%SiC milled for 1 hour and the ZrB₂-30vol%SiC milled for 2 hour compositions do not follow the linear trend that was suggested in the previous studies [54].

25
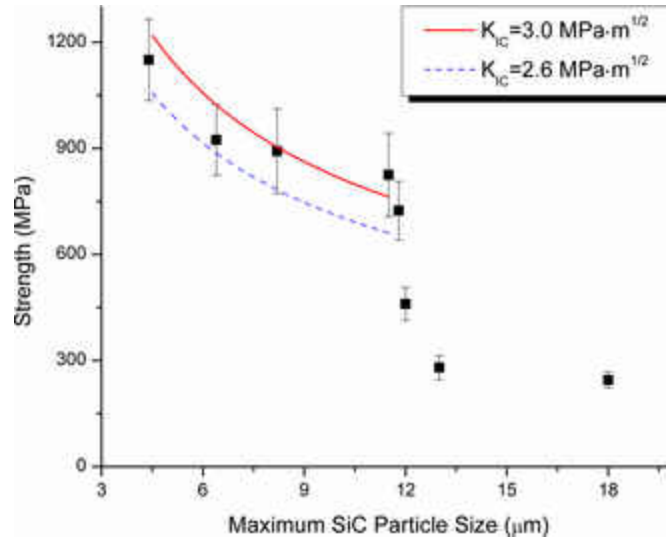
Figure 21: Strength as a function of maximum SiC particle size measured as the major axis of an ellipse for ZrB$_2$–SiC composites showing a 1/c1/2 relationship up to 11.5 lm at which point strength decreased more rapidly. Lines indicate predicted flaw size based on the Griffith criteria using a Y parameter of 1.98 and the indicated values of K$_{1C}$ [54].

The effect of sintering temperature on the strength of ZrB2-SiC has also been researched. One finds that, for 40 mass% SiC in the ceramic composites, an optimum temperature of 2000ºC gave the strongest sample same as shown below in Figure 22, and for the 50mass% SiC ceramic composites, maximum strength was reached at 1900ºC and increasing the sintering temperature decreased the strength of the sample.

26
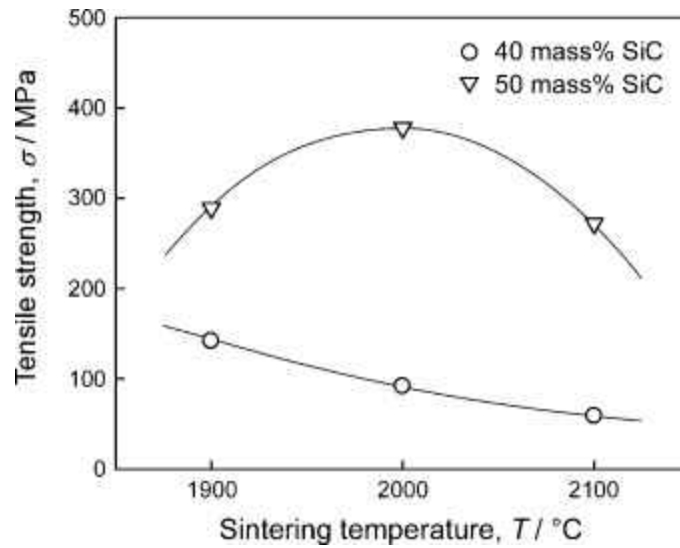
Figure 22: Effect of sintering temperature on the tensile strength of ZrB$_2$–SiC composites containing 40 and 50 mass% SiC sintered at 1900–2100 ºC [39]

Now looking at the hardness of the ZrB$_2$-SiC, one finds the following general trend; increasing the SiC content until around 50mass% increases the Vickers hardness and the fracture toughness of the ceramic composite but by further increasing the SiC content, the Vickers hardness and fracture toughness begin to decrease with a low at pure SiC. These trends are clearly visible in Figure 23 and Figure 24, which show the Vickers hardness and the fracture toughness, respectively. Figure 24 and Figure 25 below show the effects of hardness with the increase of SiC grain size. This aligns with the other trends found in Tables 4 and Table 5 above, which show that the SiC grain size increases, the hardness of the ceramic composites decreases. These graphs show both Knoop and Vickers hardness test, which both show the same type of trend.
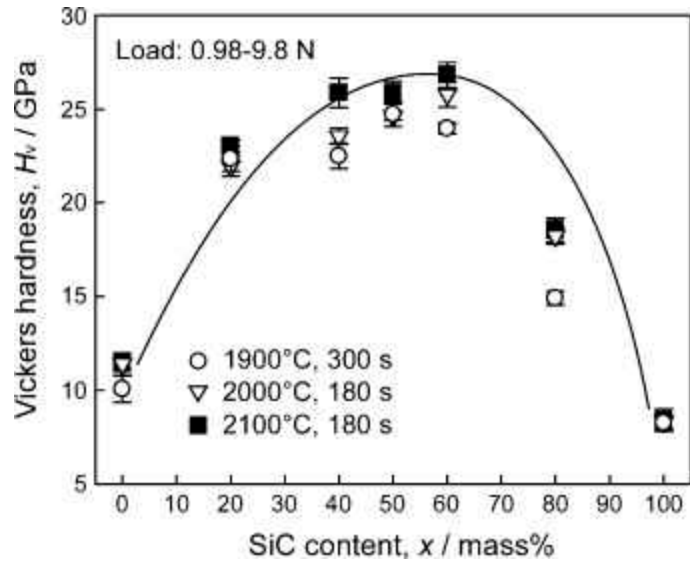
Figure 23: Effect of SiC content and sintering temperature on the Vickers hardness of ZrB$_2$–SiC composites sintered at 1900–2100 °C [39].
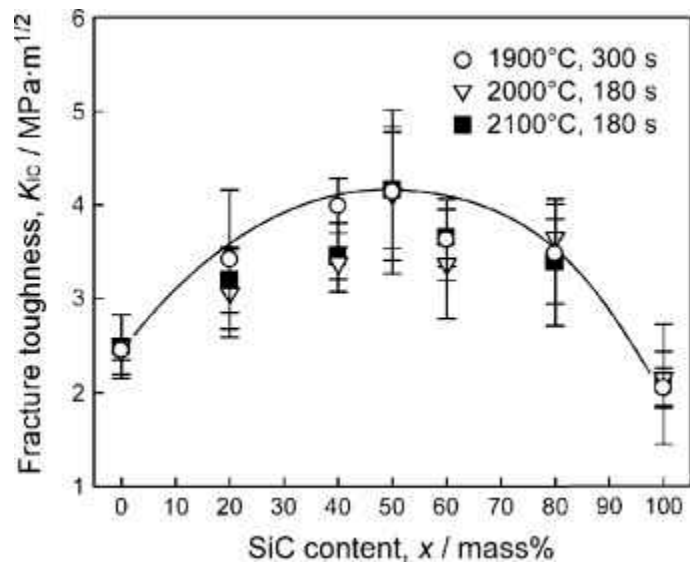
Figure 24: Effect of SiC content and sintering temperature on the fracture toughness of ZrB$_2$–SiC composites sintered at 1900–2100 °C [39].
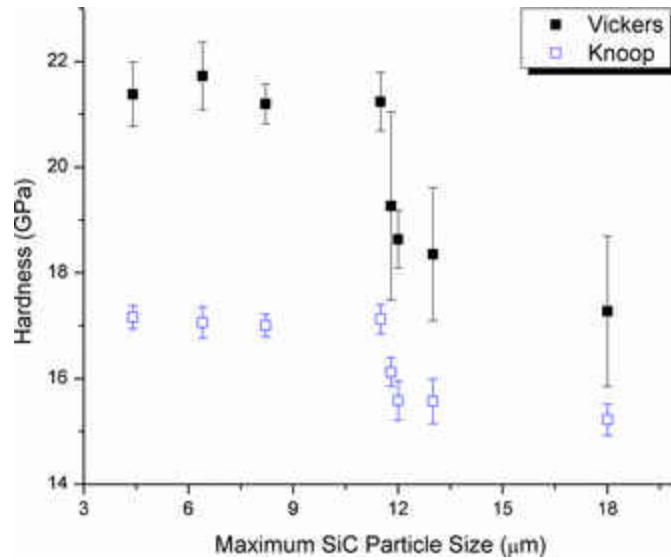
Figure 25: Hardness as a function of maximum SiC particle size measured as the major axis of an ellipse exhibiting a discontinuity for particle sizes greater than 11.5 μm [54].

In addition to the hardness and the fracture strength, the Young's Modulus or elastic modulus was also investigated with the effects of the maximum SiC particle size. One again finds the trend to be that as the SiC particle size increases, the Young's Modulus decreases. This is shown in Figure 26 below.

29
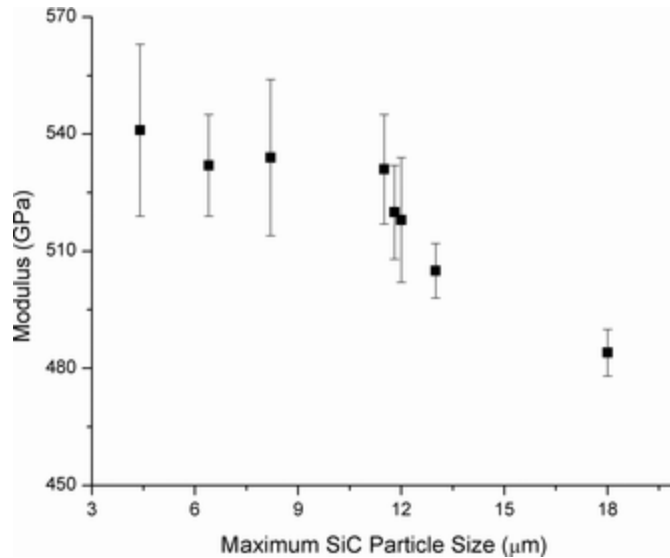
Figure 26: Elastic modulus as a function of the maximum SiC particle size measured as the major axis of an ellipse showing a reduction in modulus for composites containing SiC particles larger than 11.5 μm [54].

The mechanical properties of ZrB_2-SiC have also been investigated at elevated room temperatures. Hu conducted a 3-point bending flexure strength test of ZrB_2-15vol%SiC and ZrB_2-30vol%SiC at a temperature of 1800°C [57]. Figure 27 below shows the results of this test by Hu, including the load vs. displacement curve for the test.
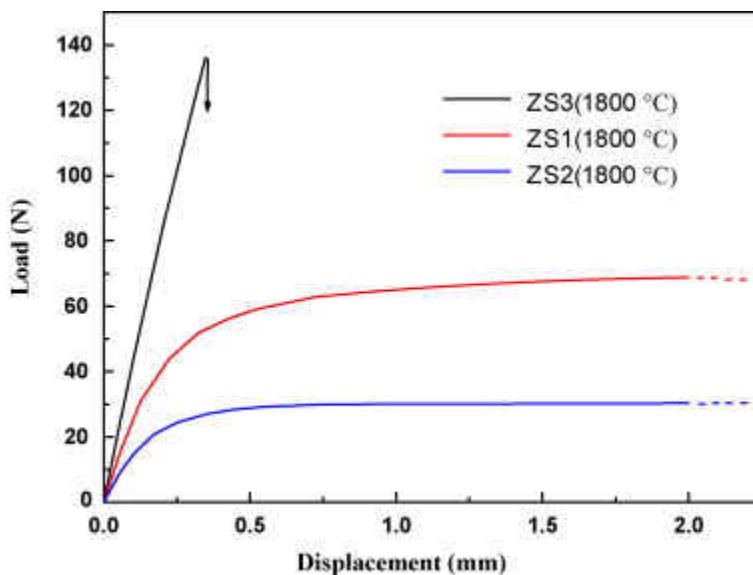
Figure 27: Load–displacement curves as obtained from three-point bending experiments conducted at 1800 °C [57].

Other experiments have been conducted to investigate the effects of temperatures on the strength of ZrB₂-SiC. Neumen investigated the Young's Modulus and flexure strength with respect to temperature and compared that to other experiment done previously. Figure 28 show the results of Young's Modulus, and Figure 29 shows the results of Flexure Strength. These Figures also show the results done initially by Rhodes earlier in 1970, when this ceramic composites was first studied [58, 59]. Bird also conducted experiments on temperature-dependent mechanical and long crack behavior [60].
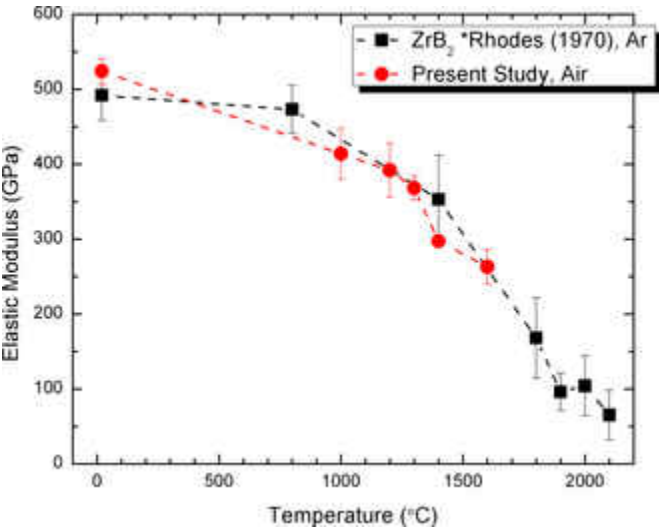
Figure 28: Elastic modulus of ZrB₂ tested in air atmosphere as a function of temperature [58, 59]

31
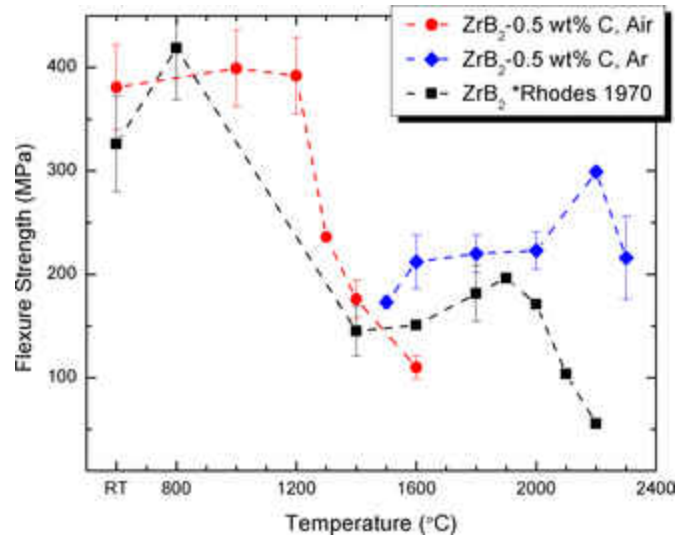
Figure 29: Four-point flexure strength of ZrB$_2$ ceramics tested in air (circles) and argon (diamonds) atmospheres as a function of temperature. For comparison, the data of Rhodes et al. (squares) are also shown [58, 59]

Fatigue is the life of a part under cyclic loading or environmental factors that a part or sample will encounter in the real world. There are many types of fatigue: cyclic loading, thermal cycling, and corrosion and rust resistance. Most of the papers in this section have been found to be mainly about thermal shock resistance. These papers were written by Zimmermann [61] and Meng [62]. Figure 30 below shows the results of thermal shock test done by quenching the samples in water. The points at which the strength the sample failed were plotted versus the change in temperature [61]. Zimmermann also investigated the depth of damage and stiffness as the temperature changed. Figure 31 below shows the results of strength of samples after a number of thermal shock cycles from Meng [62].

32
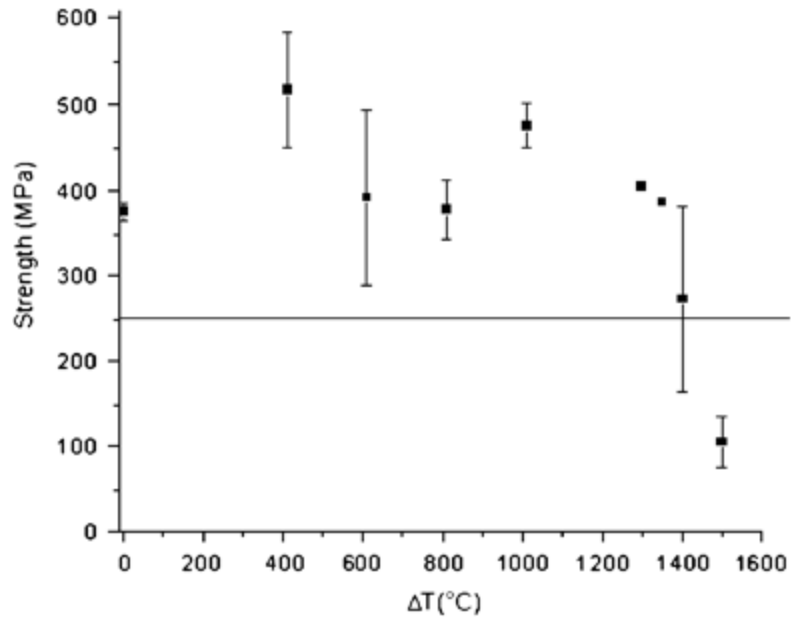
Figure 30: Strength values as a function of the change in temperature (ΔT) for fibrous monolith specimen quenched into water (27 °C) [61]
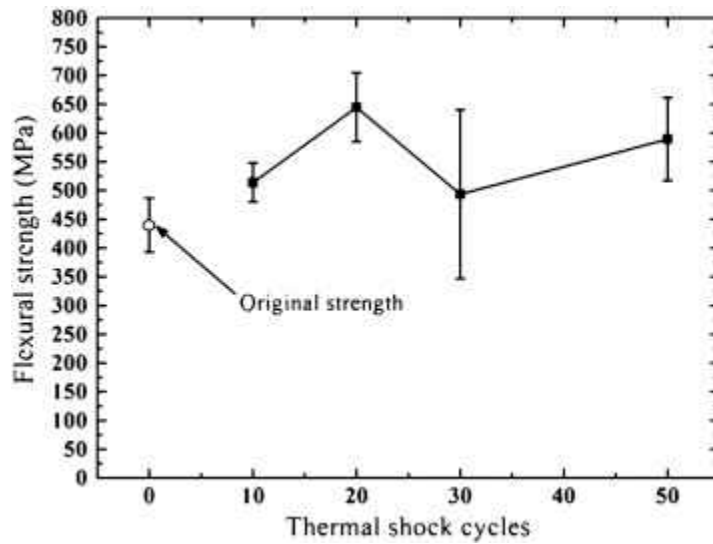
Figure 31: Effect of increasing number of shock cycles on the flexural strength [62].

Other types of fatigue are crack growth behavior and Mode I fracture toughness have been investigated by Bird [60] and Kurihara [63], respectively. Figure 32 below shows the average crack length for a compressive load applied to a sample.
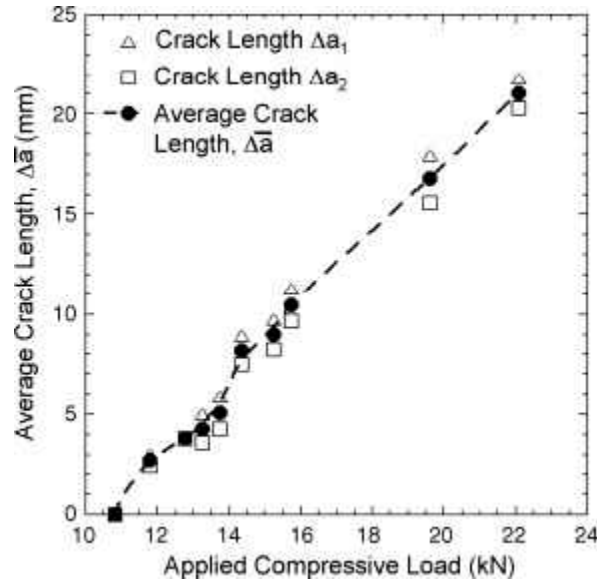
Figure 32: An example of applied load versus crack lengths [63].

Environmental and creep effects have also been studied by Orlvskaya [64] on ZrB_2-30wt%SiC ceramic composites.

Many papers have been published on oxidation results and oxidation resistance of ZrB_2-SiC ceramic composites. Such papers were written by Mallik [65], Tian [66], Hu [67], Guo [68], Opeka [6], and Han [69]. All of these papers were about oxidation and oxidation resistance. In addition to just looking at the oxidation mechanisms, tests were conducted with torches and high enthalpy flow using arc-jet test and plasma torch. These tests were done to simulate the intense heating of the leading edge upon re-entry. Figure 33 below shows the before and after images of one such test, using an oxyacetylene torch. Looking at the specimen after the test, one notices the

sample is no longer smooth and is charred, showing the effects of oxidation on the sample. In Figure 34, one can see the shear stress encountered by the samples during the test. Figure 35 shows the results of a plasma wind tunnel test of not only a blunt sample but also one with a sharp cone. Figure 36 shows a SEM image of the surface of the sharp cone, showing the creators as a result of oxidation and the high speed flow effects on the sample.

Figure 33: ZrB$_2$–20%SiC specimen before (left) and after (right) oxyacetylene torch testing at 2200 °C for 10 min [69].
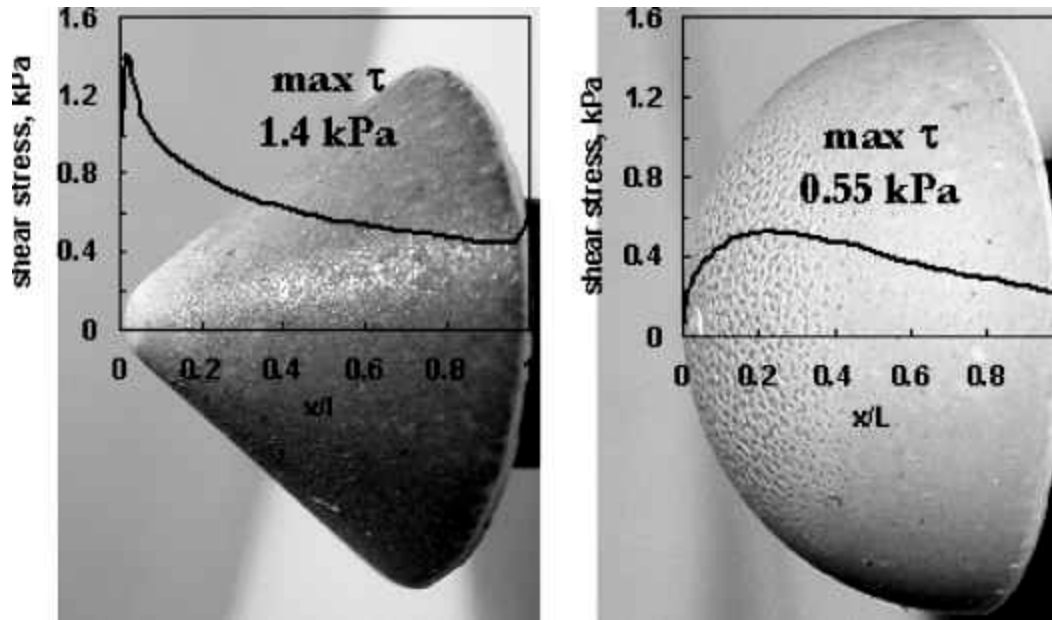
Figure 34: Shear stress vs. curvilinear normalized coordinate (x/L) [45]
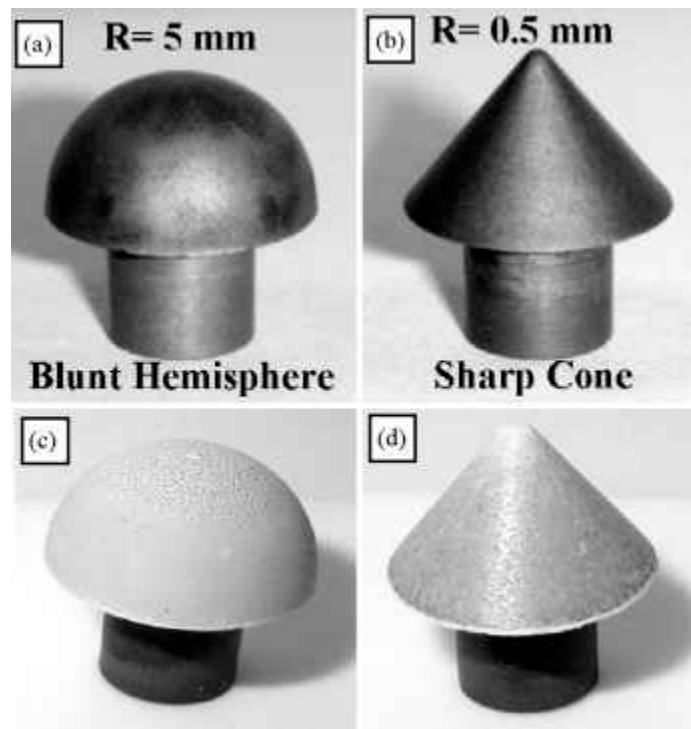
Figure 35: Visual appearance of the ceramic models before (a and b) and after testing (c and d); *R*: radius of curvature [70].

36
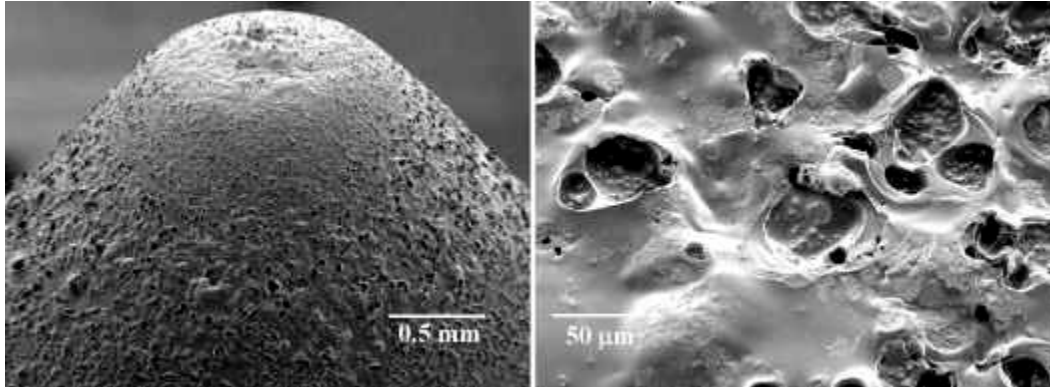
Figure 36: Exposed surface of the sharp cone: details by SEM [70].

In addition to oxidation tests, ablation tests have been conducted on sharp model leading edges. Figure 37 below shows the results of an ablation test with before and after pictures. Labels (a) and (b) on the figure are the before and after picture of the ZrB_2-SiC during the test. Looking at Figure 37 (a) and (b) labeled a and b, one sees that not only is there very little difference between the before and after, but also that the sample retained its shape. While looking at (c) and (d) of Figure 37 of SiC/C sample, one sees that there are significant changes in the shape, which would most likely result in failure. This experiment was conducted by Zhang [71]. Other publication on ablation have been found such as Li [72], and Tang [73], which just like Zhang investigated the effect of ablation on samples of UHTC.
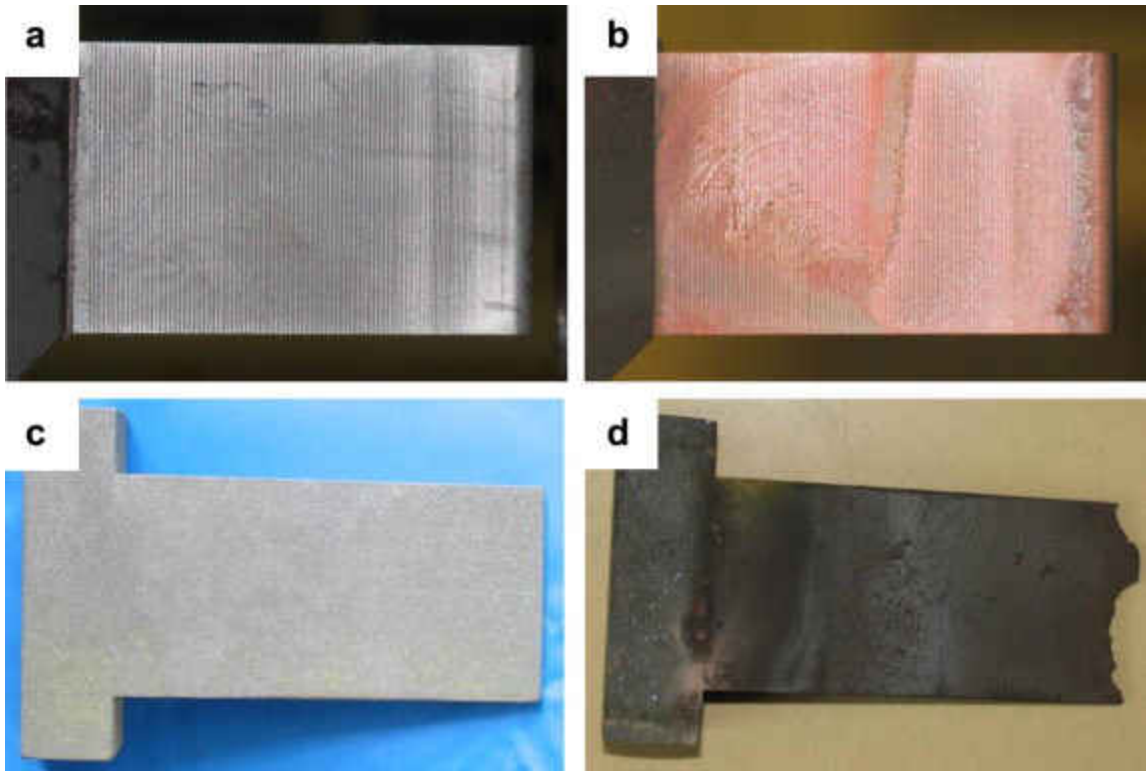
Figure 37: Photographs of the sharp leading edge models before ((a) and (c)) and after ((b) and (d)) ablation testing. (a) and (b): ZrB$_2$–SiC [71]

Recent papers have been published on the design and theory of materials for use with hypersonic and re-entry to the Earth's atmosphere. One such paper, by Savino, was an aerothermodynamics study of UHTC for thermal protection [74]. Another publication, by Oplia, was on ceramic materials for extreme environment applications. Finally, Parthasarathy published a paper about developing a test to evaluate aerothermal responses of materials for hypersonic applications [75].

<p style="text-align:center;">2.8: Raman Spectroscopy of ZrB_2-SiC</p>

Now looking at the Raman Spectroscopy of ZrB_2-SiC, one only finds SiC peaks, since ZrB_2 has not been previously reported as Raman active. This means either that ZrB_2 does not have any peaks at all in the spectra or the peaks are so small that they are not noticeable compared to the intensity of the SiC peaks. Conducting a search about this composition, one finds that each of the SiC polytypes have their own Raman spectra and are different from each other, even though most of the time they share the same peak position. Table 6 below shows a summary of the Raman peak position of each of the common types of SiC polytypes being used today in industry and research.

Table 6: Raman frequencies of the folded modes for typical SiC polytypes. Only the FTA and FTO modes with E(E1, E2) symmetry and FLA and FLO modes with A1 symmetry are shown [76]

Polytype		Frequency(cm^{-1})			
		Planar acoustic	planar optic	axial acoustic	axial optic
	$z=q/q_b$	FTA	FTO	FLA	FLO
3C	0	-	796	-	972
2H	0	-	799	-	968
	1	264	764	-	-
4H	0	-	796	-	964
	2/4	196,204	776	-	-
	4/4	266	-	610	838
6H	0	-	797	-	965
	2/6	145,150	789	-	-
	4/6	236,241	-	504,514	889
	6/6	266	767	-	-
8H	0	-	796	-	970
	2/8	112,117	793	-	-
	4/8	203	-	403,411	917,923
	6/8	248,252	-	-	-
	8/8	266	768	615	-

Polytype		Frequency(cm^{-1})			
		Planar acoustic	planar optic	axial acoustic	axial optic
	$z=q/q_b$	FTA	FTO	FLA	FLO
15R	0	-	797	-	965
	2/5	167,173	785	331,337	932,938
	4/5	255,256	769	569,577	860
21R	0	-	797	-	967
	2/7	126,131	791	241,250	-
	4/7	217,220	780	450,458	905,908
	6/7	261	767	590,594	-

The three most common polytypes are 3C, 4H and 6H. The spectra of each of these are shown in Figure 38 for 3C, Figure 39 for 4H, and Figure 40 for 6H polytypes. Looking at the three spectra, one finds that 4H, 6H and 3C share two peaks: the TO and the LO peaks. In addition, 4H and 6H have additional peaks in lower than 600 Raman shift named the FTA peaks.
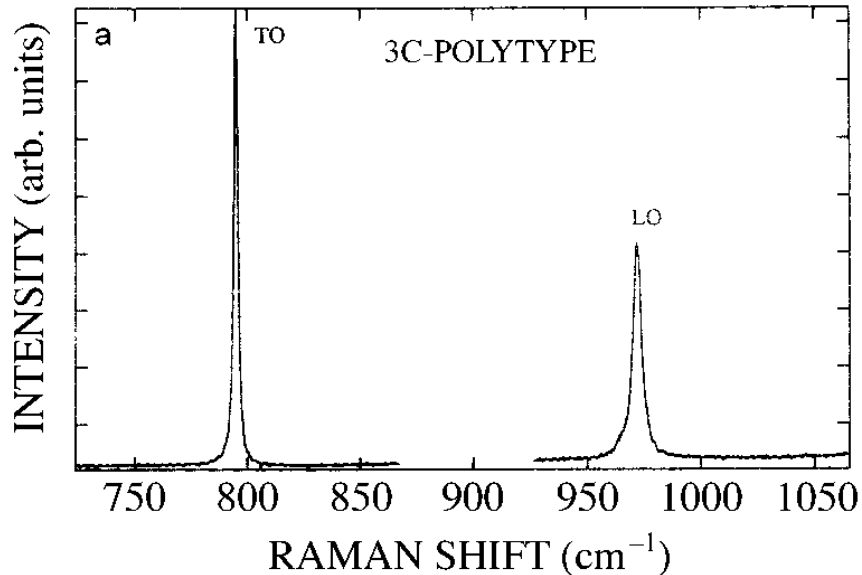
Figure 38: Raman spectra measured with a quasiback scattering geometry for 3C [76]

40
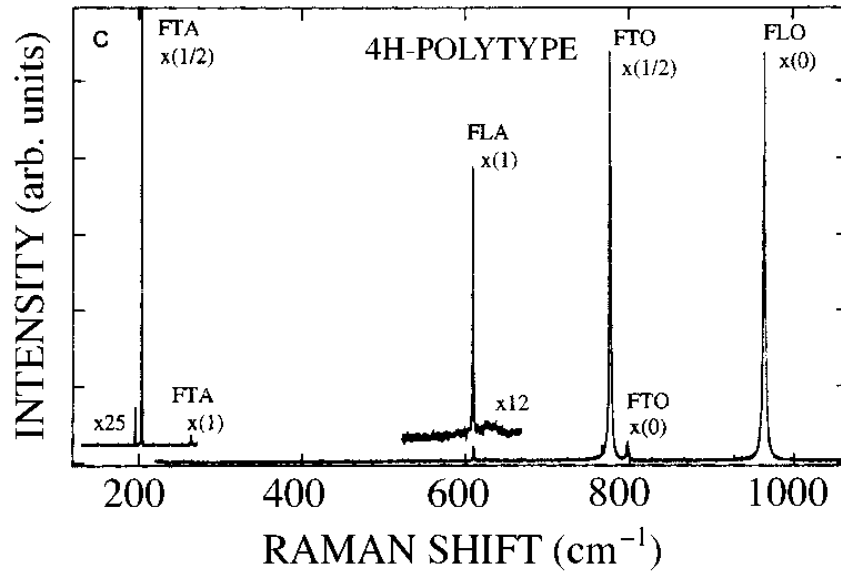
Figure 39: Raman spectra measured with a quasiback scattering geometry for 4H [76]
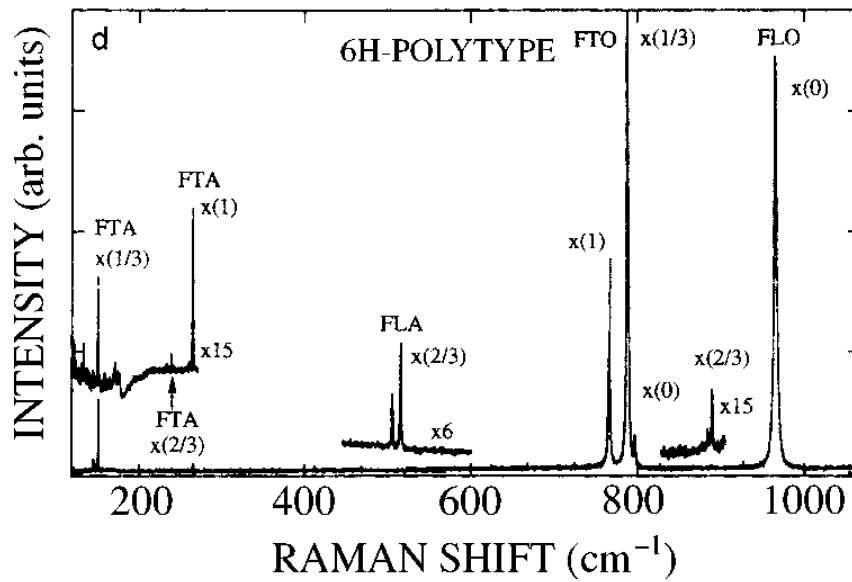
Figure 40: Raman spectra measured with a quasiback scattering geometry for 6H [76]

2.9: Piezo-Spectroscopy coefficient Using Raman Spectroscopy

ZrB_2-SiC ceramic composites have residual stress due to the mismatch of the coefficient of thermal expansion and the Young's modulus, and the difference between the sintering or processing temperature and room temperature. Since the residual stress distribution can affect the mechanical properties of the material, one would naturally want to find the distribution so that it can be altered to meet the specifications wanted. These residual stresses can be found using Raman spectroscopy, which is the method that will be used in this thesis to find the residual stresses in ZrB_2-SiC ceramic composites. This method has been used in ZrB_2-SiC [77], Yttria-Stabilized Zirconia [78], and SiC [79]. All of these experiments used compression to apply a load to a specimen under a Raman spectrometer. Watt was able to apply 0-90GPa compressive stress to ZrB_2-SiC and correlate an equation to give the reader the stress at a given point based on the change in the peak position from the stressed state to the unstressed state [77]. Figure 41 below shows a 6H-SiC Raman spectra in the stressed state compared to the unstressed state shown in red. One notices that the peak positions are shifted to the right from the un-stressed state. As a compressive stress is applied, the peak position of the Raman spectra shifts to a higher wavenumber, while if a tensile stress is applied, the peak shifts to a lower wavenumber.
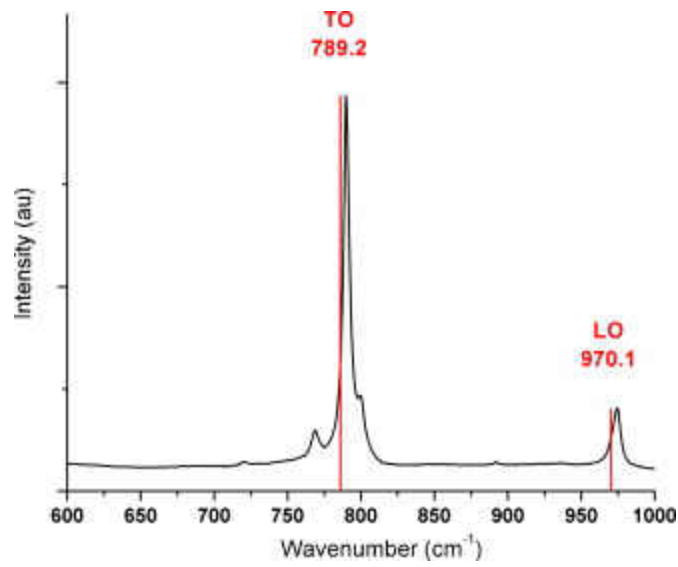
Figure 41: Raman pattern for 6H SiC from a hot pressed ZrB$_2$–SiC composite with unstressed peak positions identified with lines [77]

Another experiment on finding the piezo-spectroscopy coefficient was conducted by Grokecki on Bulk 6H-SiC [80].

CHAPTER 3: EXPERIMENTAL PROCEDURE

This section covers how each part of this thesis was conduct in order to get the results. The machines and model used as well as any other detail needed to replicate this research are included in this section of this paper.

3.1: Sample Fabrication and Density Measurements

Spark Plasma Sintering (SPS) technique was used to process the ZrB_2- 10,20, 30wt% SiC composites. Figure 42 below shows a picture of the SPS used to produce all of the samples. Three batches were prepared by weighing the ZrB_2 powder (H.C. Starck-ZrB_2 Grade B) and the SiC powder (H.C. Starck- Alpha -SiC Grade UF-10) in a certain proportion, and grinding them together in the plastic bottle, using ZrO_2-Y_2O_3 balls and acetone as a milling media. After 48 hours of grinding, the batches were dried up and sieved to break up the agglomerates. The sieved powders were loaded in the graphite die, using the graphite foil as an intermediate layer between the die and powder. The ZrB_2-10, 20, and 30 wt% SiC samples were sintered at 1950 ºC, 70 MPa, 100 ºC/min, heating and cooling rate, and dwell time of 15 minutes.

Figure 42: SPS Machine Picture

After grinding/removal of the graphite foil from the surface of the sintered samples, the density of the samples were determined using the liquid immersion technique, also known as the Archimedes method. In this method, one measures the mass of the sample in air and then measures the mass of the sample in acetone. Then using the two masses and the density of acetone, the densities of the samples were calculated using the following equation 1,

$$\rho = \frac{m_{air}}{m_{air} - m_{acetone}} \rho_{acetone} \qquad (1)$$

where m_{air} is the mass of the sample in air in grams, $m_{acetone}$ is the mass of the sample in acetone in grams, and $\rho_{acetone}$ is the density of acetone of 0.97g/cm^3 for 99% lab grade Fisher Scientific acetone. The scale used was a Mettler Toledo JB1603-C and is shown below as Figure 43.

Figure 43: Picture of the Mettler Toledo Scale

After the sample densities were calculated, the theoretical densities of the three compositions, ZrB_2-10wt%SiC, ZrB_2-20wt%SiC, and ZrB_2-30wt%SiC were calculated using the rule of mixtures, which is shown in the following equation 2 below,

$$Composite\ Density = v_1\rho_1 + v_2\rho_2 + \cdots + v_i\rho_i \tag{2}$$

where v_1 is the volume percent of the first component of the composite, $v2$ is the volume percent of the second component of the composite, v_i is the volume percent of the ith component of the composite, ρ_1 is the theoretical density of the first component of the composite, ρ_2 is the theoretical density of the second component of the composite, and ρ_i is the theoretical density of the ith component of the composite. Since the ceramic composites were produced using weight percent in order to calculate the theoretical densities, one must convert the weight percent to volume percent; this is done by using the following equation 3.

$$Volume\% = \frac{\frac{weight\%}{Density}}{Total\ Volume} * 100 \qquad \textbf{(3)}$$

3.2: Mechanical Properties Testing

2x2.5x25mm bars were machined out of the SPS samples at Prematech Advanced Ceramics, MA. Flexure strength was measured with the four-point test technique in accordance with EN843-1 standard. 5 samples were used for room temperature testing for each composition. The crosshead speed was set to 0.5mm/min. An MTS 810 Machine applied the load and is shown below along with the 4-point bending configuration in Figure 44. In the 4-point bending, the L_1 was 10mm and L_2 was 20mm, which is a standard loading and support span distance for flexure tests and fracture toughness tests as well.
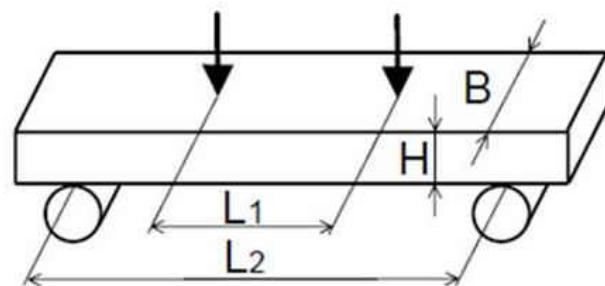
Figure 44: (a) MTS 810 system, (b) schematic diagram of the 4-point bending configuration, where H and B are the sample dimensions and L_1 is the loading distance and L_2 is the supporting span.

The flexure strengths of the samples were calculated using the following equation 4,

$$\sigma_f = \frac{3P(L_2 - L_{1)}}{2bh^2} \tag{4}$$

where σ_f is the fracture stress, P is the load at which the sample failed at, b is the base of the sample, h is the height of the sample and L_2 and L_1 are the 4-point bending distances as show above in Figure 44. For fracture strength part test, the base was 2.5mm and the height was 2mm. The dimensions of the samples were measured using a Mitutoyo Digital Micrometer with an uncertainty of 0.0005 mm. This results in more accurate dimensions of the samples than when using a regular caliper.

A scanning electron microscope (Zeiss-SEM) was used for the analysis of fracture surfaces of the ZrB_2-10, 20, 30wt% SiC bars after mechanical tests. A picture of the Zeiss-SEM is shown below in Figure 45. This analysis was done to find out the type of defects are the samples. Also what caused the samples to fail; was it dislocations, pores, or a scratch defect on the surface of the bar from machining the samples. The fracture origin was also sought in order to find out what was the biggest defect that caused the samples to fail. Three of the five samples of each composite composition were selected for investigation for both the flexure strength and the fracture toughness strengths. The three samples were selected based on the lowest, highest, and average loads at which the sample failed for each composition and test. Pictures were then taken of key surfaces of these samples at high resolution and are shown and described in the results section of this thesis.

Figure 45: Zeiss Ultra 55 SEM

Fracture toughness was measured using the Single Edge V Notch Beam (SEVNB) technique in accordance with the CEN/TS 14425-5 standard. A single notch was made on the 2 mm side of the 2x2.5x25mm bar as near to the center as possible with a depth between 20 to 40 % of the total depth of the bar, since it was shown that within this range, the depth of the notch has no influence on the K_{1c} values. The diamond saw was used to make the initial cut, which would bring the 0.5 mm of the notch, after that the final ~ 45μm tip radius was produced by manually cutting the notch with 15 and 3 μm diamond paste deposited on the razor blade. Five samples were tested at room temperature with the crosshead speed of 0.5mm/min, again using the same MTS system as the flexure strength and the same 4-point bending configuration the samples were loaded until failure. The 2.5mm side was the height and the 2mm side was the base

in this test. Once the testing was completed, a scanning electron microscope was used to take a picture of the fracture surface of the SEVNB. This was done by first making sure the fracture origin occurred at the notch tip in order to make sure that the test was valid. Then the average notch depth was checked to see if the 20-40% of the total depth of the bar was achieved. The average notch depth was measured using Adobe Photoshop software by using the scale on the picture itself. Then using the measuring tool in Adobe Photoshop, the depth of the notch was found. The depth of the notch was measured at four locations and then averaged. After the test was deemed valid, the fracture toughness was calculated using the following equation 5,

$$K_{1c} = \frac{F}{B\sqrt{W}} \frac{S_1 - S_2}{W} \frac{3\sqrt{\alpha}}{2(1-\alpha)^{1.5}} y \qquad (5)$$

where F is the fracture load, K_{1c} is the fracture toughness, B is the sample width, W is the sample depth, S_1 and S_2 is the support span of the 4-point bending device. In addition to these parameters, y and α need to be calculated using the following equation 6,

$$y = 1.9887 - 1.326 \alpha - \frac{(3.49 - 0.68 \alpha + 1.35 \alpha^2) \alpha (1-\alpha)}{(1+\alpha)^2} \quad and \quad \alpha = a/W \qquad (6)$$

where a is the average notch depth. Again five samples of each of the three composites were used in this test.

The Young's, bulk, and shear moduli along with the Poisson's ratio of materials were measured at room temperature using Resonant Ultrasound Spectroscopy (RUS). RUS is a highly accurate method for determining the resonant spectra of a sample of known mass, geometry and

dimensions [81-83]. The composite pallets 20 mm in diameter and 2-3 mm thick were placed on 3 transducers; one sent out ultrasonic waves at sweeping frequency and the other two transducers recorded the natural frequencies at which the sample was vibrating. For determining the elastic moduli of the examined materials from resonant spectra, it was assumed that the composite pallets are isotropic and thus only two elastic constants, i.e., C_{11} and C_{44} are required. From the known sample dimensions, density, and a set of "guessed" elastic constants C_{11}, and C_{44}, the first 40 resonant frequencies were calculated for each sample. A multidimensional software Quasar RuSpec (Magnaflux Quasar Systems, Albuquerque, NM) that iteratively minimizes error between the measured and calculated resonant frequencies by changing the initially "guessed" elastic constants was used to determine elastic constants for the set of measured resonant frequencies of the sample. The elastic constants C_{11} and C_{44} were further used to calculate Young's, shear and bulk moduli and Poisson's ration of the composite samples. It is worth noting here that fitting error, i.e. the root-mean-square (RMS) error between the measured and calculated resonant frequencies, never exceeded 0.3% for all tested samples.

3.3: Raman Spectroscopy and Residual Stresses

The Micro-Raman InVia Renishaw spectrometer was used to study the stress distribution in ZrB_2-SiC ceramic composites. The Raman microscope system comprises of a laser (532nm) to excite the sample, a single spectrograph fitted with holographic notch (beam splitter edge) filters, and an optical microscope (a Leica microscope with a motorized XY2 mapping stage, Figure 46 shows the entire Raman system) rigidly mounted and optically coupled to the spectrograph. The generated laser power was 25mW. The average collection time for a single spectrum varied from

50 to 300s per point. The incident and scattered beams were focused with a microscope using a 100x objective, which allowed for a laser spot as low as 1-2μm. All measurements were performed at room temperature. Before the ZrB_2-SiC measurements, the spectrometer was calibrated with a Si standard using a Si band position at 520.3 cm^{-1}.

Figure 46: Picture of the Renishaw Raman Spectrometer

In order to find the residual stress in ZrB_2-SiC ceramic composites, an *in-situ* bending Raman spectroscopy test needs to be performed. For the bending test, a 3-point bending device coupled with the micro Raman spectrometer was used. A senior design group built the 3-point bending device, and the device is shown below as Figure 47. The calibration and use of this device are mentioned in the results section of this thesis.
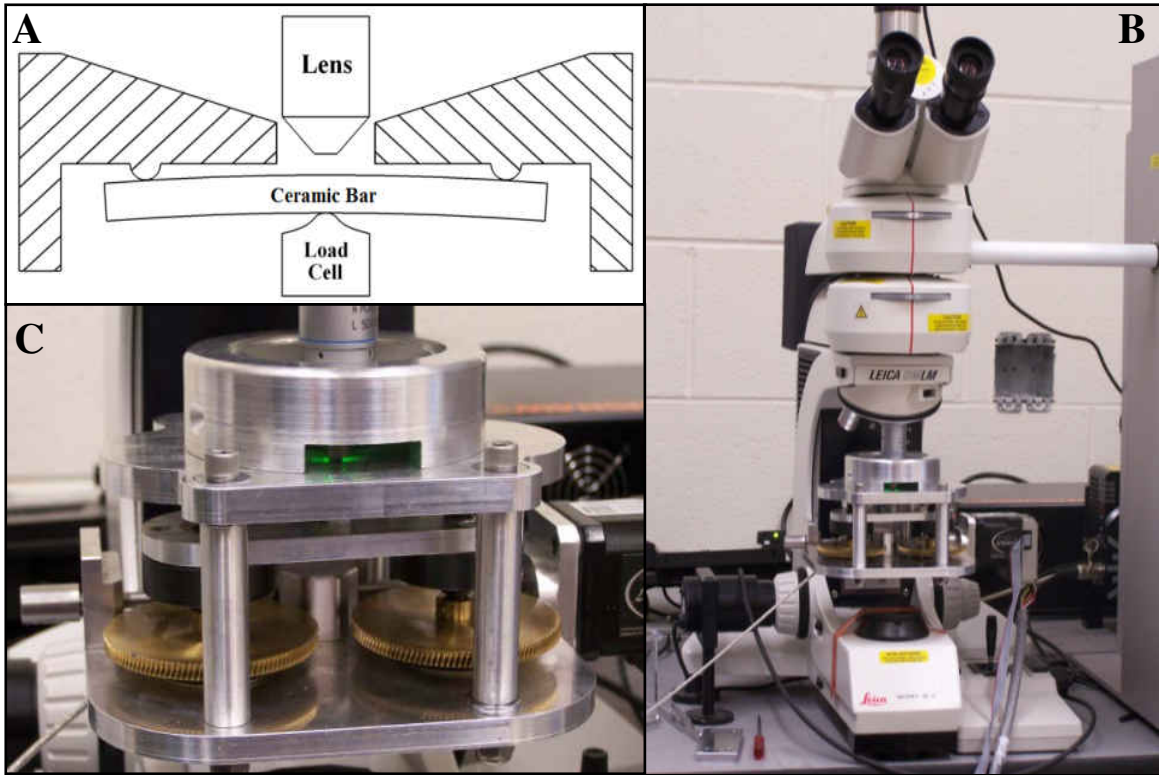
Figure 47: (a) Schematic of loading ceramic bar in three point bending for collection of *in-situ* scattered light. (b) A photograph of the *in-situ* loading device. (c) Loading device coupled with Leica optical microscope connected to InVia micro-Raman spectrometer.

While using the 3-point bending device described above, one found that the same exact point was not easily maintained. The Raman spectra must be collected at the same point throughout the entire *in-situ* bending experiment, since at different locations the peak position may be different and thus would throw off the data. Therefore, A XYZ motorized stage was also designed in order to allow the bending device previously designed to be moved so the same exact spot/area used to obtain the initial unloaded spectra could be found and held constant throughout the duration of the experiment. Figure 48 below shows the XYZ motorized stage used for this research.
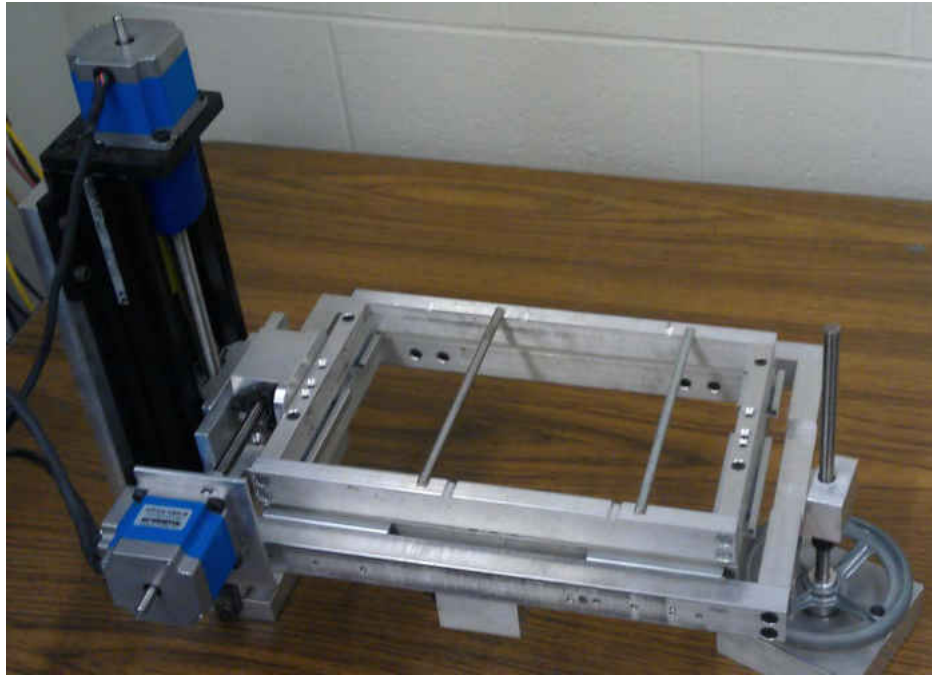
Figure 48: XYZ Stage design for 3-point bending device.

Bar samples were machined to the dimensions of 4mm x 1.5mm x 27mm, from a 50mm diameter sample that was SPS's at the same conditions as the samples made for mechanical testing, in order to achieve high loading stress for the load cell that the bending device is equipped with. The bending experiment was carried out by first loading the sample into the device, and then taking a Raman spectrum at the 0 stress state, and then loading in 20MPa increments to 300MPa. The Raman spectra were taken at each of the intervals using the following parameters: Raman Shift range 700-1100 cm^{-1}, exposure time 200 seconds, 532 nm laser, long working distance 50x objective lens, and 50% laser power. This was held constant for all of the bending experiment conducted. Throughout the experiment, the location at which the Raman spectra was collected was monitored to make sure the same exact location only was collected. Once the experiment was complete, the spectra was curve fitted. Then the center of

each of the LO and TO peaks were plotted against stress to find a correlation. The entire set up of the experiment can be seen in Figure 49 shown below.

Figure 49: *In-situ* **Raman Spectroscopy bending experiment Set-up**

For mapping, Raman scattering was performed on the mechanically polished (1μm diamond) surface. The representative 20x20μm area on the surface of the ceramic has been chosen. The area mapping was conducted with a laser having a spot size of 1μm. Autofocusing was used to collect the Raman spectra because it maintains a good focus on the sample during line/area confocal mapping experiments. To produce two dimensional (2D) maps, Renishaw Wire-2 software with a mixed Lorentzian and Gaussian peak fitting function was used. The system was set up to take spectra from all points inside the selected area of interest. Peak positions determined by peak fitting were plotted to create a strain map with a spectral resolution better than 0.1 cm^{-1}. The total acquisition time to collect all spectra for one map was 12 hours.

CHAPTER 4: RESULTS & DISCUSSIONS

The results of this thesis were separated into sections starting with the processing, then the mechanical properties, followed by the Raman results and finally the Piezo-Spectroscopy coefficient.

4.1: Spark Plasma Sintering of ZrB_2-SiC Ceramic Composite

While the samples were being SPSs the pressure, temperature and displacement history were all record in order to form the shrinkage plot of the sample sintering. Figure 50 below shows this shrinkage plot. Looking at this figure, one notices numbers; these numbers correspond to distinct points in the sintering process. Point #1 marks the start of the pressure being applied to the sample. Point #2 is the point where 50MPa was reached and held constant. Point #3 marks the point where the sample starts sintering. Point #4 marks where the holding temperature 1950ºC was reached. Point #5 marks the end of the holding temperature. At this point the sample is starting to be cooled where it shrinks more due to temperature. Point #6 marks where the pressure is being removed and point #7 marks the point where there is no more pressure being applied, and the sampling continuing to shrink due to the cooling and the coefficient of thermal expansion. Looking at the figure again between point #4 and point #5, one sees the sample shrinks very little; this is believed to be because the sample has already finished sintering.
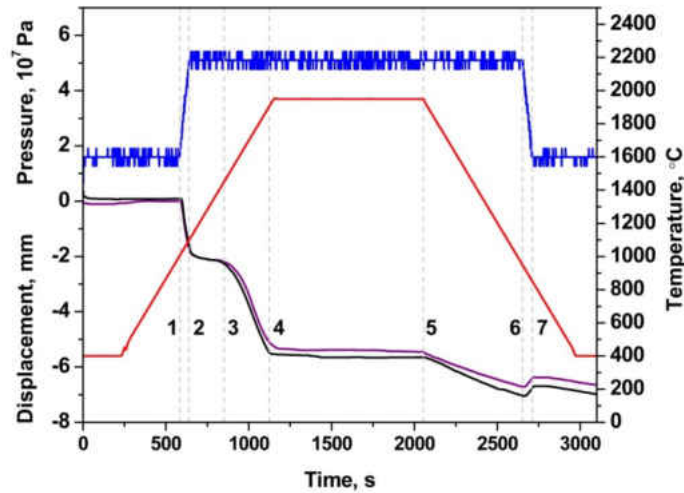
Figure 50: Shrinkage Plot for all three composites

Before calculating the density of each sample sintered, the theoretical density of the 3 compositions of interest, ZrB_2-10wt%SiC, ZrB_2-20wt%SiC and ZrB_2-30wt%SiC needs to be calculated. The theoretical densities were calculated using the rules of mixture and the theoretical density of ZrB_2 of 6.1 g/cm^3 and SiC of 3.21g/cm^3. The rules of mixtures are based on volume percent instead of weight percent, thus one needs to convert the weight percent into volume percent. The weight percent is converted to volume percent using equation 3 as shown in the experimental section of this thesis. The conversion of mass percent to volume percent for each of the composition is shown below as Table 7.

Table 7: Volume Percent Calculations

	wt%ZrB_2	wt% SiC	vol% ZrB_2	vol% SiC
ZrB2+10wt%SiC	90	10	82.59	17.41
ZrB2+20wt%SiC	80	20	67.83	32.17
ZrB2+30wt%SiC	70	30	55.15	44.85

Now that the volume percent is calculated, one can now calculate the composite theoretical densities. This is done by using the rules of mixtures equation. The rules of mixtures are described in the experimental procedure section of this thesis as equation 2. The calculated theoretical densities are shown below in Table 8.

Table 8: Composites Theoretical Density

	vol% ZrB2	vol% SiC	Theoretical Density(g/cm^3)
ZrB2+10wt%SiC	82.59	17.41	5.59
ZrB2+20wt%SiC	67.83	32.17	5.16
ZrB2+30wt%SiC	55.15	44.85	4.80

After the samples were sintered, the densities of the samples were measured using the Academies method described above in the experimental procedure section with equation 1. The densities of each of the three compositions were average and plotted as shown in Figure 51 below. The porosity of the samples was also calculated by using the theoretical density of each composition; the average results with error are also shown in Figure 51 below. The density of each of the samples was measured and averaged to get the data shown in Figure 51. In addition, the effects of sintering temperature on sample density for each composition were investigated and are shown below in Figure 52, Figure 53, and Figure 54 below. Looking at these figures, one sees for all three of the compositions, that around 1950 ℃, the samples are close to theoretical density of each composition. Thus one can conclude that this temperature is a good temperature to sinter the sample to get close to a fully dense sample. Included with the 20 and 30 weight percent composites is the density of each of the bar samples used to conduct the *in-situ* Raman bending experiment to compare with the other samples used for mechanical testing.
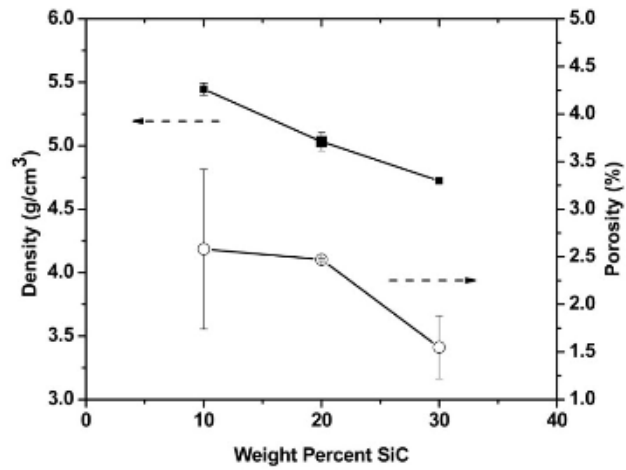
Figure 51: Density & Porosity of Sintered Samples
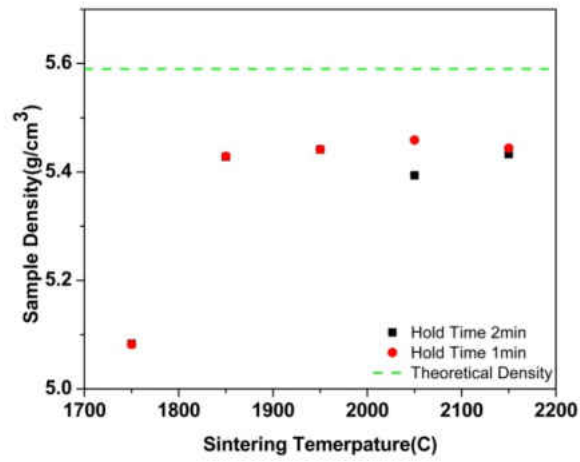
Figure 52: ZrB$_2$-10wt%SiC sample density comparing to sintering temperature
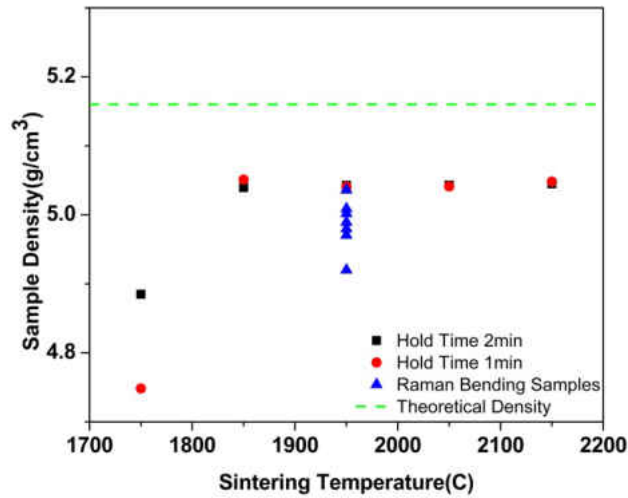
Figure 53:ZrB$_2$-20wt%SiC sample density comparing to sintering temperature
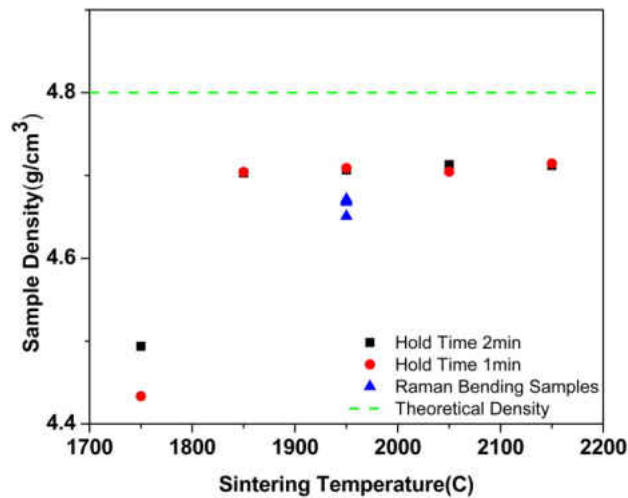
Figure 54:ZrB$_2$-30wt%SiC sample density comparing to sintering temperature

After the density and porosity were found, the SiC grain size distribution were also found for each composition, which is shown below in Figure 55 for ZrB$_2$-10wt%SiC, Figure 56 for

60

ZrB$_2$-20wt%SiC and Figure 57 for ZrB$_2$-30wt%SiC. Next to each of the grain size distribution graphs is a confocal micrograph of the sample surface of all three ceramic composite compositions. This is done in order for one to see the different between the three composites and why the average grain size can be different between the composites. The black spots are SiC and the gray area is ZrB$_2$ for all of the confocal micrographs. Table 9 below shows the summary of the grain size distribution. Looking at this table, one sees that, as the weight percent of SiC is increased, the mean grain size increases as well. This makes sense; since there is more SiC, the bigger grains can form.

Table 9: SiC Grain Size Distribution

Composite	# SiC Grains	mean(µm)	Standard Deviation(µm)
ZrB2-10wt%SiC	94	1.484	0.977
ZrB2-20wt%SiC	100	1.833	1.4
ZrB2-30wt%SiC	98	2.122	1.48
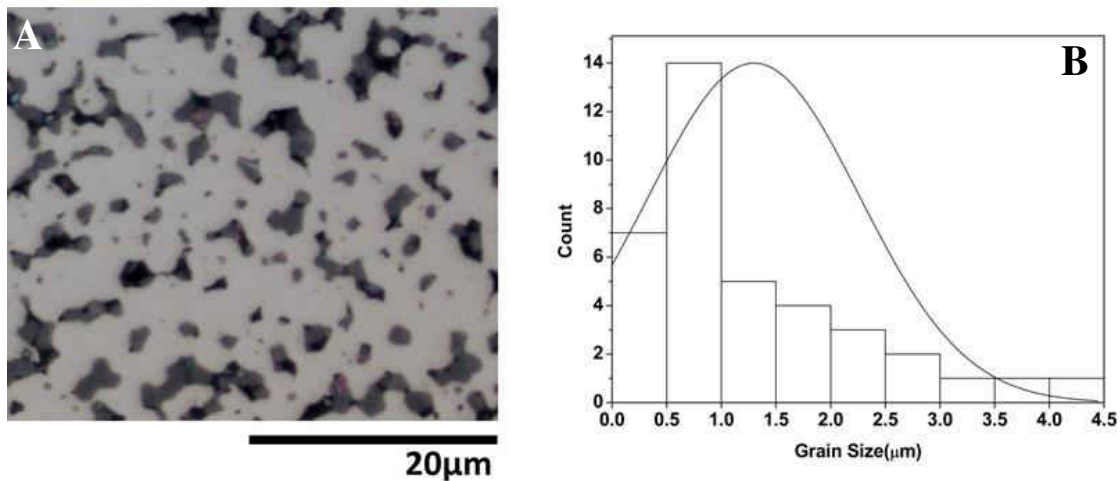
Figure 55: Confocal micrograph image of a polish surface of ZrB$_2$-10wt%SiC (a) and grain Size distribution (b)
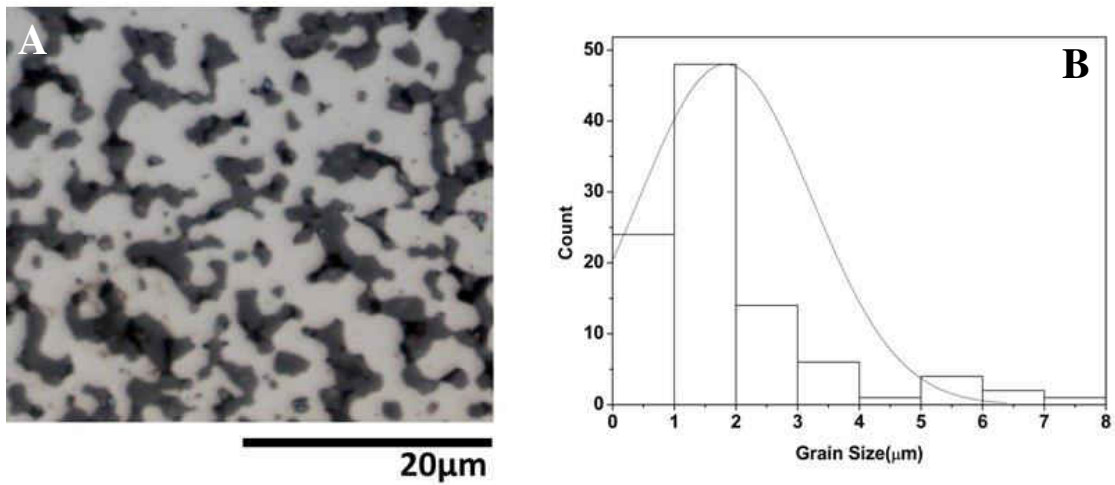
Figure 56: Confocal micrograph image of a polish surface of ZrB$_2$-20wt%SiC (a) and grain Size distribution (b)
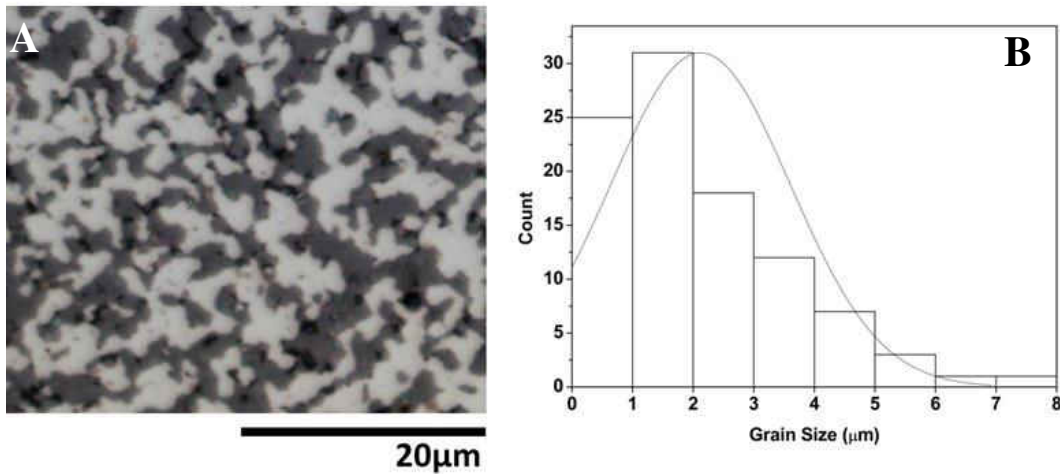
Figure 57: Confocal micrograph image of a polish surface of ZrB$_2$-30wt%SiC (a) and grain Size distribution (b)

4.2: Mechanical Properties of ZrB$_2$-SiC Processed by SPS

After calculating all of the densities and the sintering properties of the samples, one is interested in the mechanical properties of the samples; first is the fracture strength or flexure strength. This test was conducted using an MTS machine applying a load with the sample being

loaded in a 4-point bending configuration. Load was applied to the sample until the sample failed, or broke. The stress at which the sample failed at is called the flexure strength or fracture strength. This stress is calculated based on the sample's dimensions, 4-point bending distances, and finally the load at which the sample failed. Equation 4 in the experiment section of the report shows how to calculate the fracture strength. The average results with the standard error are shown below as Figure 61. Looking at this figure, one sees a general trend that as SiC weight percent increases, the strength of the samples, on average, increases. This agrees with other results in literature shown in the literature search section of this thesis. Table 10 below shows the results of each of the five samples flexure strength used to make the graph shown in Figure 61.

Table 10: Flexure Strength Results

Composite	Sample	Sample Base (mm)	Sample Height (mm)	Supports Span (mm)	Load Span (mm)	Maximum Load(N)	Breaking Stress(Mpa)
ZrB2-10%wtSiC	1	2.5019	1.9939	18.22	9.64	346.64	448.28
	2	2.4892	1.9939	18.22	9.64	449.60	584.40
	3	2.4892	1.9939	18.22	9.64	395.05	513.49
	4	2.5019	1.9812	18.22	9.64	446.12	584.36
	5	2.4892	1.9939	18.22	9.64	256.44	333.32
ZrB2-20%wtSiC	1	2.4765	1.9177	18.22	9.64	395.27	558.27
	2	2.4384	1.9177	18.22	9.64	229.56	329.30
	3	2.5019	2.0320	18.22	9.64	420.59	523.71
	4	2.4892	2.0066	18.22	9.64	421.27	540.66
	5	2.4892	1.9558	18.22	9.64	408.83	552.31
ZrB2-30%wtSiC	1	2.4257	1.8796	18.22	9.64	555.73	834.15
	2	2.4384	1.9431	18.22	9.64	417.67	583.56
	3	2.413	1.9304	18.22	9.64	533.80	763.62
	4	2.4384	1.8796	18.22	9.64	484.68	723.71
	5	2.4384	1.9177	18.22	9.64	496.81	712.64

After calculating the fracture strength, SEM images of the fracture surfaces were taken. These images are shown below as Figure 58, for ZrB_2-10wt%SiC, Figure 59 for ZrB_2-20wt%SiC, and Figure 60 for ZrB_2-30wt%SiC. These figures show the fracture surface of the samples taken by SEM using the secondary electron source. Looking at this fracture surface, one notices that the sample that fractured at the higher strength had a smoother surface. This is most likely due to the fact that the major defect that led to failure was not a surface defect, such as a scratch from machining the sample.
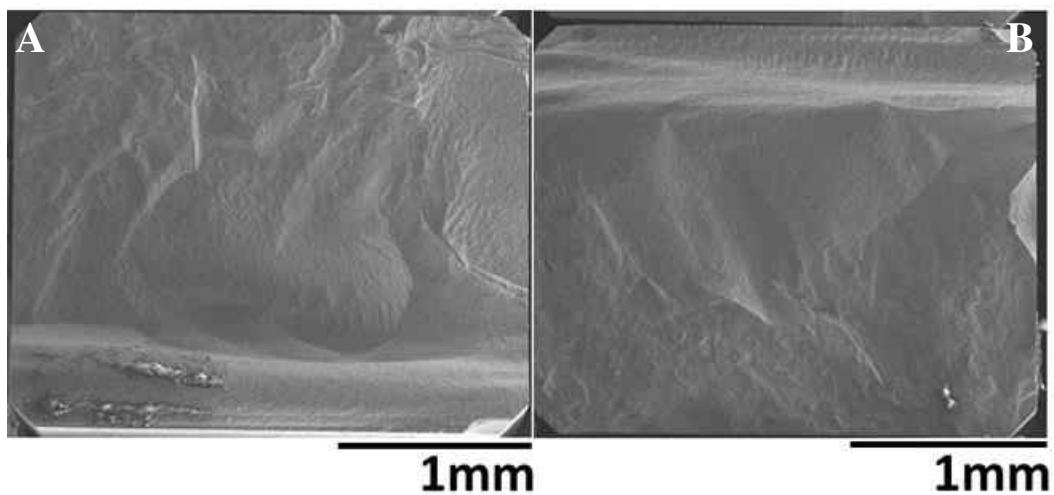
Figure 58: ZrB$_2$-10wt%SiC SEM Image of the fracture surface of the Maximum strength sample (a) and the average strength samples (b)
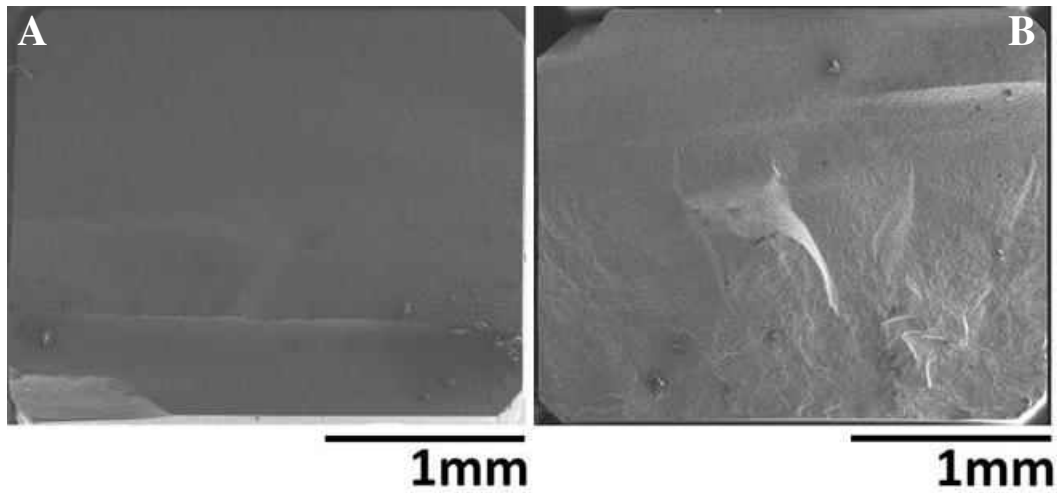
Figure 59: ZrB$_2$-20wt%SiC SEM Image of the fracture surface of the Maximum strength sample (a) and the average strength samples (b)
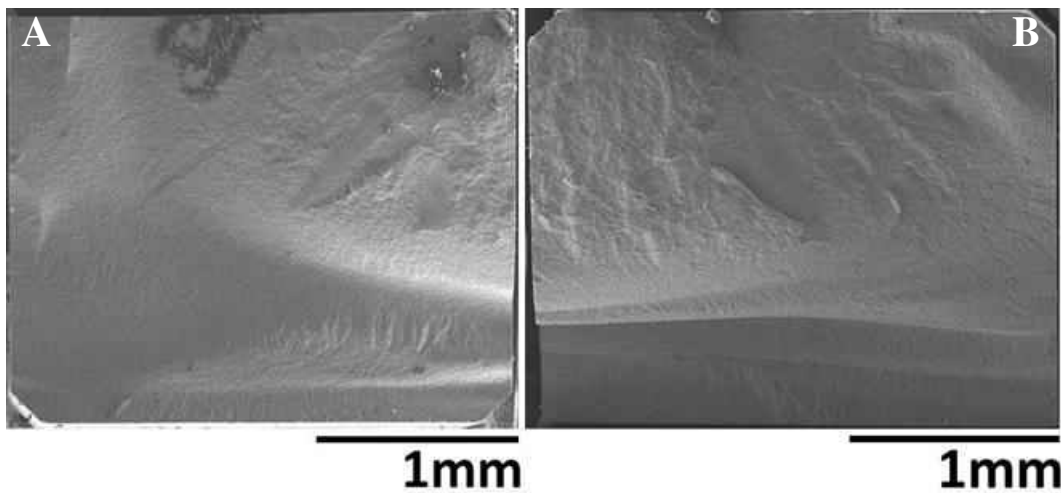
Figure 60: ZrB$_2$-30wt%SiC SEM Image of the fracture surface of the Maximum strength sample (a) and the average strength samples (b)

Following the fracture strength test, the fracture toughness test was conducted by using a single edge V-notch beam (SEVNB). This experiment was conducted by physically making a V-notch in a sample, then using the sample 4-point bending configuration as the fracture strength

65

and loading it until failure. Figure 61 again shows the results of the fracture toughness with the average value for each composition with standard error. Again the trend is, as the SiC weight percent increased, the fracture toughness increased as well. This also agrees with literature just like the flexure strength test did. Table 11 shows the calculated result of each sample that was used to construct the graph of fracture toughness shown in Figure 61.

Table 11: Fracture Toughness Results

Composite	Sample	Width (mm)	Height (mm)	Max Load(N)	a(mm)	Alpha	K1c (MPa/m^1/2)
ZrB2-10wt%SiC	8	1.9939	2.5146	33.046	1.176	0.468	2.814
	9	2.0193	2.5019	29.482	1.105	0.442	2.315
	12	2.0193	2.5019	44.772	0.870	0.348	2.727
	14	2.0066	2.4765	25.816	1.120	0.452	2.137
	15	1.9431	2.4892	46.909	0.767	0.308	2.699
ZrB2-20wt%SiC	7	1.9685	2.5019	44.723	0.828	0.331	2.673
	8	2.0066	2.5019	35.070	0.971	0.388	2.392
	9	1.9939	2.5019	37.403	0.900	0.360	2.379
	11	2.0066	2.5146	44.443	0.880	0.350	2.717
	12	1.9812	2.5019	51.113	0.828	0.331	3.034
ZrB2-30wt%SiC	6	1.9431	2.5019	54.727	0.876	0.350	3.483
	7	1.9939	2.5019	44.314	0.870	0.348	2.732
	8	2.0066	2.50063	44.758	0.827	0.331	2.624
	9	1.9685	2.5019	50.629	0.765	0.306	2.834
	10	1.9431	2.5146	51.208	0.746	0.297	2.815
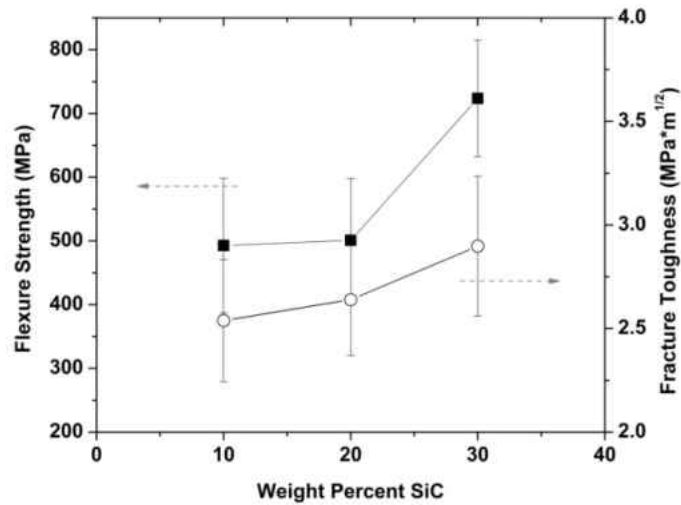
Figure 61: The effect of SiC weight on Flexure Strength and Fracture Toughness

To show what the notches looked like before the fracture toughness test was conducted, pictures are included below as Figure 62 and Figure 63 for ZrB_2-10wt%SiC composition, Figure 64 and Figure 65 for ZrB_2-20wt%SiC composition, and Figure 66 and Figure 67 for ZrB_2-30wt%SiC composition. Each figure has an overall picture of the entire notch and a picture of just the notch tip.
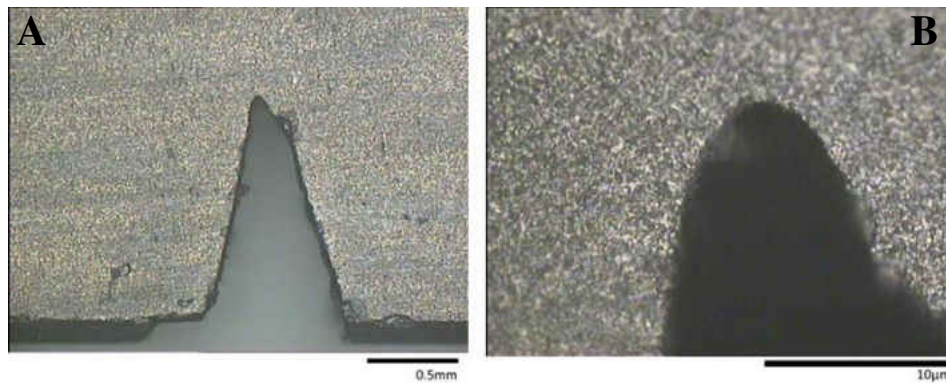
Figure 62:ZrB_2-10wt%SiC Sample 8 Notch depth (a) and Notch tip (b)
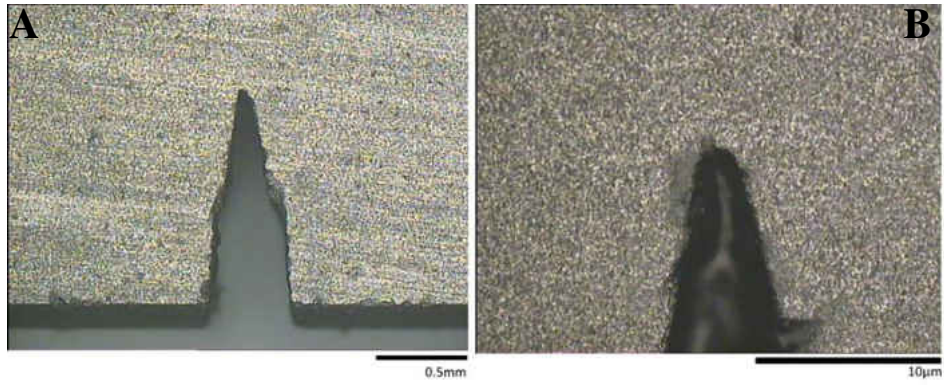
Figure 63: ZrB$_2$-10wt%SiC Sample 14 Notch depth (a) and Notch tip (b)
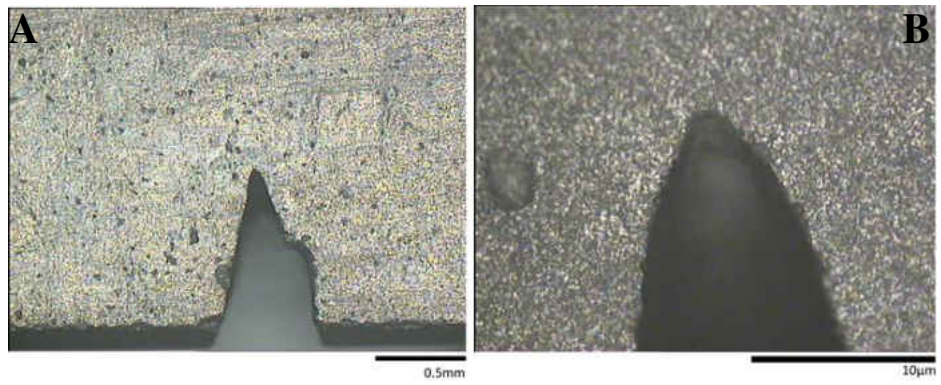
Figure 64: ZrB$_2$-20wt%SiC Sample 7 Notch depth (a) and Notch tip (b)
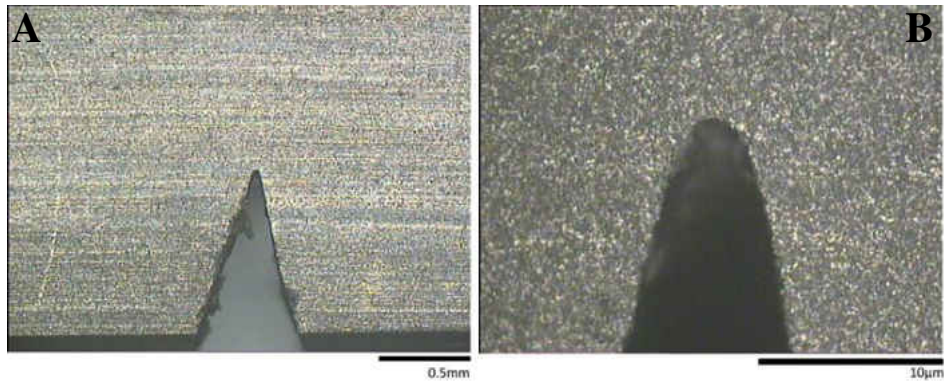
Figure 65: ZrB$_2$-20wt%SiC Sample 9 Notch depth (a) and Notch tip (b)
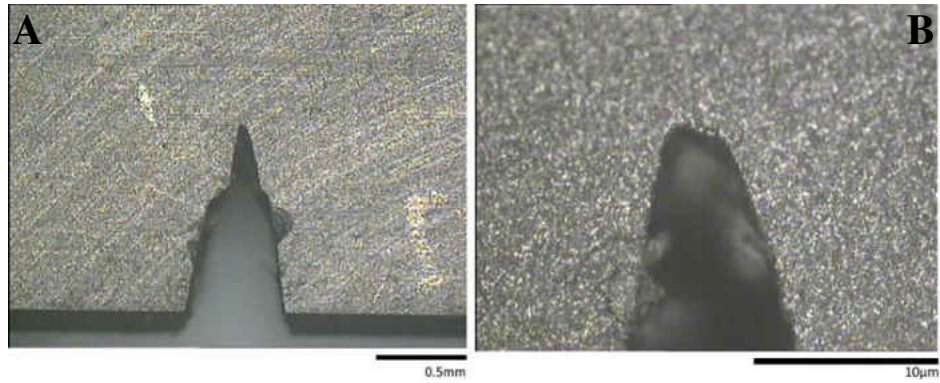
Figure 66: ZrB$_2$-30wt%SiC Sample 7 Notch depth (a) and Notch tip (b)
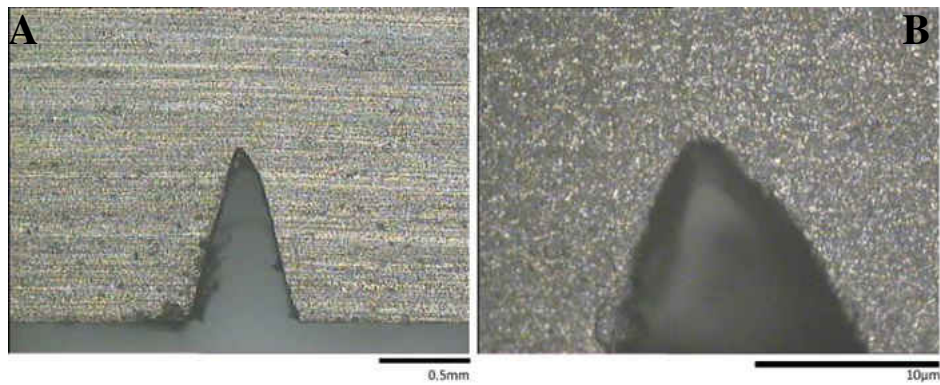
Figure 67: ZrB2-30wt%SiC Sample 9 Notch depth (a) and Notch tip (b)

Below are the SEM pictures of the samples after the fracture toughness test was conducted. Figure 68 shows the SEM Images of ZrB$_2$-10wt%SiC, Figure 69 for ZrB$_2$-20wt%SiC, and Figure 70 for ZrB$_2$-30wt%SiC.
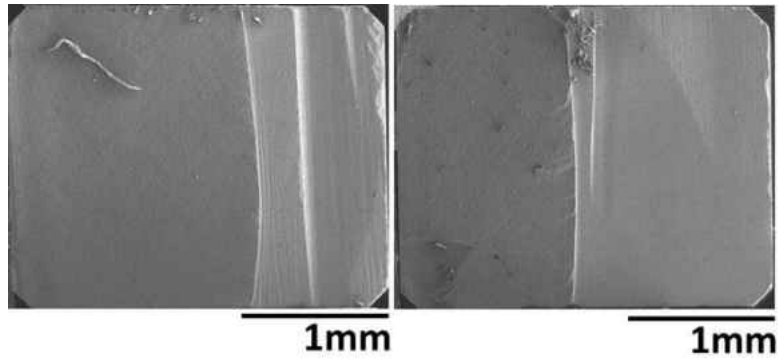
Figure 68: ZrB$_2$-10wt%SiC Fracture surface average (a) and maximum (b)
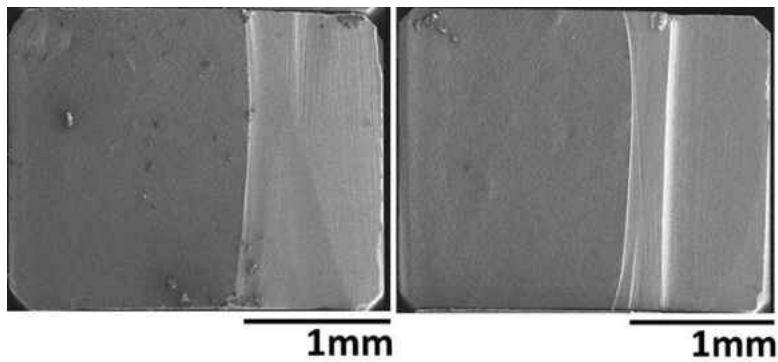
Figure 69: ZrB$_2$-20wt%SiC Fracture surface average (a) and maximum (b)
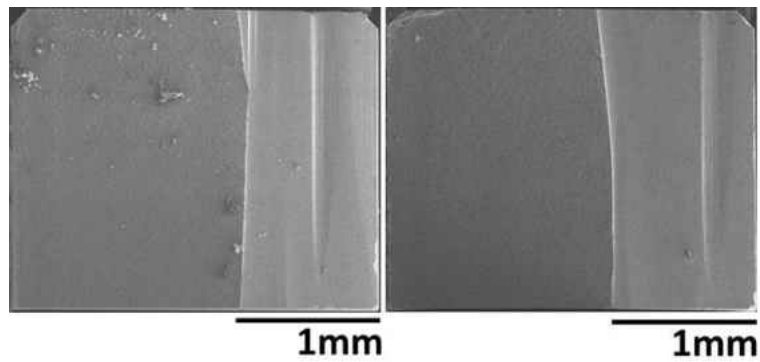
Figure 70: ZrB$_2$-30wt%SiC Fracture surface average (a) and maximum (b)

Since the samples used in these experiments were small, RUS was used in order to find the Young's Modulus, Bulk Modulus, Shear Modulus and Poisson's ratio; which are shown

70

below as Figure 71 and Figure 72. Looking at these two figures on sees that the Young's, bulk, and shear Moduli all decreased with increase in weight percent of SiC. This trend also matches literature shown in the literature part of this thesis. While Poisson's ratio increases with increase in weight percent SiC.
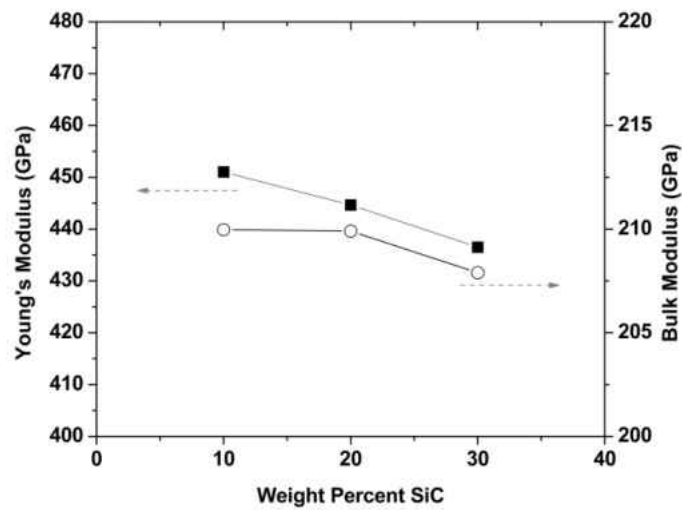
Figure 71: The effect of SiC weight on Young's Modulus and Bulk Modulus
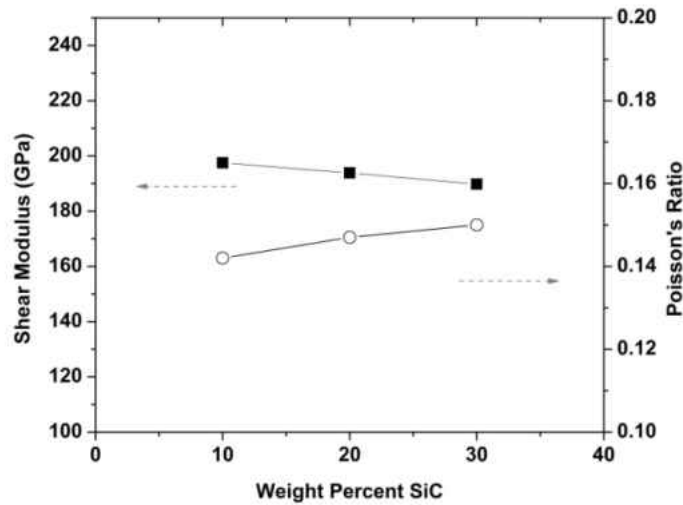
Figure 72: The effect of SiC weight on Shear Modulus and Poisson's Ratio

4.3: Bending Device Calibration

Before the bending device could be used to conduct the experiment, it needed to be calibrated. This was done in the following fashion: since the output of the load cell initially produced a voltage, a correlation from voltage to force was calculated. To do this, weights were applied by screwing off the load cell cap and placing an acrylic platform that provided a flat surface to apply various weights. A series of weights from 10 g to 200 g was placed on the acrylic platform and the corresponding voltage was recorded to verify that the measured voltage is accurate. This calibration is shown below in Figure 73. Based on the measured data, it was established that in order to obtain the force in Newton's, the voltage output of the load cell had to be multiplied by eight.
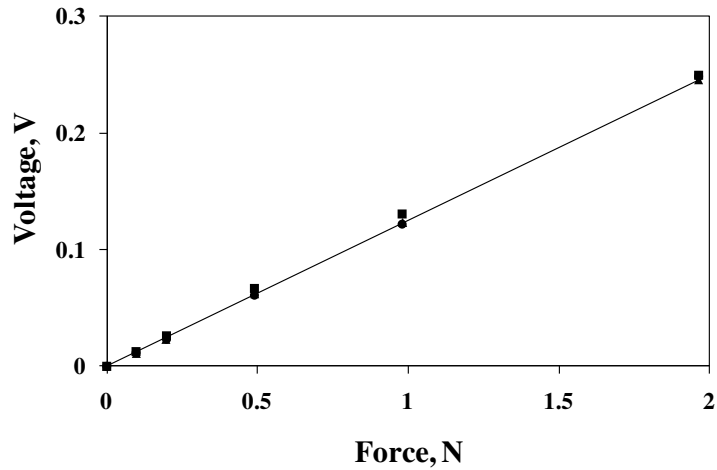
Figure 73: Force applied versus voltage output for calibration of the load cell.

In order to further verify the correctness of the measured stress and strain by the *in-situ* bending device, selected materials with a known Young's modulus were used to perform the bending tests. Stress was applied by the load cell, and resulting strain was measured by an attached strain gauge. The foil strain gauge was mounted with cyanoacrylate adhesive strain gauge glue on the tensile surface of the sample. The wires of the strain gauge and a programmable power supply that outputted 4 V and 0.2 A were attached to an Omega BCM-1 in a quarter bridge configuration. A Flute 114 multimeter was also attached to read the output voltage produced by the strain gauge. This setup is shown below in Figure 74. After the stress-strain data were collected, the slope of the stress-strain curve was determined and the Young's modulus was calculated.
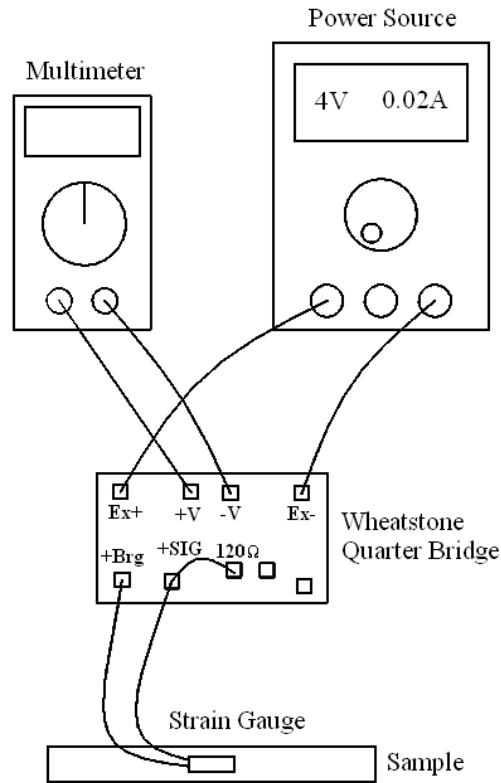
Figure 74: Strain measurement setup for the sample under investigation.

Further, the measured Young's modulus values were compared to those published in the literature or measured by other techniques. Few materials were selected as materials of choice for calibration and verification of *in-situ* bending device. Aluminum 2024 T3 (Al) was chosen as an example of a soft and ductile material, as well as brittle ceramics, such as $La_{0.8}Sr_{0.2}Ga_{0.8}Mg_{0.2}O_3$, $La_{0.8}Ca_{0.2}CoO_3$, and B_4C. The Young's modulus of Al was reported to be 73.1 GPa [84], for $La_{0.8}Sr_{0.2}Ga_{0.8}Mg_{0.2}O_3$ was reported to be 175 GPa [85], for $La_{0.8}Ca_{0.2}CoO_3$ was reported to be 135 GPa [86], and for B_4C it was reported to be 450 GPa [87].

Each sample was loaded and unloaded five times using the *in-situ* bending device so that the stress-strain deformation curves could be collected for these materials for multiple times as shown below in Figure 75.
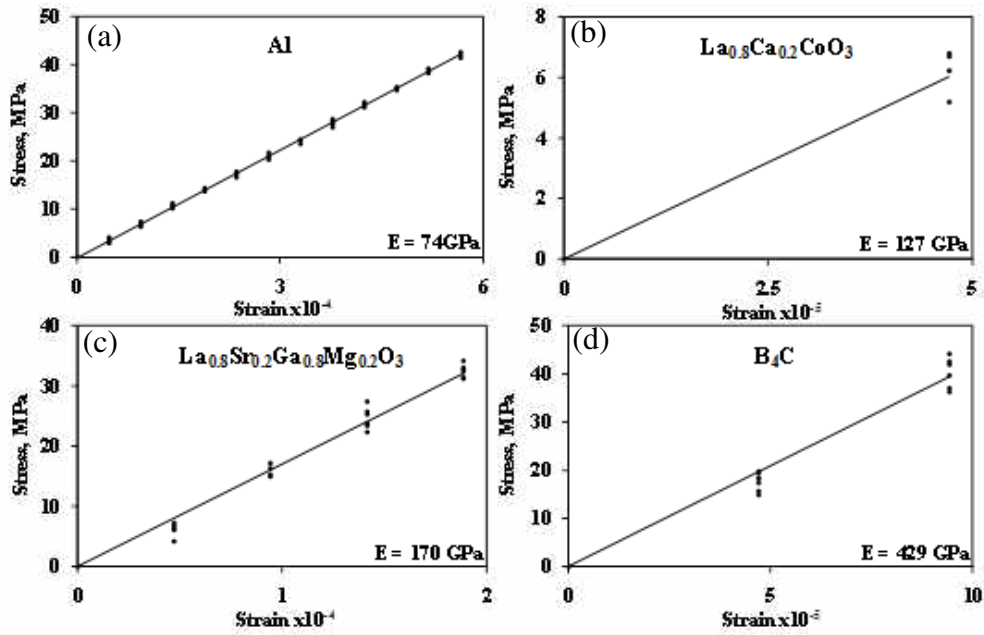
Figure 75: Stress-strain deformation curves obtained by loading (a) Al, (b) La0.8Ca0.2CoO3, (c) La0.8Sr0.2Ga0.8Mg0.2O3, and (d) B4C samples using the in-situ loading device. The Young's moduli of the samples obtained from the measurements showed a good coincide

By comparing the reference data measured in the literature to the experimental data obtained in the present research, one can see that the measured values of Young's Moduli of the four materials deviated by 6% of the data published in the literature. Thus, the calibration results show that the device performs very well and can be reliable for *in-situ* bending under laser radiation.

4.4: Raman Spectroscopy of ZrB$_2$-SiC Samples

Now looking at the Raman Spectra of ZrB$_2$-SiC, one gets the spectrum shown in Figure 76 below. The peaks in this figure are the peaks of 6H-SiC, which have been widely studied in literature as shown in the literature section of this thesis. The peaks shown in Figure 76 are the peaks investigated to find their dependence on stress. Before a stress test can be conducted, one needs to identify all of the peaks present and find out how to obtain an accurate curve fit of the data. The Wire software was use to do the curve fitting of the Raman spectra. The 4-peak position of 6H-SiC that one was interested in is TO peaks 767 cm^{-1}, 789 cm^{-1}, 797 cm^{-1} and LO peak 965 cm^{-1}. Upon curve-fitting this initial spectra, one found that at different locations, the spectra was slightly different, with one or two of the peaks having a change in slope that could indicate another hidden peak. Thus in order to get a better curve fit, one would put in an extra curve on the spectra that had a significant change in slope. Therefore sometimes the spectra would have 4, 5, or 6 curves in the results. Upon looking into literature, one found that the extra curve corresponded to other SiC polytypes of 3C and 4H. This brought about a couple of questions: does our samples contain many polytypes of SiC? Or are these curves just a filler curve to improve the curve fitting? To answer these questions, one suggested either doing XRD or doing a Raman cooling experiment down to liquid nitrogen. The reason for the liquid cooling is that since Raman is a vibrational spectroscopy, when samples are cooled, there are less vibrations; thus the peaks in the spectra will be narrower and therefore one can see exactly how many curves are really present. From this, one can determine if these peaks correspond to different polytypes of SiC. For this thesis, one decided to use only 4-curve so one can be

consistent, since not all spectra have the extra curves. This spectrum was curve fitted by hand and the parameters of this curve fit were saved and used for every spectra in this thesis.
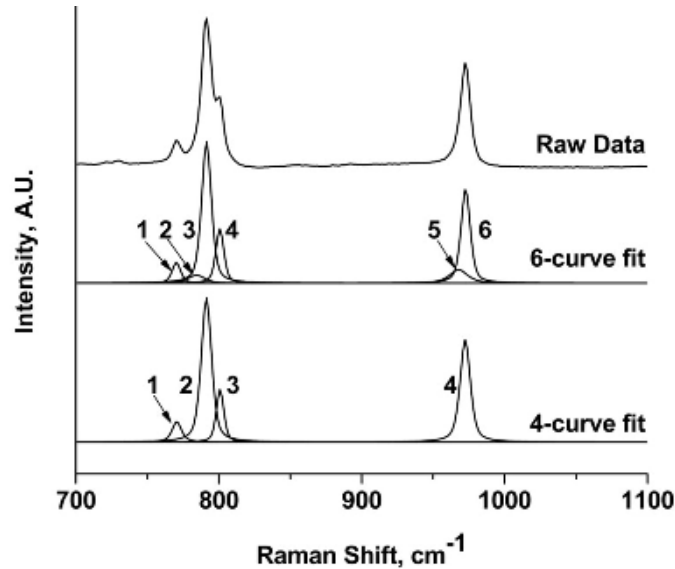
Figure 76: ZrB$_2$-SiC Raman Spectra

The ZrB$_2$ constituent of the composite has not been studied. Only in our preliminary studies had it been indicated that ZrB$_2$ exhibits a very weak Raman activity, shown in Figure 78, and its two Raman active bands could be used to study the vibrational temperature and stress dependent properties of ZrB$_2$. The crystal structure and Brillouin zone of transition metals diborides were described in earlier publications [88-91]. However, the analysis of the ZrB$_2$ phonon dispersion has just appeared in the paper in press [92]. The paper reported on two infrared active modes (E_{1u} at 60.61 meV and A_{2u} at 63.49 meV), as well as two Raman active modes (B_{1g} at 67.76 meV and E_{2g} at 98.45 meV), of calculated Γ point frequencies of ZrB$_2$ compound. It was also reported that the calculated phonon dispersion curves do not contain soft modes at any direction, thus pointing out the stability of the *P6/mmm* ZrB$_2$ phase. The crystal

structure of ZrB_2 is primitively hexagonal [93-96] with the unit cell of ZrB_2 containing three atoms [97], which gave rise to a total of nine phonon branches, consisting of three acoustic modes and six optical modes. The boron atoms lie on the corners with the three nearest neighbor boron atoms in each plane. The Zr(Hf) atoms lie directly in the centers of each boron hexagon, but midway between adjacent boron layers. Each Zr(Hf) atom has 12 nearest neighbor B atoms, and six nearest neighbor in plane Zr(Hf) atoms. The Zr(Hf) atom is positioned at (000); one B atom is at $(\frac{1}{3}\ \frac{1}{6}\ \frac{1}{2})$, and another B atom is at $(\frac{2}{3}\ \frac{1}{3}\ \frac{1}{2})$. The Zr(Hf) layers alternate with the B layers; however, it is not considered a layered compound because of the very strong interaction between interlayers. While main contribution to acoustic phonons results from the transition metal sublattice, the high frequency phonons stem from the boron ions. This is expected since the boron atom is lighter than the transition metal atoms, which leads to comparatively weaker electron-phonon interactions. The covalent character of the B-B bonding is also important for the high frequency of phonons involving boron atoms.

Yet, there is no experimental data published to confirm results of the theoretical calculations of the vibrational properties of ZrB_2 or HfB_2 ceramics. Our preliminary results [98] indicate that ZrB_2 are indeed weakly Raman active with two Raman active bands with the raw data being shown in Figure 77 below. In order to see the two peaks better, one has to subtract the base line, and then change the range to 250-2000 Raman shift, and one will get the graph shown in Figure 78 below. Even though one found ZrB_2 to be weakly Raman active, more in-depth research is required to understand the origin of these peaks and determine their stress/strain/temperature sensitivity.
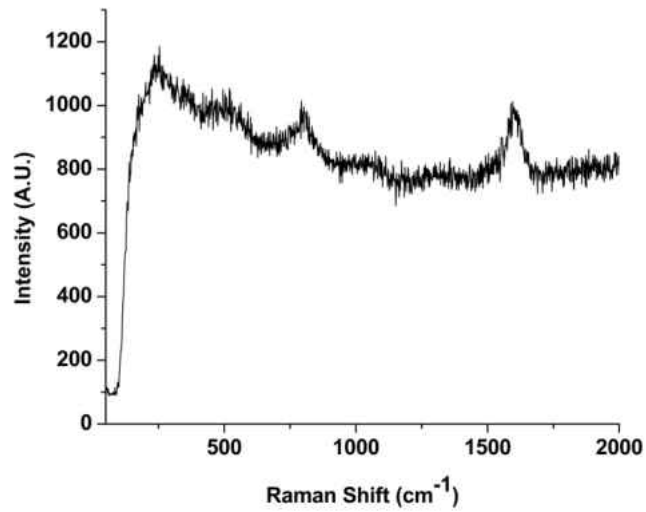
Figure 77: ZrB$_2$ Raw Data
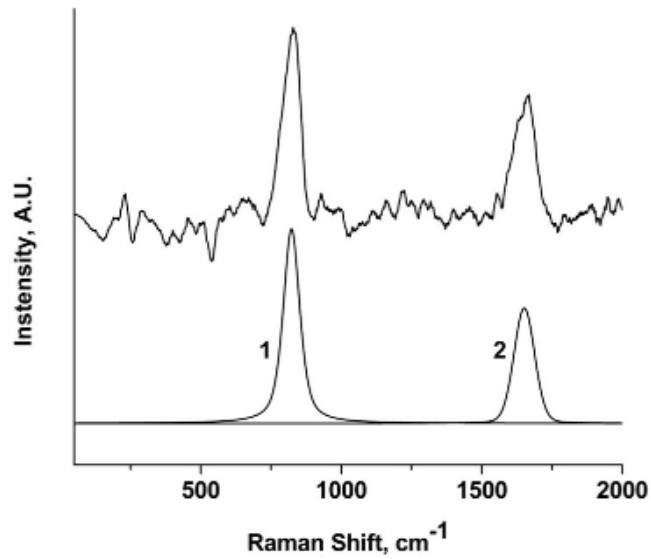
Figure 78: ZrB$_2$ Raman Spectra

After conducting the curve fitting and defining the peaks of interest, Raman Mapping experiment of a sample from each of the composites was conducted. A Raman mapping is made by taking an area of a specimen and then breaking it up into a grid system; each of the grid points

will have a spectra taken. This was done for samples over an area of 20μm x 20μm. Once the mapping is complete, one has to do the analysis and choose what type of map to create. For this thesis, one was interested in the intensity of the highest peak, the TO 790cm^{-1} peak. Thus the entire data collected was curve fitted, and the intensity of the peak was calculated for each point. Then the maps shown in Figure 79 were created. The dark areas represent low intensity and therefore are most likely ZrB_2, while the brighter spots represent high intensity and are SiC grains. Thus one is able to show the distribution of the grains on the sample using Raman Mapping.
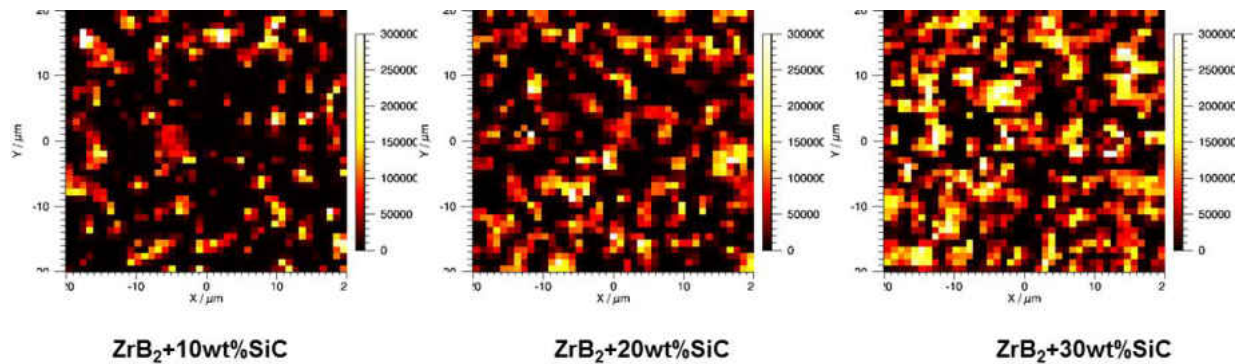
Figure 79: Raman Mapping of ZrB₂-SiC composites based on SiC 790cm^{-1} TO Peak Intensity

4.5: Piezo-Spectroscopy coefficient of ZrB₂-SiC Samples

Thermal or mechanical processing of materials often results in inelastic strains, which generate residual stresses. Such processing or mechanical deformation-induced residual stresses can be categorized as macrostresses and microstresses. Macroscopic surface residual stresses often result either during the cooling of large size components due to poor thermal conductivity, especially in ceramics (resulting from differential thermal contraction between bulk of the

material and surface), or when different macroscopic regions of a component deform non-uniformly but are constrained to fit together (such as the surface and interior). In contrast, residual microstresses can occur at the microstructural level (intergranular or interfacial microstresses) or at the level of the crystal structure (intragranular microstresses) [99]. Such stresses are, by necessity, balanced by opposing stresses in other locations within the material. Depending on the crystal structure and anisotropy, thermally induced residual stress state can be significantly complex, which is even further enhanced in multiphase composites where different phases have different CTEs and elastic moduli. Simple elastic theories may not predict the residual stress state, and residual stress measurements often require a combination of advanced experimental techniques and modeling efforts.

The processing-induced intergranular microstresses develop during the cooling of a multiphase composite whenever materials with different coefficients of thermal expansion (CTE) and elastic moduli are bonded together [100-102], whereas the intragranular residual microstresses result in anisotropic single phase polycrystalline material due to thermal contraction differences between the crystallites [103-105]. Mechanical deformation-induced microstresses develop due to elastic-plastic deformation within the material or due to strain incompatibility within the grains. Development of such microstresses is critically dependent upon the elastic and plastic anisotropy intrinsic to the material because variations in the degree of elasto-plastic anisotropy strongly influence the magnitude of microstress [106]. The inter-/intra-granular microstresses are of critical importance in failure mechanisms of the ceramics, such as ratio of the trans- and inter-granular fracture, crack branching or bridging [107], microcracking [108, 109], stress-induced phase transformation [110, 111], subcritical crack growth [112],

fatigue [113], etc. These microstresses govern crack-propagation induced energy dissipation [114, 115] and affect the ceramic toughness and strength.

The appearance of the residual microstresses in the as-processed Zr(Hf)B$_2$-SiC composite is explained by the mismatch in Young's moduli (E) and CTE (α) between ZrB$_2$ (E=489 GPa, α=5.9×10^{-6}K^{-1}) [42, 48, 116] and 6H-SiC (E=694 GPa, α=3.5×10^{-6}K^{-1}) [117, 118], as well as the difference between room temperature (25°C) and the sintering temperature (typically at ~2100 °C) of the composite. The equiaxed and almost spherical SiC grains can be assumed as elastic spheres of uniform size distributed in an infinite elastic continuum of ZrB$_2$ matrix [119]. This results in an axially symmetric stress distribution around SiC grains. It has been shown that the ceramic grain will be under a uniform/hydrostatic pressure P which can be expressed as shown in the following equation 7 [119]:

$$P = \frac{(\alpha_m - \alpha_p)\Delta T}{\left[\dfrac{0.5(1+v_m)+(1-2v_m)V_p}{E_m(1-V_p)} + \dfrac{1-2v_p}{E_p}\right]} \tag{7}$$

where v is Poisson's ratio, ΔT is temperature change, V_p is volume fraction of grains, and subscripts m and p stand for matrix and grain. On the other hand, radial (σ_{rad}) and tangential (σ_{tan}) stresses within the ZrB$_2$ matrix and at a distance r from the center of grain are expressed, respectively, as equation 8 below [119].

$$\sigma_{rad} = \frac{P}{1-V_p}\left[\frac{a^3}{r^3} - V_p\right] \quad \text{and} \quad \sigma_{tan} = -\frac{P}{1-V_p}\left[\frac{a^3}{2r^3} + V_p\right] \tag{8}$$

Thus, from the above equations it can be seen that when $\alpha_m > \alpha_p$, as is the case for ZrB$_2$-SiC composites, cooling of the composite from the sintering temperature will induce a uniform compressive stress within the SiC grains. The radial and tangential stresses within ZrB$_2$ will be compressive and tensile, respectively, and both the stresses will be at maximum at the ZrB$_2$-SiC interface.

When modeling multiphase particle reinforced composites, residual microstresses in the matrix and inclusions (different phases) can be a-priori estimated based on the simplified composite theory [120-124]. However, experimental determination of these microstresses as a function of microstructural parameters would not only allow the stress state of a particular composite to be better assessed but also design of the composites with specific properties to suit desired/target applications.

In order to find the residual stress, one must first find the non-stressed Raman peak position. These preliminary results are done without using the bending device, but just using unstressed state and finding the peak positions. This is needed in order to correlate the stress state in the ZrB$_2$-SiC ceramic composite stress. This is shown in Figure 80 below for only the TO 796cm^{-1} and LO 960cm^{-1} peaks. This relation was used to find the change in the stress based on the change in Raman shift. Now using equation 7 and 8, one can find the stress state of the SiC in the ZrB$_2$-SiC ceramic composite. The diagram shown in Figure 81a below can be used to define all of the variables and the origin. One gets the following as shown in Figure 81b for the stress distribution starting with the center of a SiC and going out radial until there is no SiC left. The highest stress occurs at the interface of the ZrB$_2$-SiC grains and then decreases from there.
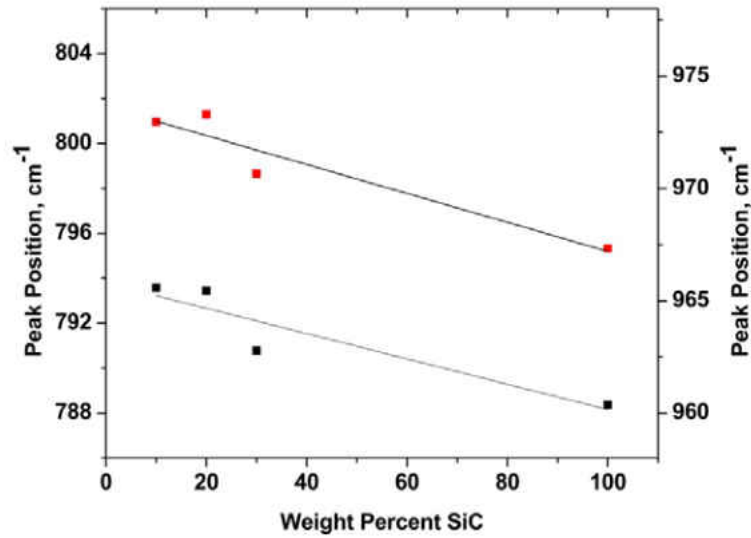
Figure 80: Effect of SiC composition on Raman Peak Position
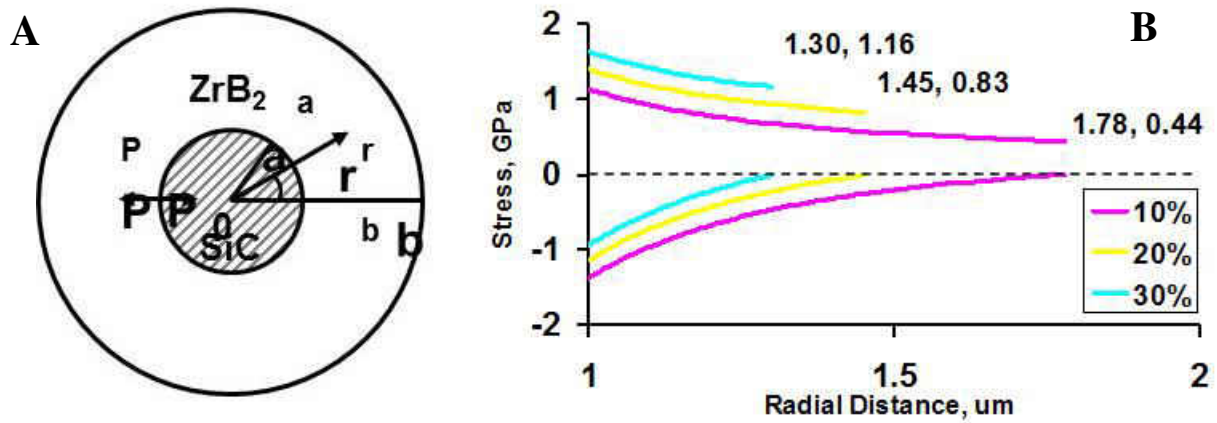
Figure 81: ZrB₂-SiC variable definition (a) and the calculated stress distribution (b)

Once the preliminary data was found, the *in-situ* bending experiment was conducted for ZrB$_2$-20wt%SiC and ZrB$_2$-30wt%SiC. For each composition, multiple samples and multiple locations on each sample were investigated. This was done in order to get some statistical data. Thus one conducted five trails for each of the two compositions. For one of the trials, the interval

of stress was changed to 50MPa from 20MPa. This was done in order to see if there is a significant change in the piezo-spectroscopic coefficient. This was also done to make sure that a 20MPa step size is not too small to get a meaningful change in peak position outside the uncertainty of our system. The uncertainty of the curve fitting process of our Renishaw Micro Raman Spectrometer, and the software is approximately $0.2cm^{-1}$ when obtaining the peaks positions. This may be apparent in some of the trial results. Some have positive correlations, which is the opposite of what the correlations should be. Figure 82 and Figure 83 below show two trails results for ZrB_2-20wt%SiC. Looking at Figure 83, one finds the results of the run with 50MPa step size. Looking at the slopes and comparing that to the first trail, one sees they are on the sample order of magnitude and also one sees that overall change between each point is more defined Thus for future work, one will use a step size of 50MPa to not only increase the accuracy of the curve fit but also to show the change in Raman shift from the previous stress state better. The last reason to use this is that one will be out of the range of uncertainty of the curve fitting for each of the results. Figure 84 below shows one-trail results for ZrB_2-30wt%SiC. Summaries of all piezo-spectroscopy coefficients for each of the runs results are shown in Table 12 below. Looking at this table, one find that the slopes of both compositions are on the same order with ZrB_2-30wt%SiC having a high slope. This makes sense since there is more SiC present in the samples. Comparing the pizeo-spectroscopy calculated in this thesis to one found in literature and they match very well. The values found in literature for 6H-SiC was found , to be in the range of ~0.2-3 GPa cm^{-1} [80]. The average values of the piezo-spectroscopy coefficient for all the runs are shown below as Table 13. The values were averaged for each peak and composition separately to come up with 8 final coefficients along with error.
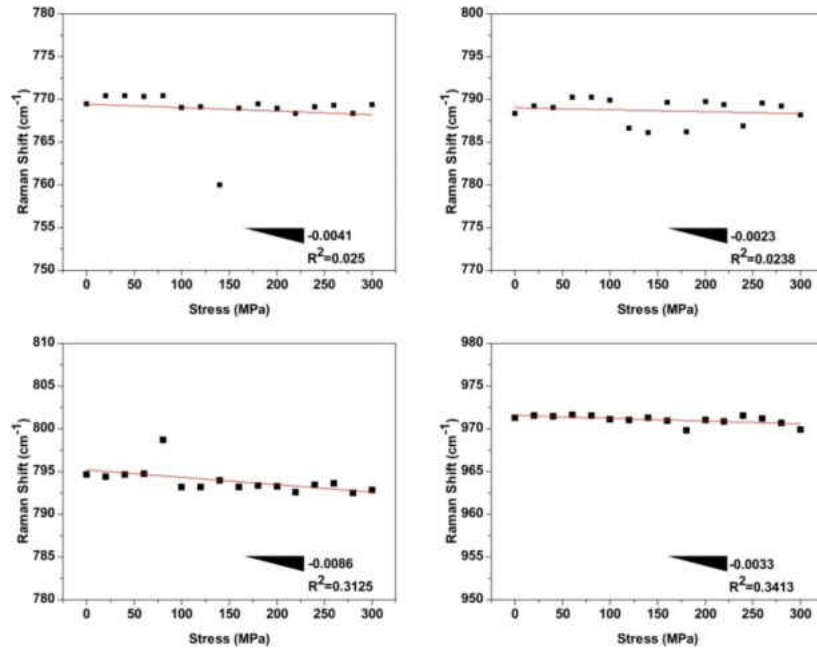
Figure 82: ZrB$_2$-20wt%SiC Result
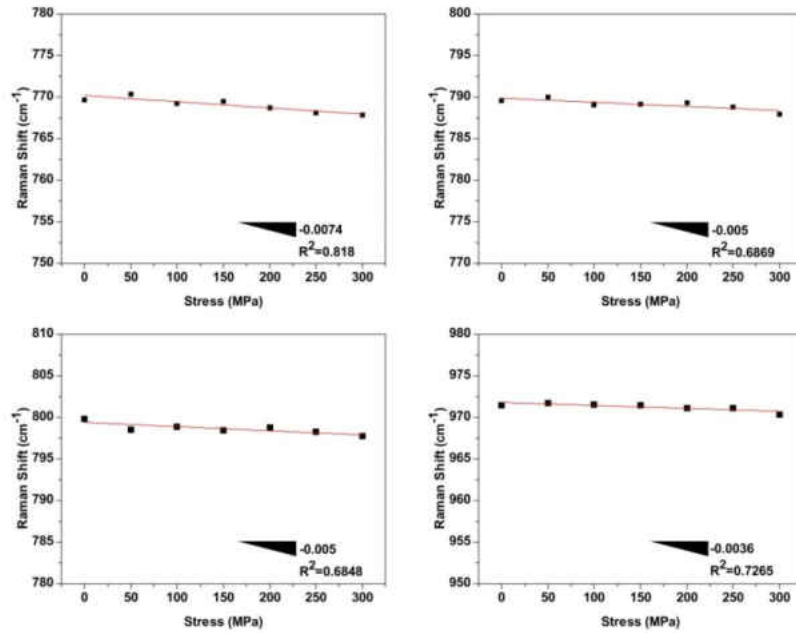
Figure 83: ZrB$_2$-20wt%SiC Result 50MPa Step size
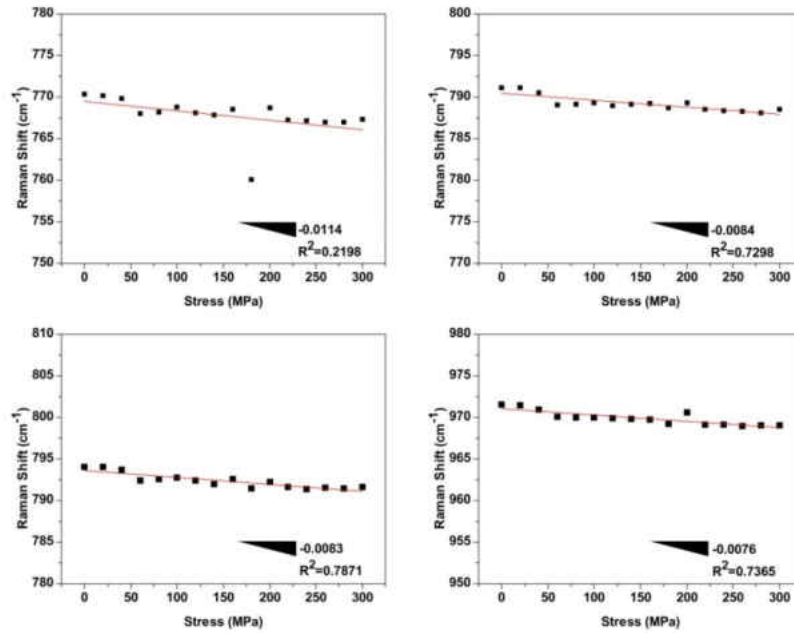
Figure 84: ZrB₂-30wt%SiC Trail 5 Results

Table 12: Summary Calculated Piezo-Spectroscopy Coefficients

		TO Peaks(MPa*cm)			LO Peak(MPa*cm)
Composition	Trial	Peak 1	Peak 2	Peak 3	Peak 4
ZrB2-20wt%SiC	1	0.0058	-0.0005	-0.0011	0.0026
	2	0.0006	0.0014	-0.0007	-0.004
	3	-0.0012	-0.0124	-0.0147	-0.009
	4	-0.041	-0.0023	-0.0086	-0.0033
	5	-0.0074	-0.005	-0.005	-0.0036
ZrB2-30wt%SiC	1	0.0007	-0.0005	0.0015	-0.0006
	2	-0.0041	-0.0041	-0.000002	-0.0012
	3	-0.0053	-0.0042	-0.0048	-0.008
	4	-0.0041	-0.0023	-0.0086	-0.0033
	5	-0.0114	-0.0084	-0.0083	-0.0076

Table 13: Average Piezo-Spectroscopy Coefficients

Pure SiC peak position	ZrB2-20wt%SiC (GPa^{-1}*cm^{-1})	ZrB2-30wt%SiC (GPa^{-1}*cm^{-1})
767cm^{-1}	-3.42±6.912	-4.84±4.331
797cm^{-1}	-3.76±5.375	-3.9±2.937
789cm^{-1}	-6.02±5.821	-4.640±3.888
965cm^{-1}	-3.46±4.116	-4.14±3.491

Since the piezo-spectroscopy coefficients were found, one can now derive an equation for the relationship between the peak shift and the magnitude of the stress. The equation that defines the relationship between the peak shift and the stress is shown below as equation 9 [77].

$$\Delta\omega = k * P \tag{9}$$

where Δω is the Raman peak shift, k is the piezo-spectroscopy coefficient in GPa*cm^{-1} and P is the magnitude of stress in GPa. Now using equation 9, one can derive 8 equations one for each peak position and composition. The 8 equations are shown in below in Table 14.

Table 14: Equations Relating Peak Shift to Stress

Pure SiC peak position	ZrB2-20wt%SiC	ZrB2-30wt%SiC
767cm^{-1}	$\Delta\omega = -3.42 \pm 6.912 * P$	$\Delta\omega = -3.46 \pm 4.116 * P$
797cm^{-1}	$\Delta\omega = -3.76 \pm 5.375 * P$	$\Delta\omega = -3.9 \pm 2.937 * P$
789cm^{-1}	$\Delta\omega = -6.02 \pm 5.821 * P$	$\Delta\omega = -4.64 \pm 3.888 * P$
965cm^{-1}	$\Delta\omega = -3.46 \pm 4.116 * P$	$\Delta\omega = -4.14 \pm 3.491 * P$

Once the equation for the dependence of the peak shift on stress was derived, the stress state could be found based on the change in the Raman peak position. This could not be done for the current work since the peak position must be found with zero stress. The reason that the zero stress peak position could not be found is that the ceramic composites have residual stresses, which results in not getting the correct zero stress peak position. Thus in order to find the zero stress peak position, one needs to find the piezo-spectroscopy coefficient for pure SiC. This composition was present during the current work and will be conducted in the future works. Once the SiC piezo- spectroscopy coefficient is found, one can then finally find the stress based on the Raman peak shift and finally be able to produce stress mappings of ZrB_2-10, 20, and 30wt%SiC ceramic composites.

CHAPTER 5: CONCLUSIONS

ZrB$_2$-10wt%SiC, ZrB$_2$-20wt%SiC and ZrB$_2$-30wt%SiC samples were produced using SPS. Following that, the samples were tested and fully characterized. The samples were characterized by calculating density, flexure strength, fracture toughness, Young's modulus, bulk and sheer moduli. The trends found in this thesis for the increase of weight percent SiC vs. the mechanical properties are found to match well with literature. The mechanical testing was followed by using a SEM to look at the fracture surfaces, to find common defects (which included pores and dislocations), and to find the fracture origin. Following the characterization, Raman spectroscopy was carried out with and without the *in-situ* bending device to find the residual stresses between the ZrB$_2$ phase and the SiC phase. The results obtained for the piezo-spectroscopy in this thesis, for both ZrB$_2$-20wt%SiC and ZrB$_2$-30wt%SiC, fall in the range of 3-6 GPa^{-1}*cm^{-1}; which compares well with previous results of 6H-SiC piezo-spectroscopy found in literature . For the ZrB$_2$-20wt%SiC samples, calculating the piezo-spectroscopy with 20MPa and 50MPa step size, one does not notice a real different between the two. The 50MPa step size shows better linear dependence and will decrease the experimental time to find the piezo-spectroscopy coefficient. Finally, one still needed to find the piezo-spectroscopy coefficient of pure ZrB$_2$, ZrB2-10wt%SiC and pure 6H-SiC. This is already in the works with the samples being produced. I am looking forward to continue this research into my PhD dissertation.

CHAPTER 6: FUTURE WORK

Future work will allow me to continue the current work to further understand this material. By doing the following after residual stresses and magnitudes are determined, both in SiC reinforcing phase and ZrB_2 matrix phase, I will work on determining how the residual stresses affect the mechanical and thermal properties of ZrB_2-SiC composites. The static properties, such as bending and compressive strength, hardness, indentation fracture resistance, coefficient of thermal expansion, and Young's Modulus of the composites will be measured both at room and high temperatures. The time dependent properties such as fatigue and creep will also be measured for ZrB_2 composites with different quantities of the SiC phase. All of the properties will be evaluated as a function of volume fraction of SiC to identify the morphology, residual stress distribution, and volume fraction of the second phase that provides the best mechanical performance. Most important for such characterization is the determination of residual stresses and their redistribution under a variety of loading conditions, as well as the establishment of the stress-induced changes in the micro-structure with variable composition.

I plan on testing the virgin ZrB_2 - 10, 20, 30wt% SiC samples at the polysonic Wind Tunnel, available at the Florida State University in Tallahassee, where the conditions of the tests will resemble the conditions that the materials faces when hypersonic vehicles re-enter the Earth's atmosphere. Figure 85 below shows the polysonic wind tunnel. Contact with the director of this wind tunnel has already been made and they have agreed I would be able to visit and conduct experiments on the wind tunnel once it is operational. Both very high speed and consequent friction upon re-entry bring the surfaces of leading edges and nose cone above 2000 °C for a time frame of 30-60 second. This is where almost no other material can survive the

thermal shock and oxidation, except UHTC composites. Metals, when exposed to such conditions, simply melt. It is important to mention that in addition to very high temperature, the very aggressive species of dissociated oxygen ions attack the surface of leading edges and nose cones of the vehicles. The experiments that closely resemble the re-entry conditions will be performed using the Wind Tunnel facilities in Tallahassee. The samples of ZrB_2 with 10, 20, and 30wt% SiC will be exposed to hypersonic flows using the hypersonic wind tunnel. During the experiments, the samples will be exposed to hypersonic flow with a known fraction of dissociated oxygen and nitrogen fraction in the gas mixture. After exposing the samples to these harsh conditions, the surfaces of the ZrB_2 - SiC composites will be analyzed by SEM to determine the formation of the oxide layers and evaluate the effect produced by the hypersonic wind tunnel experiments.
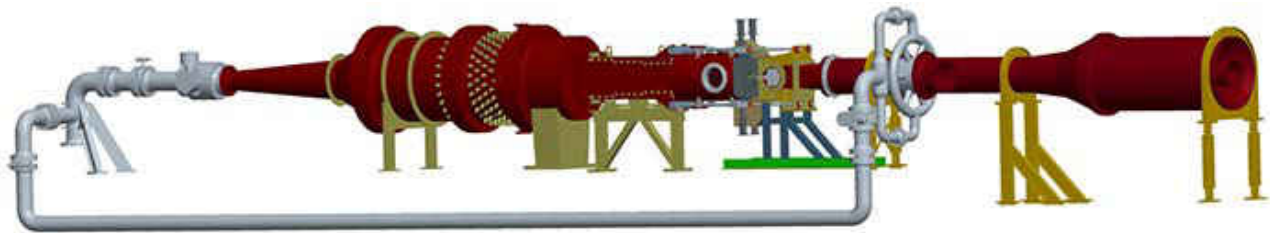
Figure 85: Florida State University polysonic wind tunnel

Following testing the material at Florida State University, I would like to visit NASA Langley Research facility and continue the research using the hypersonic wind tunnel. Since this wind tunnel not only goes to M=7 and another to M=20, which is 1.4-4 times higher than the maximum speed at the Florida State University polysonic wind tunnel, this will replicate the actual speed at which space vehicles re-enter the Earth's atmosphere. This would increase the accuracy of results to be as close to the true flow as possible. In addition, this hypersonic wind

tunnel also offers the heating effects that occur upon re-entry. This wind tunnel is one of a kind and is set apart from the rest of the hypersonic wind tunnels in the fact that it can replicate the flow the most accurately. The reason for this is that most other hypersonic wind tunnels have to cool down helium to a liquid state at high pressures in order to achieve the high Mach number flows in the hypersonic regime, causing the fluid to not be able to replicate the heating encountered during re-entry into the Earth's atmosphere.

Following the hypersonic wind tunnel testing, one would like to conduct an arc jet testing. This experiment is used to replicate the heating upon re-entry. This is also used to investigate the oxidation effects in high heat flux environments. For this experiment, one would like to visit NASA Ames Research facility and work with the thermal protection group on fully testing this material as whole part instead of a layer of protection. Figure 86 below shows an arc jet test in progress.
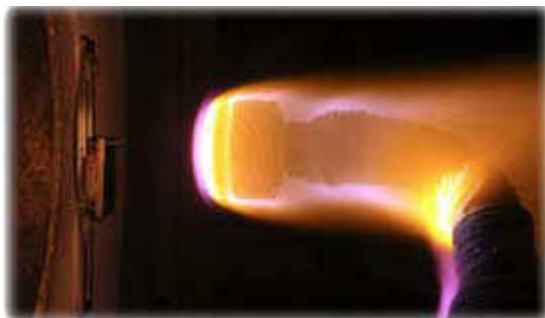
Figure 86: NASA Arc Jet

Following the hypersonic wind tunnel test and the arc jet test, one would like to do some simulations of this material. One will take into account heating, reaction rates, oxidation,

ablation, and the speed of the flow to get the most accurate simulation of the material. This including putting in properties of the material into the simulation to produce the best results.

LIST OF REFERENCES

[1] T. H. Squire and J. Marschall, "Material property requirements for analysis and design of UHTC components in hypersonic applications," *Journal of the European Ceramic Society,* vol. 30, pp. 2239-2251, 2010.

[2] R. Loehman, Corral, E., Dumm, H.P., Kotula, P., Tandon, R., "Ultra-high temperature ceramics for hypersonic vehicle applications," Sandia National Laboratories.

[3] C. A. Steeves, He, M., Valdevit, L., Evans, A.G., , "Metallic structural heat pipes as sharp leading edges from MACH 7 vehicles," in *Proceedings of IMECE 2007, ASME International Mechanical Engineering Congress and Exposition*, Seattle, USA, 2007.

[4] D. D. J. Van Wie DM, King DE and Hudson CM, "The hypersonic environment: Required operating conditions and design challenges," *J. Mater. Sci.,* vol. 39, pp. 5915-5924, 2004.

[5] E. D. a. F. A. Jackson TA, "High speed propulsion: Performance advantage of advanced materials," *J. Mater. Sci.,* vol. 39, pp. 5905-5913, 2004.

[6] M. M. Opeka, I. G. Talmy, and J. A. Zaykoski, "Oxidation-based materials selection for 2000°C + hypersonic aerosurfaces: Theoretical considerations and historical experience," *Journal of Materials Science,* vol. 39, pp. 5887-5904, 2004.

[7] Y. Tsujikawa, Y. Tsukamoto, and S. Fujii, "Performance analysis of scramjet engine with quasi-one-dimensional flow model," *International Journal of Hydrogen Energy,* vol. 16, pp. 135-142, 1991.

[8] A. S. Brown. (1997) Hypersonic designs with a SHARP edge. *Aerospace America.* 20-21.

[9] R. A. Cutler, *Engineering Properties of Borides, pp.787-803 in Ceramics and Glasses: Engineering Materials Handbook, Vol. 4*. Materials Park, OH: ASM International, 1991.

[10] E. Opila, Levine, S., Lorinca, "Oxidation of ZrB2- and HfB2-based ultra-high temperature ceramics: Effect of Ta additions," *J. Mat. Sci.,* vol. 39, pp. 5969-5977, 2004.

[11] A. Rezaie, Fahrenholtz, W., Hilmas, G.E., "Evolution of structure during the oxidation of zirconium diboride-silicon carbide in air up to 1500°C," *J. Europ. Ceram. Soc.,* vol. 27, pp. 2495-2501, 2007.

[12] H. Wen-Bo, H. Ping, Z. Xing-Hong, H. Jie-Cai, and M. Song-He, "High-Temperature Oxidation at 1900°C of ZrB2– xSiC Ultrahigh-Temperature Ceramic Composites," *Journal of the American Ceramic Society,* vol. 91, pp. 3328-3334, 2008.

[13] W. H. Mason, "Some Hypersonic Aerodynamics," *Configuration Aerodynamics Class-Presentation*.

[14] H. Li, L. Zhang, Q. Zeng, J. Wang, L. Cheng, H. Ren*, et al.*, "Crystal structure and elastic properties of ZrB compared with ZrB2: A first-principles study," *Computational Materials Science,* vol. 49, pp. 814-819, 2010.

[15] J. W. Lawson, C. W. Bauschlicher, M. S. Daw, and W. Y. Ching, "Ab Initio Computations of Electronic, Mechanical, and Thermal Properties of ZrB2 and HfB2," *Journal of the American Ceramic Society,* vol. 94, pp. 3494-3499, 2011.

[16] S. N. a. H. Harima, "Raman Investigation of SiC Polytypes," *phys. stat. sol.,* vol. 162, 1997.

[17] P. Greulich-Weber. (2010). *Silicon Carbide: Basics*.

[18] O. M. M. Gadzyra. *Structural Model: Solid solution SiC-C (diamond).*

[19] C. H. Park, B.-H. Cheong, K.-H. Lee, and K. J. Chang, "Structural and electronic properties of cubic, 2H, 4H, and 6H SiC," *Physical Review B,* vol. 49, pp. 4485-4493, 1994.

[20] K. J. Chang and M. L. Cohen, "Ab initio pseudopotential study of structural and high-pressure properties of SiC," *Physical Review B,* vol. 35, pp. 8196-8201, 05/15/ 1987.

[21] P. E. Van Camp, V. E. Van Doren, and J. T. Devreese, "First-principles calculation of the pressure coefficient of the indirect band gap and of the charge density of C and Si," *Physical Review B,* vol. 34, pp. 1314-1316, 07/15/ 1986.

[22] B. H. Cheong, K. J. Chang, and M. L. Cohen, "Pressure dependences of band gaps and optical-phonon frequency in cubic SiC," *Physical Review B,* vol. 44, pp. 1053-1056, 07/15/ 1991.

[23] N. Churcher, K. Kunc, and V. Heine, "Calculated ground-state properties of silicon carbide," *Journal of Physics C: Solid State Physics,* vol. 19, p. 4413, 1986.

[24] N. Churcher, K. Kunc, and V. Heine, "Ground state properties of the group IV ionic compound silicon carbide," *Solid State Communications,* vol. 56, pp. 177-180, 10// 1985.

[25] P. J. H. Denteneer and W. van Haeringen, "Ground-state properties of polytypes of silicon carbide," *Physical Review B,* vol. 33, pp. 2831-2834, 02/15/ 1986.

[26] P. J. H. Denteneer and W. van Haeringen, "Ground-state properties of wurtzite silicon carbide," *Solid State Communications,* vol. 65, pp. 115-119, 1// 1988.

[27] R. D. Carnahan, "Elastic Properties of Silicon Carbide," *Journal of the American Ceramic Society,* vol. 51, pp. 223-224, 1968.

[28] E. V. Clougherty, Kaufman, L., "Investigation of Boride Compounds for Very High Temperature Applications," ManLabs, Inc., Cambridge, MA,1963.

[29] A. E. McHale, *Phase Equilibrium Diagrams – Phase Diagrams for Ceramists* vol. X: The American Ceramic Society, 1994.

[30] L. Zou, N. Wali, J.-M. Yang, and N. P. Bansal, "Microstructural development of a Cf/ZrC composite manufactured by reactive melt infiltration," *Journal of the European Ceramic Society,* vol. 30, pp. 1527-1535, 2010.

[31] G. Honstein, C. Chatillon, and F. Baillet, "Thermodynamic approach to the vaporization and growth phenomena of SiC ceramics. I. SiC and SiC–SiO2 mixtures under neutral conditions," *Journal of the European Ceramic Society,* vol. 32, pp. 1117-1135, 2012.

[32] Q. Lonné, N. Glandut, and P. Lefort, "Surface densification of porous ZrB2–39mol.% SiC ceramic composites by a laser process," *Journal of the European Ceramic Society,* vol. 32, pp. 955-963, 2012.

[33] C.-N. Sun, M. C. Gupta, and K. M. B. Taminger, "Electron Beam Sintering of Zirconium Diboride," *Journal of the American Ceramic Society,* vol. 93, pp. 2484-2486, 2010.

[34] S. Ran, O. Van der Biest, and J. Vleugels, "ZrB2–SiC composites prepared by reactive pulsed electric current sintering," *Journal of the European Ceramic Society,* vol. 30, pp. 2633-2642, 9// 2010.

[35] Z. Yuan, Z. Jin, R. Kang, and Q. Wen, "Tribochemical polishing CVD diamond film with FeNiCr alloy polishing plate prepared by MA-HPS technique," *Diamond and Related Materials,* vol. 21, pp. 50-57, 1// 2012.

[36]   X. Dong, F. Lü, L. Yang, Y. Zhang, and X. Wang, "Influence of spark plasma sintering temperature on electrochemical performance of La0.80Mg0.20Ni3.75 alloy," *Materials Chemistry and Physics,* vol. 112, pp. 596-602, 12/1/ 2008.

[37]   Y. Zhao, L.-J. Wang, G.-J. Zhang, W. Jiang, and L.-D. Chen, "Effect of holding time and pressure on properties of ZrB2–SiC composite fabricated by the spark plasma sintering reactive synthesis method," *International Journal of Refractory Metals and Hard Materials,* vol. 27, pp. 177-180, 1// 2009.

[38]   W.-M. Guo, J. Vleugels, G.-J. Zhang, P.-L. Wang, and O. Van der Biest, "Effect of heating rate on densification, microstructure and strength of spark plasma sintered ZrB2-based ceramics," *Scripta Materialia,* vol. 62, pp. 802-805, 5// 2010.

[39]   I. Akin, M. Hotta, F. C. Sahin, O. Yucel, G. Goller, and T. Goto, "Microstructure and densification of ZrB2-SiC composites prepared by spark plasma sintering," *Mikrostruktur und Verdichtung von mit Funkenentladungsplasmasintern aufbereiteten ZrB2-SiC-Verbundwerkstoffen,* p. 2379, 2010.

[40]   S. C. Zhang, G. E. Hilmas, and W. G. Fahrenholtz, "Mechanical properties of sintered ZrB2–SiC ceramics," *Journal of the European Ceramic Society,* vol. 31, pp. 893-901, 5// 2011.

[41]   W. G. Fahrenholtz, G. E. Hilmas, I. G. Talmy, and J. A. Zaykoski, "Refractory Diborides of Zirconium and Hafnium," *Journal of the American Ceramic Society,* vol. 90, pp. 1347-1364, 2007.

[42]   D. E. Wiley, W. R. Manning, and J. O. Hunter, "Elastic properties of polycrystalline TiB2, ZrB2 and HfB2 from room temperature to 1300 °K," *Journal of The Less-Common Metals,* vol. 18, pp. 149-157.

[43]   H. C. Starck, "ZrB$_2$ Grade B."

[44]   W. G. Fahrenholtz, G. E. Hilmas, A. L. Chamberlain, and J. W. Zimmermann, "Processing and characterization of ZrB2-based ultra-high temperature monolithic and fibrous monolithic ceramics," *Journal of Materials Science,* vol. 39, pp. 5951-5957, 2004.

[45]   X. Zhang, L. Xu, S. Du, C. Liu, J. Han, and W. Han, "Spark plasma sintering and hot pressing of ZrB2–SiCW ultra-high temperature ceramics," *Journal of Alloys and Compounds,* vol. 466, pp. 241-245, 10/20/ 2008.

[46]   Y.-Y. Wang, K. Liu, C.-L. Zhou, C.-H. Wang, R.-x. Liu, and Y.-N. Luan, "Electrical and Mechanical Properties of ZrB2-Based Composite Ceramic," ed: Trans Tech Publications, Zürich, 2012, 2012, p. 744.

[47]   M. M. Opeka, E. J. Talmy, E. J. Wuchina, J. A. Zaykoski, and S. J. Causey, "Mechanical, thermal, and oxidation properties of refractory hafnium and zirconium compounds," *Mechanische, thermische und Oxidations-Eigenschaften von feuerfesten Hafnium- und Zirkonverbindungen,* p. 2405, 1999.

[48]   P. Vajeeston, P. Ravindran, C. Ravi, and R. Asokamani, *Electronic structure, bonding, and ground-state properties of AlB2-type transition-metal diborides*.

[49]   S. Hayun, V. Paris, R. Mitrani, S. Kalabukhov, M. P. Dariel, E. Zaretsky*, et al.*, "Microstructure and mechanical properties of silicon carbide processed by Spark Plasma Sintering (SPS)," *Ceramics International,* vol. 38, pp. 6335-6340, // 2012.

[50] L. Yin, E. Y. J. Vancoille, K. Ramesh, and H. Huang, "Surface characterization of 6H-SiC (0001) substrates in indentation and abrasive machining," *International Journal of Machine Tools and Manufacture,* p. 607, 2004.

[51] H. C. Starck, "Alpha SiC Grade UF-10."

[52] G. A. Slack, "Thermal conductivity of pure and impure silicon, silicon carbide, and diamond," *Journal of Applied Physics,* vol. 35, pp. 3460-3466, 12/02/ 1964.

[53] Z. Li and R. C. Bradt, "Thermal expansion and thermal expansion anisotropy of SiC polytypes," *Waermedehnung und Anisotropie der Waermedehnung von SiC Polytypen,* p. 445, 1988.

[54] J. Watts, G. Hilmas, and W. G. Fahrenholtz, "Mechanical Characterization of ZrB2–SiC Composites with Varying SiC Particle Sizes," *Journal of the American Ceramic Society,* vol. 94, pp. 4410-4418, 2011.

[55] S. Zhu, W. G. Fahrenholtz, and G. E. Hilmas, "Influence of silicon carbide particle size on the microstructure and mechanical properties of zirconium diboride–silicon carbide ceramics," *Journal of the European Ceramic Society,* vol. 27, pp. 2077-2083, // 2007.

[56] A. Rezaie, W. G. Fahrenholtz, and G. E. Hilmas, "Effect of hot pressing time and temperature on the microstructure and mechanical properties of ZrB2–SiC," *Journal of Materials Science,* vol. 42, pp. 2735-2744, 2007/04/01 2007.

[57] P. Hu and Z. Wang, "Flexural strength and fracture behavior of ZrB2–SiC ultra-high temperature ceramic composites at 1800°C," *Journal of the European Ceramic Society,* vol. 30, pp. 1021-1026, 3// 2010.

[58] W. H. Rhodes, E. V. Clougherty, and D. Kalish, "Research and development of refractory oxidation-resistant diborides. Part II. Volume IV. Mechanical properties. Technical report, 15 September 1967--15 May 1969," AD--865809; AFML-TR--68-190(Pt.2)(Vol.4) United StatesThu Dec 13 09:33:35 EST 2012NTIS.ANL; NSA-27-022824English, 1970.

[59] E. W. Neuman, G. E. Hilmas, and W. G. Fahrenholtz, "Strength of Zirconium Diboride to 2300°C," *Journal of the American Ceramic Society,* vol. 96, pp. 47-50, 2013.

[60] M. W. Bird, R. P. Aune, A. F. Thomas, P. F. Becher, and K. W. White, "Temperature-dependent mechanical and long crack behavior of zirconium diboride–silicon carbide composite," *Journal of the European Ceramic Society,* vol. 32, pp. 3453-3462, 9// 2012.

[61] J. W. Zimmermann, G. E. Hilmas, and W. G. Fahrenholtz, "Thermal Shock Resistance and Fracture Behavior of ZrB2–Based Fibrous Monolith Ceramics," *Journal of the American Ceramic Society,* vol. 92, pp. 161-166, 2009.

[62] S. Meng, F. Qi, H. Chen, Z. Wang, and G. Bai, "The repeated thermal shock behaviors of a ZrB2–SiC composite heated by electric resistance method," *International Journal of Refractory Metals and Hard Materials,* vol. 29, pp. 44-48, 1// 2011.

[63] J. K. Kurihara, T. Tomimatsu, Y. F. Liu, S. Q. Guo, and Y. Kagawa, "Mode I fracture toughness of SiC particle-dispersed ZrB2 matrix composite measured using DCDC specimen," *Ceramics International,* vol. 36, pp. 381-384, 1// 2010.

[64] N. Orlovskaya, R. Stadelmann, M. Lugovy, V. Subbotin, G. Subhash, M. Neubert, *et al.,* "Mechanical properties of ZrB2-SiC ceramic composites: room temperature instantaneous behaviour," *Advances in Applied Ceramics,* vol. 112, pp. 9-16, // 2013.

[65]   M. Mallik, K. K. Ray, and R. Mitra, "Oxidation behavior of hot pressed ZrB2–SiC and HfB2–SiC composites," *Journal of the European Ceramic Society,* vol. 31, pp. 199-215, 1// 2011.

[66]   C. Tian, D. Gao, Y. Zhang, C. Xu, Y. Song, and X. Shi, "Oxidation behaviour of zirconium diboride–silicon carbide ceramic composites under low oxygen partial pressure," *Corrosion Science,* vol. 53, pp. 3742-3746, 11// 2011.

[67]   P. Hu, W. Guolin, and Z. Wang, "Oxidation mechanism and resistance of ZrB2–SiC composites," *Corrosion Science,* vol. 51, pp. 2724-2732, 11// 2009.

[68]   W.-M. Guo and G.-J. Zhang, "Oxidation resistance and strength retention of ZrB2–SiC ceramics," *Journal of the European Ceramic Society,* vol. 30, pp. 2387-2395, 8// 2010.

[69]   J. Han, P. Hu, X. Zhang, S. Meng, and W. Han, "Oxidation-resistant ZrB2–SiC composites at 2200°C," *Composites Science and Technology,* vol. 68, pp. 799-806, 2008.

[70]   F. Monteverde, R. Savino, M. D. S. Fumo, and A. Di Maso, "Plasma wind tunnel testing of ultra-high temperature ZrB2–SiC composites under hypersonic re-entry conditions," *Journal of the European Ceramic Society,* vol. 30, pp. 2313-2321, 8// 2010.

[71]   X. Zhang, P. Hu, J. Han, and S. Meng, "Ablation behavior of ZrB2–SiC ultra high temperature ceramics under simulated atmospheric re-entry conditions," *Composites Science and Technology,* vol. 68, pp. 1718-1726, 6// 2008.

[72]   H. Li, L. Zhang, L. Cheng, and Y. Wang, "Ablation Resistance of Different Coating Structures for C/ZrB2–SiC Composites Under Oxyacetylene Torch Flame," *International Journal of Applied Ceramic Technology,* vol. 6, pp. 145-150, 2009.

[73]   S. Tang, J. Deng, S. Wang, and W. Liu, "Comparison of thermal and ablation behaviors of C/SiC composites and C/ZrB2–SiC composites," *Corrosion Science,* vol. 51, pp. 54-61, 1// 2009.

[74]   R. Savino, M. De Stefano Fumo, D. Paterna, and M. Serpico, "Aerothermodynamic study of UHTC-based thermal protection systems," *Aerospace Science and Technology,* vol. 9, pp. 151-160, 3// 2005.

[75]   T. A. Parthasarathy, M. D. Petry, G. Jefferson, M. K. Cinibulk, T. Mathur, and M. R. Gruber, "Development of a Test to Evaluate Aerothermal Response of Materials to Hypersonic Flow Using a Scramjet Wind Tunnel," *International Journal of Applied Ceramic Technology,* vol. 8, pp. 832-847, 2011.

[76]   S. Nakashima and H. Harima, "Raman Investigation of SiC Polytypes," *physica status solidi (a),* vol. 162, pp. 39-64, 1997.

[77]   J. Watts, G. Hilmas, W. G. Fahrenholtz, D. Brown, and B. Clausen, "Stress measurements in ZrB2–SiC composites using Raman spectroscopy and neutron diffraction," *Journal of the European Ceramic Society,* vol. 30, pp. 2165-2171, 8// 2010.

[78]   A. M. Limarga and D. R. Clarke, "Piezo-Spectroscopic Coefficients of Tetragonal-Prime Yttria-Stabilized Zirconia," *Journal of the American Ceramic Society,* vol. 90, pp. 1272-1275, 2007.

[79]   J. F. DiGregorio and T. E. Furtak, "Analysis of Residual Stress in 6H-SiC Particles within Al2O3/SiC Composites through Raman Spectroscopy," *Journal of the American Ceramic Society,* vol. 75, pp. 1854-1857, 1992.

[80]   K. Grodecki, A. Wysmolek, R. Stepniewski, J. M. Baranowski, W. Hofman, E. Tymicki*, et al.*, "Raman Piezospectroscopy of Phonons in Bulk 6H-SiC," *ACTA PHYSICA POLONICA A,* vol. 116, pp. 947-949, 2009.

[81]   M. W. Barsoum, M. Radovic, A. Ganguly, T. Zhen, P. Finkel, S. R. Kalidindi*, et al.*, "On the elastic properties and mechanical damping of Ti(3)SiC(2), Ti(3)GeC(2), Ti(3)Si(0.5)Al(0.5)C(2) and Ti(2)AlC in the 300-1573 K temperature range," *Acta Materialia,* vol. 54, pp. 2757-2767, Jun 2006.

[82]   A. Migliori and J. L. Sarrao, *Resonant ultrasound spectroscopy: applications to physics, materials measurements, and nondestructive evaluation*: John Wiley, 1997.

[83]   M. Radovic, E. Lara-Curzio, and L. Riester, "Comparison of different experimental techniques for determination of elastic properties of solids," *Materials Science and Engineering A,* vol. 368, pp. 56-70, 2004.

[84]   M. Shafiul Ferdous, C. Makabe, M. S. Rana, and T. Miyazaki, "Improving the fatigue strength of a multiple hole specimen by applying additional holes or notches," *Engineering Failure Analysis,* vol. 18, pp. 75-87, 1// 2011.

[85]   S. Pathak, D. Steinmetz, J. Kuebler, E. Andrew Payzant, and N. Orlovskaya, "Mechanical behavior of La0.8Sr0.2Ga0.8Mg0.2O3 perovskites," *Ceramics International,* vol. 35, pp. 1235-1241, 4// 2009.

[86]   N. Orlovskaya, M. Lugovy, S. Pathak, D. Steinmetz, J. Lloyd, L. Fegely*, et al.*, "Thermal and mechanical properties of LaCoO3 and La0.8Ca0.2CoO3 perovskites," *Journal of Power Sources,* vol. 182, pp. 230-239, 7/15/ 2008.

[87]   N. Orlovskaya, S. Yarmolenko, J. Sankar, J. Kuebler, and M. Lugovy, "Effects of rolling and hot pressing on mechanical properties of boron carbide-based ceramics," *Journal of Materials Science,* vol. 43, pp. 5942-5947, 2008/09/01 2008.

[88]   M. C. Cadeville, Meyer, A.J.P., Hebd, C.R., *Seances Acad. Sci.,* vol. 255, 1962.

[89]   S. H. Liu, L. Kopp, W. B. England, and H. W. Myron, "Energy bands, electronic properties, and magnetic ordering of CrB_{2}," *Physical Review B,* vol. 11, pp. 3463-3468, 05/01/ 1975.

[90]   H. Ihara, M. Hirabayashi, and H. Nakagawa, "Band structure and x-ray photoelectron spectrum of ZrB_{2}," *Physical Review B,* vol. 16, pp. 726-730, 07/15/ 1977.

[91]   P. G. Perkins, Sweeney, A.V.J., "Investigation of electronic band structures of NaB6, KB6, TiB2, and CrB," *J. Less-Common Met.,* vol. 47, pp. 165-173, 1976.

[92]   E. Deligoz, K. Colakoglu, and Y. O. Ciftci, "Phonon dispersion and thermodynamical properties in ZrB2, NbB2, and MoB2," *Solid State Communications,* vol. 150, pp. 405-410, 3// 2010.

[93]   G. V. Samsonov, Serebryakova, T.I., Neronov, V.A., *Borides*. Atomizdat, Moscow, 1975.

[94]   I. R. Shein and A. L. Ivanovskii, "Band structure of ZrB2, VB2, NbB2, and TaB2 hexagonal diborides: Comparison with superconducting MgB2," *Physics of the Solid State,* vol. 44, pp. 1833-1839, 2002/10/01 2002.

[95]   K. E. Spear, "Chemical bonding in AlB2-type borides," *Journal of the Less Common Metals,* vol. 47, pp. 195-201, 6// 1976.

[96]   G. Grimvall and A. F. Guillermet, "Phase stability properties of transition metal diborides," *AIP Conference Proceedings,* vol. 231, pp. 423-430, 07/01/ 1991.

[97]   V. A. Epelbaum, Gurevich, M.A., "On Zr-B phase diagram: Formation of ZrB2 phase," *Zh. Fiz. Khim.,* vol. 32, 1958.

[98]   M. Donohue, C. Carpenter, and N. Orlovskaya, "Vibrational Properties of Zr(Hf)B2–SiC UHTC Composites by Micro-Raman Spectroscopy," in *Boron Rich Solids*, N. Orlovskaya and M. Lugovy, Eds., ed: Springer Netherlands, 2011, pp. 287-302.

[99]   D. Dye, H. J. Stone, and R. C. Reed, "Intergranular and interphase microstresses," *Current Opinion in Solid State and Materials Science,* vol. 5, pp. 31-37, 1// 2001.

[100]   R. W. Davidge and T. J. Green, "The strength of two-phase ceramic/glass materials," *Journal of Materials Science,* vol. 3, pp. 629-634, 1968/11/01 1968.

[101]   J. Selsing, "Internal Stresses in Ceramics," *Journal of the American Ceramic Society,* vol. 44, pp. 419-419, 1961.

[102]   W. D. Kingery, "Note on Thermal Expansion and Microstresses in Two-Phase Compositions," *Journal of the American Ceramic Society,* vol. 40, pp. 351-352, 1957.

[103]   O. N. Grigoriev, Krell, A., Trefilov, V.I., "Determination of thermal residual stresses in single phase ceramic materials," *Zavodskaya Laboratoriya,* vol. 7, pp. 36-39, 1990.

[104]   A. Krell, Grigoriev, O.N., "Residual stresses and microporosity in oxide ceramics," *Sprechsaal,* vol. 123, pp. 1012-1015, 1990.

[105]   A. Krell, A. Teresiak, and D. Schläfer, "Grain size dependent residual microstresses in submicron Al2O3 and ZrO2," *Journal of the European Ceramic Society,* vol. 16, pp. 803-811, // 1996.

[106]   B. Clausen, T. Lorentzen, and T. Leffers, "Self-consistent modelling of the plastic deformation of f.c.c. polycrystals and its implications for diffraction measurements of internal stresses," *Acta Materialia,* vol. 46, pp. 3087-3098, 5/22/ 1998.

[107]   C. C. Wu, S. W. Freiman, R. W. Rice, and J. J. Mecholsky, "Microstructural aspects of crack propagation in ceramics," *Journal of Materials Science,* vol. 13, pp. 2659-2670, 1978/12/01 1978.

[108]   D. J. Green, *Microcraking mechanisms in ceramics, In Fracture Mechanics of Ceramics* vol. 5. New York: Plenum Press, 1983.

[109]   A. G. Evans, "Microfracture from thermal expansion anisotropy—I. Single phase systems," *Acta Metallurgica,* vol. 26, pp. 1845-1853, 12// 1978.

[110]   A. H. Heuer and M. Rühle, "Overview no. 45: On the nucleation of the martensitic transformation in zirconia (ZrO2)," *Acta Metallurgica,* vol. 33, pp. 2101-2112, 12// 1985.

[111]   S. Schmauder and H. Schubert, "Significance of Internal Stresses for the Martensitic Transformation in Yttria-Stabilized Tetragonal Zirconia Polycrystals During Degradation," *Journal of the American Ceramic Society,* vol. 69, pp. 534-540, 1986.

[112]   P. F. Becher and M. K. Ferber, "Grain-size dependence of the slow-crack growth behavior in noncubic ceramics," *Acta Metallurgica,* vol. 33, pp. 1217-1221, 7// 1985.

[113]   J. D. Almer, J. B. Cohen, and B. Moran, "The effects of residual macrostresses and microstresses on fatigue crack initiation," *Materials Science and Engineering: A,* vol. 284, pp. 268-279, // 2000.

[114] W. Pompe, Kreher, W., , *Theoretical approach to energy-dissipative mechanisms in zirconia and other ceramics* vol. 12. Columbus, Ohio: The American Ceramic Society, 1983.

[115] Y. Fu and A. G. Evans, "Microcrack zone formation in single phase polycrystals," *Acta Metallurgica,* vol. 30, pp. 1619-1625, 8// 1982.

[116] W. G. Fahrenholtz, "The ZrB2 Volatility Diagram," *Journal of the American Ceramic Society,* vol. 88, pp. 3509-3512, 2005.

[117] D. N. Talwar and J. C. Sherbondy, "Thermal expansion coefficient of 3C--SiC," *Applied Physics Letters,* vol. 67, pp. 3301-3303, 1995.

[118] C. M. Su, M. Wuttig, A. Fekade, and M. Spencer, "Elastic and anelastic properties of chemical vapor deposited epitaxial 3C-SiC," *Journal of Applied Physics,* vol. 77, pp. 5611-5615, 1995.

[119] K. Chawla, *Ceramic Matrix Composites*. Massachusetts: Kluwer Academic Publishers, 2003.

[120] M. Taya, S. Hayashi, A. S. Kobayashi, and H. S. Yoon, "Toughening of a Particulate-Reinforced Ceramic-Matrix Composite by Thermal Residual Stress," *Journal of the American Ceramic Society,* vol. 73, pp. 1382-1391, 1990.

[121] W. Kreher and R. Janssen, "On microstructural residual stresses in particle reinforced ceramics," *Journal of the European Ceramic Society,* vol. 10, pp. 167-173, // 1992.

[122] C.-H. Hsueh and P. F. Becher, "Residual thermal stresses in ceramic composites. Part I: with ellipsoidal inclusions," *Materials Science and Engineering: A,* vol. 212, pp. 22-28, 7/15/ 1996.

[123] H. Awaji, S.-M. Choi, and E. Yagi, "Mechanisms of toughening and strengthening in ceramic-based nanocomposites," *Mechanics of Materials,* vol. 34, pp. 411-422, 7// 2002.

[124] J. D. Eshelby, "The Determination of the Elastic Field of an Ellipsoidal Inclusion, and Related Problems," *Proceedings of the Royal Society of London. Series A, Mathematical and Physical Sciences,* vol. 241, pp. 376-396, 1957.